

CHINESE-RUSSIAN
"NAVIGATION AND MOTION CONTROL"
YOUTH FORUM

CONFERENCE PROCEEDINGS

PAPERS OF RUSSIAN PARTICIPANTS ONLY

CHINESE SOCIETY OF INERTIAL TECHNOLOGY
ST. PETERSBURG BRANCH OF THE RUSSIAN ACADEMY OF SCIENCES (SPBB RAS)

13th-14th DECEMBER, 2024 NANJING CHINA

The conference proceedings contain the papers from Russian participants only.

Conference Information

In order to further strengthen cooperation with the International Public Association – Academy of Navigation and Motion Control, the Chinese Society of Inertial Technology and the St. Petersburg Branch of the Russian Academy of Sciences co-sponsored the Chinese-Russian "Navigation and Motion Control" Youth Forum, which promotes the cooperation of young talents in the field of inertial technology in academia and industry, and other common interests.

Conference Dates

13th-14th December, 2024

Conference Place

Jiangsu Conference Center

No. 307 Zhongshan East Road, Xuanwu District, Nanjing, Jiangsu Province, China

Sponsor

Chinese Society of Inertial Technology

St. Petersburg Branch of the Russian Academy of Sciences (SPbB RAS)

Co-sponsor

Nanjing University of Aeronautics and Astronautics

Nanjing Inertial Technology Society

Conference Session

1 Inertial sensors, navigation and positioning systems

2 Combined navigation and motion control system

3 Global Navigation Satellite System

4 Gravity aided navigation

5 Integrated themes

CONTENTS

1. O. A. Stepanov, Yu. A. Litvinenko, A.V. Motorin, A. M. Isaev	
Comparison of Bayesian estimation and factor-graph optimization methods	6
2. A.S. Espinoza Valles, I.V. Belokonov, I.A. Lomaka, P.N. Nikolaev	
Method for the reconstruction of nanosatellite angular motion based on magnetometer measurements: a case study of SAMSAT-ION.....	9
3. A.V. Kozlov, F.S. Kapralov, G.O. Barantsev, S.A. Fedorov	
Complete calibration cycle for assembled strapdown inertial navigation systems.....	11
4. E.V. Shestakova	
Failure detection for a redundant sensor unit	14
5. Zlygosteva M.P., Kolevatov A.P., Ulianovskaia T.A., Ivshina I.V., Sergeev A.M.	
Identification of fiber optic gyroscope temperature drift models	16
6. E.V. Lukoyanov, E.V. Dranitsyna	
Comparative analysis of algorithms for increasing fault tolerance of complexes with redundant strapdown inertial navigation systems	19
7. M.A. Vlasova, A.N. Shevchenko, S.V. Ermak	
Optimizing the radio-frequency field amplitude when monitoring the vapor cell parameters in different quantum sensors.....	22
8. M. A. Sorvina	
Wireless implementation of surface acoustic wave accelerometers	25
9. Yu. A. Litvinenko, O. A. Stepanov	
The features of federated filtering methods in nonrecursive measurement processing	28
10. V. Bondarenko	
Development of a 6-axis robotic manipulator for stereotactic surgery.....	30
11. E.V. Barinova, I. V. Belokonov, I. A. Timbai	
Problems of angular motion of CUBESAT 6U nanosatellites in low earth orbits	35
12. I.S. Arkhipov	
Multi-agent real-time operating system for collaborative robot control.....	37
13. A. V. Bragin	
Gyroscope biases estimation using zero-velocity updates in pedestrian navigation	39
14. T.O. Berger, I. A. Lomaka	
Parameter selection for magnetic attitude control of small satellites in sun-synchronous orbit.....	42

15. D.G. Arseniev, A.E.Misnik, M.A.Shalukhova	
Management of patient rehabilitation in medical cyberphysical systems	44
16. A.A. Golovan, V.S. Vyazmin	
The current state of strapdown airborne gravimetry. Methodology of gravimeter data postprocessing	47
17. F.S. Kapralov	
Modern precision of attitude determination using multi-antenna satellite navigation system	50
18. I. A. Akimov	
An approach to estimating the gravity vector disturbance based on repeated airborne observations	52
19. P. S. Mikhailov, V. N. Koneshov, V. N. Solovyev	
Assessments of the accuracy of modern global models of the Earth's gravity field and experience of their use in performing marine gravimetric surveys.....	55
20. M.M. Murzabekov, D.S. Bobrov, V.P. Lopatin, E.S. Skvortsov	
Field geophysical complex for creating navigation gravity magnetic maps for autonomous navigation systems.....	57
21. D. O. Gavrilov, A. V. Ivliev	
Development of an actuator for a magnetic orientation system for a nanosatellite	60
22. V. V. Potekhin, E. V. Kuklin, P. K. Smirnov	
Control of industrial distributed systems based on open information technology.....	62
23. A. K. Golubev, A. A. Pyrkin, V. M. Fomin	
Sensorless control of induction motor	64
24. M.A. Tit, A.G. Scherbak, O.S. Yulmetova	
Experience in developing a technology of precision spherical units manufacture	66
25. M.A. Vlasova, V.V. Chalkov	
Development of a modular stand for testing quantum sensor optical cells based on a reference standard.....	69
26. S.A. Fedorov, F.S. Kapralov	
Smoothing filter for micromechanical gyroscope unstable bias estimation in dynamic calibration experiment	73
27. M. A. Ponomareva, A. V. Kramlikh	
Determination of the spacecraft orientation using instantaneous measurements	75
28. V.G. Karaulov, A.M. Gruzlikov, M. D. Korableva	
Solving the problem of relative navigation using deep neural networks	77

29. O. A. Stepanov, Yu. A. Litvinenko, A. M. Isaev	
Recursive iterative batch linearized smoother for navigation estimation problems	81
30. V.A. Bolotina, D.P Avariaskin	
Study of the influence of the Moon on the inspection motion of spacecrafts in high orbits	84
31. A. R. Brazhenko, A. O. Komarov	
Algorithm for localization and direction determination of threat impact using vision language models in autonomous transport systems	87
32. S.P. Ablyasova	
Simulation of trajectory parameters of object motion in pole areas using quasi-geodetic coordinates	91
33. D.A. Safin	
An algorithm for raw data fusion of a strapdown inertial navigation system and odometer	94
34. V. Smetanina	
Identification of spatiotemporal clusters in multi-agent systems using an endemic model.....	97
35. D. Mingazov, M. Kozin	
Research on consensus and fixed-time control methods for multi-agent systems.....	100
36. A.O. Komarov, A. R. Brazhenko	
A scene building algorithm for visualizing obstacles using two cameras	103
37. D. I. Smolianov	
On the navigation problem of unmanned wheeled agricultural machinery using inertial, satellites information and odometry	106

O. A. STEPANOV, Yu. A. LITVINENKO, A.V. MOTORIN, A. M. ISAEV
(Concern CSRI Elektropribor, ITMO University, St. Petersburg, Russia)

Comparison of Bayesian estimation and factor-graph optimization methods

Possibilities and features of designing estimation algorithms based on factor-graph optimization in problems of navigation information processing/navigation processing problems are discussed. The relationship and differences between the Bayesian approach and factor-graph optimization algorithms are considered. It is shown that the main feature of factor-graph optimization algorithms is their nonrecursive nature due to batch measurement processing, which is also practiced in the design of algorithms within the Bayesian approach. The differences between the algorithms designed with the use of these two approaches may lie in different ways of factorization of the posterior probability density function (PDF).

Examples of recursive and nonrecursive estimation algorithms designed with the use of factor-graph optimization and the Bayesian approach are given, including those for the problem of simultaneous localization and mapping.

Introduction. Algorithms based on the Bayesian estimation theory are widely used to solve problems of navigation information processing. Significant progress has been made in the field of designing such algorithms, especially with respect to linear estimation problems that are solved by means of recursive Kalman-type algorithms, which are essentially universal in nature. As for nonlinear estimation problems, there is no such a universal algorithm, which is why designing effective estimation algorithms, including those applicable to navigation applications, is still relevant. In this regard, algorithms based factor-graph optimization (FGO) have recently received considerable attention [1–15]. Currently, FGO algorithms are actively implemented in the field of navigation information processing, especially in robotic systems [1,3,5,7–15], in particular to solve problems of simultaneous localization and mapping (SLAM) [2,4,5,10–12], including the cases involving information on geophysical fields. Among the merits of FGO algorithms are their higher accuracy [1,3,7,9] compared to the extended Kalman filter (EKF) and low computational complexity compared to traditional extremum search methods [2,7]. However, the reasons behind the mentioned merits have not been given proper consideration. At the same time, it is desirable to identify these reasons and compare FGO algorithms not only with EKF, but also with other Bayesian algorithms. Such an analysis is possible due to the fact that FGO algorithms rely on factorization of the conditional (posterior) PDF of the estimated parameters, which is the basis for designing optimal Bayesian estimation algorithms. This analysis will make it possible to identify the range of navigation information processing problems for which the use of FGO algorithms is most effective, as well as problems where no significant gains can be expected as compared to Bayesian algorithms.

Thus, this work is devoted to the comparison of algorithms designed on the basis of FGO and Bayesian methods in problems of navigation information processing problems. The first part of this study deals with linear and nonlinear problems in a general formulation, while the second part considers a SLAM problem.

Comparison of methods. Many navigation estimation problems are reduced to a linear Gaussian formulation, that is, estimation of the Gaussian state vector given by a linear shaping filter based on its linear measurements with white-noise Gaussian error. In this case, from the standpoint of the Bayesian approach, the Kalman filter is an optimal solution to the filtering problem. It is also possible to design various smoothing algorithms in the Bayesian approach, in particular the Rauch-Tung-Stribel (RTS) smoothing algorithm. It can be shown that solution of the same problem in terms of FGO methods leads to the algorithms that replicate RTS smoothing [16]. This is a consequence of the factor graph triviality in such a problem, as well as the fact that in this case, the maximum of posterior density coincides with its mathematical expectation. Note that FGO-based algorithms are precisely smoothing algorithms, and it is inappropriate to compare them with filtering algorithms such as the Kalman filter.

Another broad class of problems is represented by nonlinear estimation problems. From the Bayesian approach standpoint, these problems can be solved with the use of linearization, for example, by expanding nonlinear functions in a Taylor series. This leads to suboptimal algorithms, such as EKF and smoothing EKF. When algorithms are designed on the basis of FGO, the same linearization methods as in EKF may be often used, while the factor graph of such a problem remains trivial. However, the EKF implements a recursive processing scheme with linearization for each measurement, while in FGO algorithms, linearization is carried out based on the processing results of the whole accumulated batch of measurements. The latter case is preferential, since it reduces linearization errors due to the fact that the posterior PDF is normalized with the accumulation of measurements, thus ensuring its better approximation. However, the Bayesian approach also allows for nonrecursive algorithms to process a batch of measurements in which the linearization point is adjusted similarly to the FGO based on the results of batch measurement processing, and, moreover, the algorithms can also be designed using other, more accurate, methods for representing the posterior density [15, 17, 18].

The SLAM problem stands apart among nonlinear navigation processing problems. Direct application of standard Bayesian algorithms to solve such a problem leads to an EKF with a state vector of rather high dimension, since the state vector must include all constants describing the map. The covariance matrix of such a vector is filled, which makes the EKF in the SLAM problem computationally complicated. When approaching SLAM from the FGO standpoint, it turns out that it is possible to design a nontrivial factor graph for each of these problems, which corresponds to a special factorization of the posterior density which is different from the traditional one. As a result, this makes it possible to design an algorithm that solves the problem in stages, first, the localization problem, and then, the mapping problem. In this case, there is no need to calculate the full/whole??? covariance matrix for the entire state vector, which significantly reduces the computational complexity of the algorithm [19].

Conclusion. It is shown that FGO-based algorithms are smoothing algorithms that maximize the posterior PDF, which in a linear problem is generally equivalent to Bayesian estimation algorithms. Thus, it is impossible to conclude that the accuracy of FGO algorithms in such problems can be improved and computational complexity reduced relative to Bayesian algorithms.

In nonlinear problems, the gain in accuracy of FGO algorithms as compared to recursive Bayesian algorithms is due to the use of a batch of measurements. This, in turn, with the accumulation of measurements, leads to normalization of the posterior distribution density function and, as a consequence, to its better approximation. It is noted that within the framework of the Bayesian approach, it is easy to obtain algorithms similar to the FGO algorithms. Moreover, based on the Bayesian approach, it is possible to design algorithms using other, more accurate, methods for representing the posterior density.

It is shown that in a number of problems containing many constant parameters, such as the SLAM problem, FGO methods allow designing estimation algorithms that are computationally significantly simpler than the algorithms designed by traditional methods from the standpoint of the Bayesian approach without taking into account the features of these problems.

This work was supported by the grant from the Russian Science Foundation, project no.

23-19-00626, <https://rscf.ru/project/23-19-00626/>

REFERENCES

1. Q. Zeng, W. Chen, J. Liu, and H. Wang, "An Improved Multi-Sensor Fusion Navigation Algorithm Based on the Factor Graph," *Sensors*, vol. 17, p. 641, Mar. 2017.
2. E. Olson, AXLE: Computationally-efficient trajectory smoothing using factor graph chains, 2021. *IEEE International Conference on Robotics and Automation (ICRA)*, Xi'an, China, 2021, pp. 7443-7448, doi: 10.1109/ICRA48506.2021.9561823.
3. Weisong Wen, Tim Pfeifer, Xiwei Bai Li-Ta Hsu. Factor graph optimization for GNSS/INS integration: A comparison with the extended Kalman filter. *NAVIGATION* 2021; 68:315–331.

4. A.Yu., Scalable algorithms for simultaneous mapping and localization of a swarm of mobile robots, Cand. Sci. (Tech.), St Petersburg, 2021
5. Xiwei WU, Bing XIAO, Cihang WU, Yiming GUO, Lingwei LI., Factor graph-based navigation and positioning for control system design: A review. *Chinese Journal of Aeronautics*. Volume 35, Issue 5, May 2022, pp. 25-39
6. Yanwu Zhai and Songyuan Zhang. A novel LiDAR-IMU-Odometer coupling framework for two-wheeled inverted pendulum (TWIP) robot localization and mapping with nonholonomic constraint factors. *Sensors*, 2022, 22, 4778. <https://doi.org/10.3390/s22134778>.
7. Jun Dai, Songlin Liu, Xiangyang Hao, Zongbin Ren and Xiao Yang. UAV Localization Algorithm Based on Factor Graph Optimization in Complex Scenes. *Sensors*, 2022, 22, 5862.
8. Mingxing Chen , Zhi Xiong , Jun Xiong,d Rong Wang. A hybrid cooperative navigation method for UAV swarm based on factor graph and Kalman filter, *International Journal of Distributed Sensor Networks*, 2022, Vol. 18(1).
9. Shiji Xin, Xiaoming Wang, Jinglei Zhang, Kai Zhou, and Yufei Chen, A Comparative Study of Factor Graph Optimization-Based and Extended Kalman Filter-Based PPP-B2b/INS Integrated Navigation. *Remote Sens.* 2023, 15, 5144. <https://doi.org/10.3390/rs15215144>.
10. A.A. Penkovsky, J. Mahmoud, M. Mohrat, and S.A. Kolyubin, Robust visual-inertial odometry for ground robots in dynamic environments, *30th St. Petersburg International Conference on Integrated Navigation Systems*, 2023, pp. 49–54.
11. D.A. Cherginets and A.A. Vedyakov, Design of visual-inertial odometry algorithm for a four-legged walking robot with a stereo camera, *31st Saint Petersburg International conference on Integrated Navigation Systems*, 2024, pp. 453–457.
12. A.R. Abdrashitov, Relative navigation of a group of unmanned aerial vehicles using Bayesian estimates, *Trudy XIX Vserossiiskoi nauchno-prakticheskoi konferentsii "Perspektivnye sistemy i problemy upravleniya"* (Proc. of the XIX All-Russian scientific and practical conference "Advanced systems and control problems"), 2024.
13. S.H. Quan, S.H. Chen, Y.L. Zhou S. Zhao, H.Z. Hu, Q. Zhu, A Robust IMU/GNSS/ODO integrated navigation system based on factor graph, *31th Saint Petersburg International Conference on Integrated Navigation Systems, ICINS 2024*, Proceedings. 27. 2024
14. V.G. Karaulov, A.M. Gruzlikov, O.A. Stepanov, and Yu.A. Litvinenko, Solution of the problem of AUV Positioning Relative to a Stationary Docking Station Using a Factor Graph Optimization Algorithm, *31th St. Petersburg International Conference on Integrated Navigation Systems, Conference Proceedings*. St. Petersburg, 2024.
15. O.A. Stepanov, A.M. Isaev, A.V. Motorin, Yu.A. Litvinenko, and V.P. Zolotarevich, Recursive and nonrecursive algorithms applied to navigation data processing: Differences and interrelation with factor graph optimization algorithms, *Proc. 31st St. Petersburg International Conference on Integrated Navigation Systems*, 2024, pp. 424–432.
16. A. Aravkin, B. Bell, J. Burke, and G. Pillonetto, Kalman smoothing and block tridiagonal systems: new connections and numerical stability results, arXiv, 2013, <https://doi.org/10.48550/arXiv.1303.5237>.
17. Stepanov, O.A., *Primenenie teorii nelineinoy fil'tratsii v zadachakh obrabotki navigatsionnoi informatsii* (Application of Nonlinear Filtering Theory for Navigation Data Processing), 3rd edn., St. Petersburg: Elektropribor, 2003.
18. V.A. Vasiliev, Yu.A. Litvinenko, O.A. Stepanov, and A.B. Toropov, Comparison of recursive and nonrecursive filtering algorithms for map-aided navigation problems, *XIV Vserossiiskaya mnogoprofil'naya konferentsiya po problemam upravleniya, MKPU-2021* (XIV All-Russian multi-conference on control problems), Proceedings: in 4 volumes. Rostov-on-Don, 2021, pp. 125-127.
19. F. Dellaert and GTSAM Contributors, "Georgia Tech Smoothing and Mapping Library", <https://github.com/borglab/gtsam>, 2022.

A. S. ESPINOZA VALLES, I. V. BELOKONOV, I. A. LOMAKA, P. N. NIKOLAEV
(Samara National Research University, Samara)

METHOD FOR THE RECONSTRUCTION OF NANOSATELLITE ANGULAR MOTION BASED ON MAGNETOMETER MEASUREMENTS: A CASE STUDY OF SAMSAT-ION

This study presents a method for reconstructing the angular motion of a nanosatellite using magnetometry measurements. The core concept of the method is based on using Earth's magnetic field measurements for approximate estimation of orientation quaternions and angular velocities of the nanosatellite. The application of the proposed method made it possible to reconstruct the angular motion of the SamSat-ION nanosatellite during flight tests.

Introduction. The reconstruction of spacecraft attitude motion is essential for ensuring operational functionality, particularly for missions involving scientific observations and communication. Numerous approaches have been proposed for attitude determination, utilizing data from solar panel current and sun sensors [1, 2]. Using magnetometer data for in-flight attitude estimation is especially relevant for small spacecraft with limited power and computational resources, as confirmed by multiple studies [3, 4]. This paper is devoted to a technique for nanosatellite angular motion reconstruction based on magnetometer measurements. As a result, the angular motion of SamSat-ION was successfully reconstructed during all communication sessions with the nanosatellite.

Methodology for the Reconstruction of Nanosatellite Angular Motion. The behavior of nanosatellite angular motion can be approximately reconstructed by using the direction of the local magnetic field vector measured by the onboard magnetometer. The process of reconstructing the angular motion can be divided into two stages. The first stage involves preliminary correction of magnetometry measurements, while the second stage includes the estimation of orientation parameters: initial quaternion conditions and angular velocity.

Correction of Magnetometer Measurement Errors. Before using magnetometer measurements for angular motion estimation, it is necessary to eliminate caused by the magnetometer bias vector \mathbf{b}_{mag} . To estimate the bias, the difference between the magnitude of the magnetometer measurement vector, after subtracting the bias, and the magnitude of the corresponding reference measurement vector is minimized. The calculated magnetic field measurements are derived from the IGRF-13 model, corresponding to the orbital trajectory. The orbital motion is estimated using the SGP4 model with TLE data available for the nanosatellite under consideration.

Estimation of the Initial Conditions for Angular Motion. It is necessary to align the reference magnetic field measurements with the nanosatellite's orientation. Based on the initial conditions being determined, the angular motion is predicted according to the dynamic Euler equations and kinematic equations. The calculated reference measurements are then transformed into the nanosatellite's body-fixed coordinate system (BFCS) using a rotation matrix composed of the predicted quaternions. Taking into account the estimated magnetometer bias vector, the initial conditions of the satellite's attitude motion are determined by minimizing the following objective function:

$$\Phi(\mathbf{q}_0, \boldsymbol{\omega}_0) = \sum_{i=1}^N \left(1 - \frac{(\mathbf{B}_{meas_i} - \hat{\mathbf{b}}_{mag}) \cdot \mathbf{B}_{ref_i}(\mathbf{q}_0, \boldsymbol{\omega}_0)}{\|\mathbf{B}_{meas_i} - \hat{\mathbf{b}}_{mag}\| \|\mathbf{B}_{ref_i}(\mathbf{q}_0, \boldsymbol{\omega}_0)\|} \right) \rightarrow \min_{\mathbf{q}_0, \boldsymbol{\omega}_0} \quad (1)$$

where \mathbf{q}_0 and $\boldsymbol{\omega}_0$ are the initial conditions for the orientation quaternion vector and angular velocity vector; \mathbf{B}_{meas} is the measurement vector from the onboard magnetometer; \mathbf{b}_{mag} is the bias vector of the magnetometer; \mathbf{B}_{ref} is the vector of calculated magnetometer reference measurements in the BFCS; N is the number of measurements available in a communication session.

The optimal solution to the objective function (1) can be found using methods such as the differential evolution algorithm, which offers a high degree of convergence.

Advisor: professor, head of the Inter-University Department of Space Research of Samara University, Belokonov I.V.

Application of the Methodology for the Reconstruction of Nanosatellite Angular Motion.

SamSat-ION is a CubeSat 3U developed at Samara University and launched in June 2023 to study the Earth’s magnetosphere and ionosphere. The SamSat-ION attitude determination and control system is based on active magnetic stabilization and includes several measurement instruments, such as MMC5883 magnetometers, MPU-9255 and ADXRS290 gyroscopes, and TCS3472 sun sensors. The proposed methodology was applied to reconstruct the relative motion of SamSat-ION using scientific telemetry obtained during flight testing. The initial conditions of the orientation quaternion and angular velocity were estimated for all communication sessions. Fig. 1 shows the orientation estimation results as the alignment between the magnetometer measurements and the calculated values. Fig. 2 presents the absolute angular velocity estimation results, showing the alignment between gyroscope measurements and the reconstructed angular velocity.

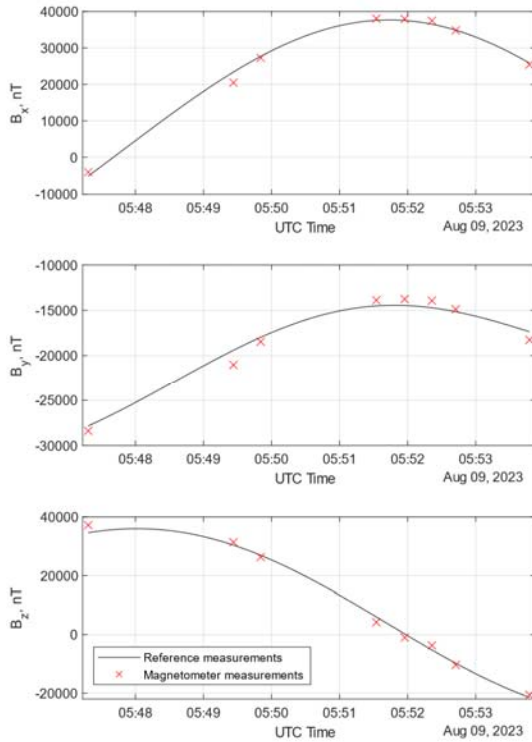


Fig. 1. Attitude estimation (correlation with magnetometer measurements)

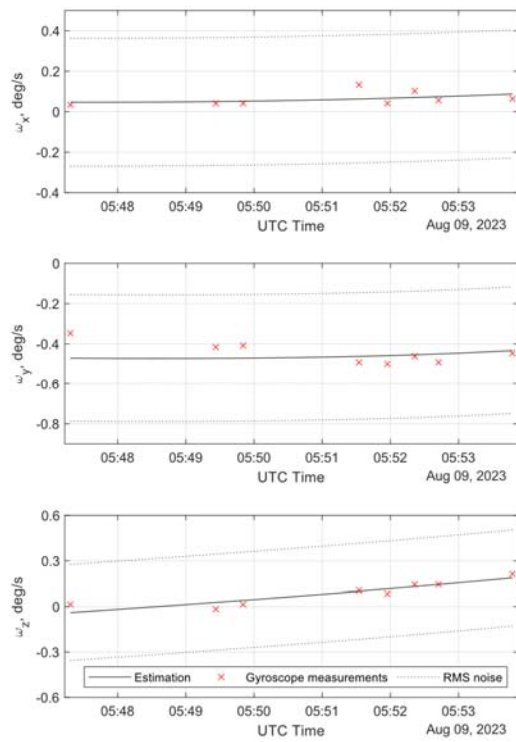


Fig. 2. Angular velocity estimation (correlation with gyroscope measurements)

As seen in the graphs, the sensor measurements align well with the calculated values. Since the calculated sensor values are directly related to the nanosatellite’s orientation, it can be concluded that the angular motion has been reconstructed with high accuracy. The angular velocity magnitude of the SamSat-ION remained within the range of 0.41–0.55 deg/s during all analyzed communication sessions.

Conclusion. This work presents an approach to reconstructing nanosatellite angular motion based on magnetometer measurements. Using the proposed approach, the angular motion of the SamSat-ION nanosatellite was successfully reconstructed during flight tests.

REFERENCES

1. **Belokonov I.V., Kramlikh A.V., Lomaka I.A., Nikolaev P.N.** Reconstruction of a Spacecraft’s Attitude Motion Using the Data on the Current Collected from Solar Panels. *Journal of Computer and Systems Sciences International*. 2019. Vol. 58. № 2. P. 286–296.
2. **Belokonov I.V., Lomaka I.A.** Postflight Recovery of the Rotational Motion of a Small Space Vehicle from Solar Sensor Information. *Journal of Computer and Systems Sciences International*. 2023. Vol. 62. № 2. P. 214–224.
3. **Ivanov D.S. et al.** The results of flight tests of an attitude control system for the Chibis-M microsatellite. *Cosmic Research*. 2014. Vol. 52. № 3. P. 205–215.
4. **Ivanov D.S. et al.** Angular Motion of the TNS-0 # 2 Nanosatellite after Launch from the International Space Station. *Cosmic Research*. 2019. Vol. 57. № 4. P. 272–288.

A.V. KOZLOV, F.S. KAPRALOV, G.O. BARANTSEV, S.A. FEDOROV
(Lomonosov Moscow State University, Moscow)

COMPLETE CALIBRATION CYCLE FOR ASSEMBLED STRAPDOWN INERTIAL NAVIGATION SYSTEMS

The report provides an extended list of error sources of inertial sensors and their corresponding calibration procedures. Altogether, they constitute a complete calibration cycle, which every navigation system should undergo through its development and production. We discuss standard sensor error model, as well as measurement timing skew, size effect, angular misalignment, elastic deformations, and other parameters. Quantitative assessment of the produced navigation errors allows one to evaluate whether particular effects should be addressed when developing a new system and its calibration methods.

Introduction. Most publications and reports about calibration of strapdown inertial navigation systems (INS) focus on specific methods for estimating null biases, scaling errors and axial misalignments of inertial sensors which measure angular rate (gyroscopes) and specific force (accelerometers). All other systematic error sources are considered already eliminated at that point. Indeed, one have to estimate these listed above parameters for each individual instrument, and their accuracy strongly affects navigation solution [1]. However, complete set of calibration and test experiments intended to assess whether the actual sensor errors conform to the models accepted for them, appears to be substantially wider, and especially so for systems under development. The report provides a more complete list of inertial sensor error sources, based on the expertise of our laboratory in developing and calibrating a wide variety of navigation instruments — from micromechanical low-grade gyrocompasses to strapdown airborne gravimeters. Authors have developed some of reported calibration techniques and their combinations, which allow reducing the time taken by calibration experiments, while some methods are listed for completeness. We also study mutual influence of error sources onto the estimation of one another, which naturally occurs in practice while working with systems not yet fully calibrated in production and/or development. We also provide quantitative relations and examples.

Error classes. For the sake of this report, we will further consider the following classes of sensor errors based on the amount and types of calibration procedures needed to produce necessary compensation models:

- parameters identical for all systems of the same type;
- parameters different for each individual instrument;
- temperature variations;
- calibration experiment parameters affecting the calibration of INS.

Let us further discuss these classes one after another.

Parameters identical for all systems of the same type. The below list of error sources are usually calibrated (or tested for) once for all INS of the same model while in development:

- synchronization of gyroscope measurements;
- timing skew between accelerometer and gyroscope measurements;
- spatial separation of accelerometer proof masses (size effect).

The significance of precise synchronization of gyroscope measurements is often not recognized at development stage, mainly due to most tests involving rotations only around single instrumental axis. However, when INS undergoes harmonic oscillations around an angle bisector between two instrumental axes, the timing skew between corresponding gyroscope measurements results in average attitude drift around orthogonal axis roughly proportional to the square of amplitude times frequency squared. For example, when amplitude is 90° and period is 5 seconds (active maneuvering), or when amplitude is $3'$ and frequency is 320 Hz (vibrations) each microsecond of the timing skew produces average attitude drift of approximately $0.15^\circ/\text{hr}$, which is unacceptable for navigation grade systems. To estimate the magnitude of this effect in a particular INS the authors have developed a dedicated experiment [2]. We designed the method to be resilient to other residual INS calibration errors.

The timing skew between accelerometer and gyroscope measurements appears to be of lower importance for navigation solution; however, as airborne gravimeter flight tests have shown, it produces considerable variations in gravity anomaly estimates. The dynamic calibration referenced below allows the estimation of the magnitude of the effect.

Spatial separation of accelerometer proof masses, better known as size effect, had been studied well in literature. Nevertheless, since gravimetry requires extreme precision in measuring acceleration while on a plane flying airborne, it implies sub-millimeter accuracy in estimating the separation parameters (see [3] for reference). This, in turn requires special methods of calibration which also should tolerate residual calibration errors for other parameters.

Parameters different for each individual instrument. We divide here error sources that require estimation of their model parameters individually for each INS instrument (excluding for now their temperature variations) into the following groups:

- errors produced by electronic circuits;
- angular alignment parameters;
- standard model of inertial sensor errors;
- extended inertial sensor error models: elastic deformations of axes of sensitivity, etc.

Errors produced by electronic circuits sometimes require separated calibration procedures, and sometimes they are mitigated using an "auto-calibration" in real time.

Angular alignment parameters allow one to align instrumental axes of the INS or inertial measurement unit (IMU) with those of the carrier object [4]. Three components of Euler rotation vector (often being small) may serve this purpose. The rotation itself may be either constant (preferably), or variable. For example, if the elastic torsion coefficients of the IMU damping system are larger than $0.5/g$ in magnitude, then under 6-g loads alignment errors will exceed threshold of $3'$, which may be undesirable.

Sensor bias, scaling and misalignment (referred here to as standard errors) calibration is widely covered in literature, though often separated from other error sources. The presence of these errors should be taken into account in every other calibration procedure. We consider two methods of calibration for the standard errors, as well as for other INS error parameters: static and dynamic calibration [5].

Extended inertial sensor error models include non-linear terms. They must be small enough to neglect multiplicative noises appearing in their compensation. Their parameter estimability in different calibration procedures, and especially how these parameters are separated from other error sources and how they are conditioned in estimation, is poorly studied. Known error sources of this type are: g-sensitivity of mechanical gyroscopes, non-linear characteristics of inertial sensors (e.g., their scaling asymmetry) and elastic deformations of their axes of sensitivity. Their calibration may be included in the procedures for standard sensor error model [6]. While developing a new INS, one should test it for the above effects, and then decide whether to neglect or compensate them in calibration.

Temperature variations. Traditionally, the approach to calibrating temperature variations is to perform calibration experiments in several temperature points. As research [7] indicates, linear temperature variations coefficients may be estimated along with other parameters under changing temperature considerably reducing the time required for calibration. For micromechanical sensors, there exist cases of signal dependency on not only on temperature itself, but also on its time profile.

Parameters inherent to calibration experiment. There exist quantities that do not affect sensor errors themselves, but still may affect calibration or skew the desired estimates if not accounted for. They include:

- turntable inclination from the plumb line and declination from reference azimuth;
- INS spatial separation from the center of rotation on a turntable [8];
- IMU damping system parameters mentioned above in regards to its axial misalignment.

For these parameters, full observability is not required, however taking them into account and their separation from estimated sensor error parameters are necessary.

Conclusion. We have presented an extended list of INS error sources, which may guide one through development and testing of newly developed inertial navigation systems. An overview of typical error manifestation cases and methods for their calibration and mitigation has been given.

ЛИТЕРАТУРА

1. **Kuznetsov A., Molchanov A., Fomichev A., Zheleznov V., Kozlov A.** On Guaranteeing Tolerances for Strapdown INS Instrumental Errors. *30th Saint Petersburg International Conference on Integrated Navigation Systems (ICINS)*, Saint Petersburg, Russia, 2023, pp. 1-6. DOI: 10.23919/ICINS51816.2023.10168385.
2. **Kozlov A., Kapralov F., Fomichev A.** Calibration of a Timing Skew between Gyroscope Measurements in a Strapdown Inertial Navigation System. *26th Saint Petersburg International Conference on Integrated Navigation Systems (ICINS)*, St. Petersburg, Russia, 2019, pp. 1-5. DOI: 10.23919/ICINS.2019.8769417.
3. **Kozlov A., Kapralov F.** Millimeter-level calibration of IMU size effect and its compensation in navigation grade systems. *2019 DGON Inertial Sensors and Systems (ISS)*, Braunschweig, Germany, 2019, pp. 1-12. DOI: 10.1109/ISS46986.2019.8943630.
4. **Kozlov A.; Kapralov F.** Angular Misalignment Calibration for Dual-Antenna GNSS/IMU Navigation Sensor. *Sensors* 2023, 23, 77. DOI: 10.3390/s23010077.
5. **Vavilova N., Vasineva I., Golovan A., Kozlov A., Papusha I., Parusnikov N.** The Calibration Problem in Inertial Navigation. *Journal of Mathematical Sciences*, 253. DOI: 10.1007/s10958-021-05272-y.
6. **Barantsev G., Kozlov A., Shaimardanov I., Nekrasov A.** A Model of the Elastic Dynamic Torsion of a Ring Laser Gyroscope Mechanical Dither and a Method for its Calibration. *29th Saint Petersburg International Conference on Integrated Navigation Systems (ICINS)*, Saint Petersburg, Russian Federation, 2022, pp. 1-4. DOI: 10.23919/ICINS51784.2022.9815435.
7. **Kozlov A., Tarygin I., Golovan A., Shaymardanov I., Dzuev A.** Calibration of an inertial measurement unit at changing temperature with simultaneous estimation of temperature variation coefficients: A case study on BINS-RT. *24th Saint Petersburg International Conference on Integrated Navigation Systems (ICINS)*, St. Petersburg, Russia, 2017, pp. 1-3. DOI: 10.23919/ICINS.2017.7995635.
8. **Kozlov A., Sazonov I., Vavilova, N.** IMU calibration on a low grade turntable: Embedded estimation of the instrument displacement from the axis of rotation. *2014 International Symposium on Inertial Sensors and Systems (INERTIAL)*, Laguna Beach, CA, USA, 2014, pp. 1-4. DOI: 10.1109/ISS.2014.6782525.

E.V. SHESTAKOVA
(Lomonosov Moscow State University, Moscow)

FAILURE DETECTION FOR A REDUNDANT SENSOR UNIT

We solve the problem of failure detection in a redundant unit of angular velocity sensors. Four methods are investigated: the method of "zero" linear combinations, the least squares method, the least absolute deviations method, and the guaranteeing approach.

Introduction. To increase the reliability of the navigation system, the redundant inertial sensor units (angular velocity sensors) are used. Instead of the commonly employed three mutually orthogonal sensors, six sensors are used. The failure detection problem in a redundant angular velocity sensor unit is considered. Four methods are studied: the method of "zero" linear combinations, the least squares method, the least absolute deviations method, and the guaranteeing approach.

Problem statement. Let the measurements delivered by the angular velocity sensor unit (at a given time instant) have the form

$$z = Gq + \varrho, \quad (1)$$

where $z = (z_1, \dots, z_6)^T \in R^6$ is a vector of angular velocity sensor unit measurements, G is a given matrix, $q \in R^3$ is a vector to be estimated, it consists of angular velocity components in projections onto the instrumental frame, $\varrho = (\varrho_1, \dots, \varrho_6) \in R^6$ is a vector of the measurement error.

Assume two failures at most can occur at a certain time instant. It is required to detect possible failures in the measurements. In other words, we need to detect the presence of failures and to determine which measurement channels they occur in.

We consider several methods for detecting the failures.

«Zero» linear combinations method. When using this method, we assume that no more than one failure can occur in the measurement channels (at a chosen time instant). The essence of the method is as follows. We find vectors x such that the desired signal is excluded:

$$G^T x = 0. \quad (2)$$

This way we achieve "direct access" to the error:

$$x^T z = x^T \varrho.$$

By solving the system (2), we obtain six linear combinations $x[1], \dots, x[6]$. Each of them contains exactly one zero entry. To detect a singular failure, we need to calculate the six inner products of z and $x[i]$. The failure occurs in the i -th channel if and only if the combination number i equals zero (is close to zero) and the other combinations are non-zero. When there are no failures, all combinations are equal to zero. Thus, the presence of a single failure can be determined by one "zero" (small in magnitude) combination and the rest non-zero combinations.

Least absolute deviations and least squares. We investigate classical estimation methods: least absolute deviations and least squares [1]. First, we find the estimate \hat{q} of the parameter vector q using the least deviations method (or least squares method). Then by the obtained estimate \hat{q} we construct the estimate of the measurement error using the formulas

$$\hat{\varrho}_i = z_i - G_i \hat{q}, \quad i=1, \dots, 6.$$

Scientific supervisor Doctor of Physical and Mathematical Sciences, Lead Research Scientist, Lomonosov Moscow State University, Faculty of Mechanics and Mathematics, Laboratory of Control and Navigation
Alexander Ivanovich Matasov_.

Then the absolute values of this estimates are compared to the prescribed threshold value Δ . We assume that the failure occurs in the channel, where the absolute value of the estimate is greater than the threshold value Δ .

Numerical testing shows that the classical methods do not provide new advantages with such small amount of measurements (six measurements in our case). The least squares method does not always detect even a singular failure. The least absolute deviations method does detect one failure but requires more computational cost than the "zero" combinations method. Both methods are unable to detect two failures reliably.

Guaranteeing estimation method. Consider a new method for determining failures, which is based on the guaranteeing approach [2-4]. The algorithm is as follows. For each row of the matrix G we construct the estimate of the scalar quantity $\widehat{G}_i q$ using the guaranteeing approach. The problem is set as an optimal estimation problem, where we minimize the maximal estimation error under all uncertain factors. At the same time, we assume that the absolute values of the errors are bounded by a known constant σ :

$$|q_i| \leq \sigma, \quad i = 1, \dots, 6.$$

Then using the formulas

$$\widehat{q}_i = z_i - \widehat{G}_i q, \quad i=1, \dots, 6$$

we obtain the estimate for the estimation error, which is compared to the threshold value Δ .

In order to calculate \widehat{q} we need to solve a set of variational problems, which can be reduced to linear programs. Due to the low dimension of the variational problems, the corresponding computational load is very moderate. At the same time, the guaranteeing estimation problem can be a reference for evaluating the quality of other simpler implemented algorithms. The advantage of the guaranteeing approach is that the problem of detecting failures is formulated as an optimal estimation problem. Therefore, unlike traditional approaches, all available information is used for estimation. Moreover, it is possible to calculate the optimal guaranteed estimation errors for the parameters. Extensive numerical testing shows that the guaranteeing approach allows us to detect two failures in an angular rate sensor unit.

Conclusion. We proposed the solution to the problem for failure detection in a redundant unit of angular velocity sensors. Four methods are investigated. Numerical testing showed that the guaranteeing approach provides the most accurate results.

REFERENCES

1. **V.I. Mudrov, V.L. Kushko.** Least Absolute Deviations Method. Moscow: URSS, 2013.
2. **A.B. Kurzhanskii.** Control and Estimation under Uncertainty Conditions. Moscow: Nauka, 1977.
3. **M.L. Lidov.** Minimax Estimation Methods. Preprint No.71, Keldysh Institute of Applied Mathematics of RAS, 2010.
4. **A.I. Matasov.** Guaranteeing Estimation Method. Moscow: Moscow University Press, 2009.

ZLYGOSTEVA M.P., KOLEVATOV A.P.¹, ULIANOVSKAIA T.A., IVSHINA I.V., SERGEEV A.M.
(Perm Scientific-Industrial Instrument Making Company, Perm)

IDENTIFICATION OF FIBER OPTIC GYROSCOPE TEMPERATURE DRIFT MODELS

Models of fiber-optic gyroscope temperature drift are investigated. Test results of fiber-optic gyroscope defects arising from changes in ambient temperature are presented. It is shown that these defects deteriorate temperature compensation efficiency. Based on the study results classification of these defects of fiber-optic gyroscope is proposed, it allows to divide inertial navigation systems created on their basis by accuracy classes. Methods have been developed for identifying models of fiber-optic gyroscope temperature drift, including using fuzzy logic method.

Introduction. The paper studies behavior of fiber-optic gyroscope (FOG) included in strapdown inertial navigation systems (SINS) produced by Perm Scientific-Industrial Instrument Making Company. Based on long-term observations of the FOG-based SINS temperature calibration results classification and identification of the FOG defects is proposed, which allows to divide the manufactured navigation systems by accuracy classes.

Fiber optic gyroscope temperature drift models. It is known that the FOG principle of operation is based on Sagnac effect [1, 2]: “the phase difference of two light waves propagating along a closed contour in opposite directions when the contour rotates around an axis normal to its plane is proportional to the angular velocity of rotation”. Despite apparent relative simplicity of the sensor, it is very sensitive to various external influences that cause side drifts distorting its signal and, therefore, leading to increase of the measurement error of absolute angular velocity projection on the object sensitivity axis [4-6, 33-36]. Change in the FOG ambient temperature has a significant influence on the FOG characteristics. Therefore, one of the main issues arising in the FOG-based SINS development is the FOG drift compensation caused by temperature changes inside a strapdown measurement module (SMM).

Direct measurement of temperature gradients and finding correlation dependences of the FOG zero offset is difficult, since multiple temperature sensors placement inside a multilayer fiber coil is a difficult task. It is difficult to develop a numerical model of this effect, because it is necessary to take into account many parameters, both design and technological: frame material and geometry, properties of a particular type of optical fiber, protective and hardening coating material, impregnation compound, coil filling factor, fiber tension force, etc. Therefore, the researchers propose simplified models of the FOG temperature drift, assuming that by the efforts of designers and process specialists the FOG temperature error gradient component will be minimized, ensuring the proposed models relevancy. Models of the FOG temperature drift are presented in [8-25]. All these works declare successful results of thermal compensation, so the authors of this report find it difficult to recommend any method, but suggest focusing on the FOG defects that worsen quality of thermal compensation.

FOG defects classification. To calculate the thermal compensation model coefficients, the FOG readings (as part of the SINS) obtained at thermal transitions when calibrating the system on Acutronic turn tables were used. The SINS calibration is performed at static temperatures and thermal transitions. Thermal transitions of the following types were used:

- 1) transitions with temperature change by $20 \div 25^\circ\text{C}$ between calibration temperature points, the rate of temperature change averages $2.5 \cdot 10^{-3} \div 5.0 \cdot 10^{-3} \text{ }^\circ\text{C/sec}$;
- 2) additional transitions by $40 \div 70^\circ\text{C}$, the rate of temperature change averages $7.0 \cdot 10^{-3} \div 0.01 \text{ }^\circ\text{C/sec}$;

¹ Supervisor PhD, associate professor, department head, Andrei Petrovich Kolevatov

3) self-heating - the system cold start and keeping it switched on until it reaches a stable temperature mode without external heat/cooling sources, the temperature change rate is up to $1.5 \cdot 10^{-3}$ °C/sec.

At thermal transitions the SINS is installed in the plane of horizon with a given direction relative to the meridian plane. Thermal drift is evaluated by averaging the FOG initial readings at 5 minutes using moving average method. The chosen value of the FOG readings averaging interval is determined by the results of calculation of D. Allan variations of the FOG investigated batch output readings [30]. The temperature derivative is calculated from the temperature sensor readings of the FOG. The detected defects of optical units according to the results of thermal compensation are classified as follows:

- 1) change of steady-state temperature zero offset;
- 2) increased intensity of the FOG drift noise component;
- 3) S-shape of the FOG thermal drift;
- 4) irregular shape of the FOG drift;
- 5) drift advance/delay relative to the rate of temperature change;
- 6) presence of emissions.

The concept of the FOG controlled temperature drift is introduced, for which the value of the permissible residual drift is limited to the range of $\pm 0.03^\circ/\text{hour}$.

Defect Identification. As a rule, reviewing graphs with test results of a product takes a lot of time and it is a manual and labor-intensive process. Therefore, in the present work we proposed algorithms that allow automatic identification of defects of a fiber-optic gyroscope during thermal compensation. To identify defects, methods of statistical processing of measurements [31] are used, with the help of which basic scales and membership functions are formed for application of the fuzzy set theory [32]. About 60 reports on thermal compensation of FOGs were analyzed. The results of automatic identification were compared with manual defect analysis. According to the study sample about 72% of the reports completely conforms with the visual inspection results, this demonstrates effectiveness of the proposed identification methods. Note that all the FOG described defects are not amenable or little amenable to algorithmic thermal compensation, however, they may indicate certain structural or technological defects in the FOG sensitive elements, which in the future will be able to help FOG developers to understand the defects cause and get the opportunity to eliminate them.

REFERENCES

1. Lefevre, H.C., *The Fiber Optic Gyroscope*, Boston, MA, USA, Artech House, 2014, p. 343.
2. W.K. Burns, P.F. Liao, P. Kelley. *Optical fiber rotation sensing*. Academic press, 1994, p. 390
3. Shupe D.M. Thermally induced non-reciprocity in the fiber-optic interferometer // *Applied optics* 1980, vol.19, No. 5, pp. 654-655. DOI: 10.1364/AO.19.000654
4. Mohr F., Schadt F. Bias error in fiber optic gyroscopes due to elasto-optic interactions in the sensor fiber. *Proc. SPIE*, 2004, vol. 5502, pp. 410–413. DOI: 10.1117/12.566654 Available at:
5. <http://proceedings.spiedigitallibrary.org/proceeding.aspx?articleid=848587>
6. Schadt F., Mohr F. Error signal formation in FOGs through thermal and elasto-optical environment influence on the sensing coil // *Proc. Inertial Sensors and Systems*. 2011. P. 2.1–2.13.
7. Hocker G.B. Fiber-optic sensing of pressure and temperature. *Appl. Opt.*, 1979, Vol. 18, No. 9, pp. 1445–1448. DOI: 10.1364/AO.18.001445
8. Ling W., Li X., Xu Z., Zhang Z., Wei Y. Thermal effects of fiber sensing coils in different winding pattern considering both thermal gradient and thermal stress. *Optics Communications*, 2015, vol. 356, pp. 290–295. DOI: 10.1016/j.optcom.2015.08.002.
9. IEEE Standard Specifying and Testing Single-Axis Interferometric Fiber Optic Gyros, IEEE Std 952- 2020 (Revision of IEEE Std 952-1997)
10. V. E. Dzhashitov, V. M. Pankratov. *Mathematical Models of Thermal Drift of Inertial Systems Gyroscopic Sensors*. St. Petersburg: SSC RF Central Research Institute "Electropribor", 2001. 150 pages.
11. V. E. Dzhashitov, V. M. Pankratov, A. V. Golikov, S. G. Nikolaev, A. P. Kolevatov, A. D. Plodnikov, K. V. Koffer. Hierarchical Thermal Models of FOG-based Strapdown Inertial Navigation System. *Gyroscopy and Navigation*, July 2014, Volume 5, Issue 3, pp. 162-173.
12. V. E. Dzhashitov, V. M. Pankratov, A. V. Golikov, S. G. Nikolaev, A. P. Kolevatov, A. D. Plodnikov, K. V. Koffer. Temperature Calibration of a Strapdown Navigation System Based on Signals from Distributed Thermal Sensors. *Mechatronics, Automation, Control* No 7, 2013, pp. 42-47.

13. V. E. Dzhashitov, V. M. Pankratov. Mathematical Models of Thermal Drift of Inertial Systems Gyroscopic Sensors. St. Petersburg: SSC RF Central Research Institute "Electropribor", 2001. 150 pages.
14. A. P. Kolevatov, S. G. Nikolaev, A. G. Andreev, V. S. Ermakov, O. L. Kel, D. I. Shevtsov. Fiber-Optic Gyroscope for Strapdown Navigation Systems. Development, Thermal Compensation, Testing. Gyroscopy and Navigation No 3(70) 2010, pp. 49-60.
15. Investigation of the Output Signal Dependence of a Fiber-Optic Gyroscope on Temperature as part of a Gimballess Inertial Measurement Unit // E. V. Dranitsyna, D. A. Egorov. (<https://textarchive.ru/c-1987880.html>)
16. G. I. Yemelyantsev, A. P. Stepanov. Integrated Navigation System. St. Petersburg: SSC RF Central Research Institute "Electropribor", 2016. – 394.
17. Dranitsyna, E., Gontar, D.A., Compensation for the Temperature Dependence of the Fog Output Signal, International Workshop Navigation and Motion Control (NMC 2021), IOP Conference Series: Materials Science and Engineering, 2022, vol. 1215 (2022), no. 012003, pp. 1–5.
18. Esipenko I. A., Lykov D. A., Mathematical Model of Fiber-Optic Gyroscope Thermal Drift and its Experimental Verification // Bulletin of the Bauman Moscow State Technical University. Ser. Instrumentation. 2017. No 5, pp. 31–46. DOI: 10.18698/0236-3933-2017-5-31-46.
19. Vakhrameev E. I., Galyagin K. S., Ivonin A. S., Oshivalov M. A., Ulrich T. A. Fiber-Optic Gyroscope Thermal Drift // News of Higher Educational Institutions. Instrumentation. 2011. Volume 54, No 1. pp. 32–37.
20. Vakhrameev E. I., Galyagin K. S., Ivonin A. S., Oshivalov M. A. Forecast and Correction of Fiber-Optic Gyroscope Thermal Drift // News of Higher Educational Institutions. Instrumentation. 2013. Volume 56, No 5, pp. 79–84
21. Vakhrameev E. I., Galyagin K. S., Oshivalov M. A., Savin M. A. Methods of Numerical Forecasting and Correction of Fiber-Optic Gyroscope Thermal Drift // News of Higher Educational Institutions. Instrumentation. 2017. Volume 60, No 1, pp. 32–38
22. Frolov A. V., Mikhailov Yu. V., Smirnov S. V. Development and Validation of a Methodology for Modeling Thermal and Deformed State of Strapdown Inertial Navigation System Parts. Bulletin of the Bauman Moscow State Technical University. Ser. Instrumentation, 2022, No 1 (138), pp. 32–48. DOI: <https://doi.org/10.18698/0236-3933-2022-1-32-48>
23. Research and Improvement of the Fiber-Optic Gyroscopes Accuracy Parameters. / A.S. Aleynik. Dissertation for the Degree of Candidate of Technical Sciences. St. Petersburg 2012. St. Petersburg National Research University of Information Technologies, Mechanics and Optics at the Department of Physics and Optical Communication Technology.
24. Pylaev Yu. K. Temperature Disturbances of a Strapdown Inertial Navigation System with Fiber-Optic Gyroscopes. Degree of Candidate of Technical Sciences. Institute of Problems of Precision Mechanics and Control of the Russian Academy of Sciences, NPP Antares LLC, Saratov 2004. 263 pages.
25. Tarygin E. I. Calibration Method of Thermal Model of Sensitive Elements Unit Consisting of Three Angular Velocity Sensors. Gyroscopy and Navigation. Volume 27. No 4 (107), 2019, pp. 88 – 102.
26. Kozlov A. V., Tarygin I. E., Golovan A. A., Shaimardanov I. H., Dzuev A. A. Calibration of Inertial Measurement Units with Assessment of Temperature Dependencies Based on Variable Temperature Experiment: Calibration Results of the БИНС-PT // XXIV St. Petersburg International Conference on Integrated Navigation Systems. Digest. St. Petersburg: JSC "Concern "Central Research Institute "Electropribor", 2017, pp. 225–228.
27. Nikiforovsky D. A., Deineka I. G., Sharkov I. A., Meshkovsky I. K. Method for Compensating Fiber-Optic Gyroscope Temperature Drift Using Correlations between the Gyroscope and Several Temperature Sensors Readings. Gyroscopy and Navigation. Volume 30. No 2 (117), 2022. pp. 71-80.
28. Meshkovsky I. K., Rupasov A. V., Strigalev V. E., Sharkov I. A. (ITMO Research Institute, St. Petersburg, Russia) Investigation of the Effect of Thermal Influences on Fiber-Optic Gyroscope Operation. XXI St. Petersburg International Conference on Integrated Navigation Systems. 2014.
29. Klimkovich B. V. Influence of Temperature Sensors Random Error on the Quality of Temperature Compensation of the Zero Offset by a Neural Network // Gyroscopy and Navigation. 2020. T. 28. №4 (111), pp. 53–70. DOI 10.17285/0869-7035.0049.
30. Antonova M. V., Matveev V. A. A Model of Fiber-Optic Gyroscope Error under the Influence of Thermal and Magnetic Fields // Bulletin of the Bauman Moscow State Technical University. Ser. Instrumentation. 2014. No 3, pp. 73–80.
31. On the Issue of Evaluating Noise Components of the Measuring Path using Allan Variation Method / D. A. Kutova, O. I. Maslova, S. Y. Perepelkina, A. A. Fedotov // Gyroscopy and Navigation. – 2015. – № 2 (89). – pp. 30–39.
32. Pugachev V. S. Probability Theory and Mathematical Statistics. М.: ФИЗМАТГИЗ. 2002. – 496 pages.
33. Averkin A. N., Bатыршин I. Z., Blishun A. F., Silov V. B., Tarasov V. B., Pospelova D. A. Fuzzy Sets in Control and Artificial Intelligence Models. М.: Книга по требованию, 2024. – 312 pages.
34. Rui S., Xiyuan C., Chong S., Hong Z. Modeling FOG drift using back-propagation neural network optimized by artificial fish swarm algorithm // Journal of Sensors, 2014, Volume 2014, Article ID 273043, 6 pages, DOI : <http://dx.doi.org/10.1155/2014/273043>
35. Haotian Y., Bin Z., Lixin W., Rong Z. A Novel tri-axial MEMS gyroscope calibration method over a full temperature range // Sensors, 2018, 18, 3004; DOI: 10.3390/s18093004, www.mdpi.com/journal/sensors
36. Xuyou L., Chen Z., Zhou H., Zhen Z. Temperature errors of IFOG and its compensation in engineering application // The Ninth International Conference on Electronic Measurement & Instruments, 2009, ICEMI'2009
37. Chun-Lei Z., Qi Z., Shu-Hua Y., Lei G., Guo-Chao W. Modeling and compensation for temperature errors of interferometric fiber optic gyroscope // International Conference on Information and Automation, 2009

E.V. LUKOYANOV, E.V. DRANITSYNA
(Concern CSRI Elektropribor, ITMO University, St. Petersburg)

COMPARATIVE ANALYSIS OF ALGORITHMS FOR INCREASING FAULT TOLERANCE OF COMPLEXES WITH REDUNDANT STRAPDOWN INERTIAL NAVIGATION SYSTEMS

Three algorithms for increasing fault tolerance of complexes—integrated systems with redundant strapdown inertial navigation systems (SINS)—are analyzed and compared from the standpoint of their efficiency. The proposed algorithms are based on the method of pairwise difference calculation and its various modifications. Comparison is supported by semi-natural simulation, in which the experimental data are complemented with the simulated faults.

Introduction. Like any equipment, SINS are prone to faults and can generate navigation solutions with errors that significantly higher than the stated accuracy. This can be caused by hardware or software faults, as well as by operating conditions that differ from those specified for these systems. In order to increase fault tolerance of SINS-based integrated systems (IS) [1, 2], it is necessary to implement methods for fault detection and isolation (FDI) [3-7].

FDI methods for SINS can be implemented at the levels of either inertial sensors or IS [8]. The following methods can be used for sensors: checking for exceeding the ranges of measured values, based on the expected object's motion dynamics; integrity monitoring by direct checks of the consistency between the values calculated from different combinations of measurements, or with the model of the object's motion. Different FDI methods are not mutually exclusive and are often combined.

If a fault is detected in an inertial sensor, its output data cannot be used any further. The absence of redundant inertial sensors means a failure of the SINS as a whole. For this reason, redundant SINS are often provided to increase fault tolerance at the IS level [9]. In this case, three identical systems are commonly used, wherein the faulty system is determined by comparing pairwise differences of the generated navigation parameters of the same type. As a result, the faulty SINS is excluded from generation of a general navigation solution. This approach is used not only in marine navigation, but also in aviation [10-12] and satellite navigation systems [13, 14].

The purpose of this study is to compare the efficiency of three methods for detecting faulty SINS caused by abnormal readings of inertial sensors when using a triple system. The methods we propose are based on the analysis of pairwise differences (PD) for the parameters measured by inertial sensors, namely:

- detection by the weighted sum of PD;
- detection using an adaptive threshold for PD;
- detection using an adaptive threshold for the principal components [15] of PD.

FDI problem statement. In comparison with the existing algorithms, in which the FDI problem is solved at the IS level, so that the values of the SINS output navigation and dynamic parameters are used, the authors propose to implement the isolation of faults at the sensor level, which will reduce the time from the occurrence of a fault to its detection. In addition, this approach will make it possible, due to redundancy, to replace unreliable measurements of sensors, and thereby ensure isolation of faults and the uninterrupted output of the navigation solution.

The measurements used to solve the diagnostics problems of a redundant system are a composite vector of output signals from similar sensors of different SINS, for example, accelerometers, gyroscopes or temperature sensors:

$$S_i = [X_{1,i} \ Y_{1,i} \ Z_{1,i} \ X_{2,i} \ Y_{2,i} \ Z_{2,i} \ X_{3,i} \ Y_{3,i} \ Z_{3,i}]^T, \quad (1)$$

where $X_{r,i}$, $Y_{r,i}$, $Z_{r,i}$ is a signal from the r -th SINS ($r=1$ is the main SINS, $r=2$, $r=3$ are redundant) along the corresponding measuring axis at the i -th moment in time.

It is necessary to solve the problem of detecting the fact of the fault at the i -th moment in time and to determine the number of the sensor whose data are not reliable.

Experimental data. The comparison of the algorithms was carried out by means of semi-natural simulation of the three SINS operation under conditions of a vibrating stationary base. Then, the obtained data were complemented with the simulated faults. In particular, a class of multiple (from 1 to 5 cycles) additive faults of medium and low levels was simulated, occurring at arbitrary moments in the gyroscope readings, along different axes in three identical SINS. The fault amplitude was set randomly in the range from 100 to 1000 °/h.

Brief description of the compared algorithms. The first algorithm is based on the analysis of the *weighted sum of pairwise differences* for the values measured by inertial sensors along the same axes. For each measurement S_i , we calculate the vector of pairwise differences, after which the weighted sum of its components is divided by the average variance of the vector S_i components (it is assumed that it is identical for the sensors installed on different axes and in different systems). In this case, the function of making a decision on the fault occurrence is quite simple: if the value of the sum exceeds a certain specified threshold (in accordance with the expert data on the system), then the system is faulty.

In the second algorithm, unlike the first one, the *operation threshold is calculated individually* for each pairwise difference, which allows increasing the algorithm's sensitivity to faults. In order to determine the fact of a fault, it is sufficient to determine that the individual threshold is exceeded at least for one of the pairwise differences.

The third algorithm is, to a certain extent, a variation of the second approach in terms of formation of an adaptive detection threshold. The difference is that in the calculation of the threshold value, we no longer use the values of the pairwise differences themselves as a parameter, but their *transformations to the principal components*. To determine the fact of a fault, it is sufficient to determine that the individual threshold is exceeded at least for one of the principal components of the pairwise differences.

Comparative analysis of the algorithm's performance. For each algorithm, the confusion matrix was calculated, which is classical in binary classification problems [16], a special case of which is the FDI problem.

Analysis of the simulation results has shown that the algorithms using the adaptive threshold have a higher detection recall in the case of small- and medium-level faults (~ 30-55%), while the classical pairwise difference method provides a solution to the problem at a level of (~ 2-37%). For large-level faults, all algorithms have shown approximately the same result (~ 99-100%). For the problem of finding a failed sensor, we calculated similar metrics, which showed a 100% result in all experiments. It follows that to solve diagnostics problems at a high level, it is necessary to provide, first of all, a solution to the problem of detecting small-level faults, while solution to the problem of finding faults after the detection stage does not present difficulties any longer.

Conclusion. A comparative analysis of the efficiency of three algorithms for increasing the fault tolerance of IS with redundant SINS based on the comparison of pairwise differences in the parameters measured by inertial sensors has been carried out. The comparison of the methods was performed by means of semi-natural simulation of the three SINS operation under the same conditions but with different faults in the readings of inertial sensors. Based on the simulation results, it can be concluded that the most effort-consuming faults to detect are small-amplitude faults. In this case, methods with an adaptive threshold solve this problem more effectively. One of the possible lines of research is integration of the proposed algorithms for solving FDI problems of inertial sensors to achieve the greatest efficiency.

This work was supported by the grant from the Russian Science Foundation,
project no. 23-79-10071, <https://rscf.ru/project/23-79-10071/>

REFERENCES

1. IMO Resolution MSC.252(83). Adoption of the revised performance standards for integrated navigation systems (INS).

2. Standard IEC 61924-2:2021. Maritime navigation and radiocommunication equipment and systems - Integrated navigation systems (INS) - Part 2: Modular structure for INS - Operational and performance requirements, methods of testing and required test results.
3. Chen, J. and Patton R.J., Robust model-based fault diagnosis for dynamic systems. Springer Science & Business Media, 2012. – T. 3.
4. Dmitriev, S.P., Kolesov, N.V., and Osipov, A.V., Informatsionnaya' nadezhnost' upravlenie i diagnostika navigatsionnykh system (Information reliability, monitoring and diagnosis of navigation systems), St. Petersburg: OAO Kontsern TsNII, 2003.
5. Kolesov, N.V., Tolmacheva, M.V., and Yukhta, P.V., Real-time systems. Planning, analysis, and diagnosis. St. Petersburg: OAO Kontsern TsNII, 2014.
6. Wang R., Xiong, Z., Liu, J., Xu, J., and Shi, L. Chi-square and SPRT combined fault detection for multisensor navigation, *IEEE Transactions on Aerospace and Electronic Systems*, 2016, vol. 52, no. 3, pp. 1352-1365.
7. Koshaev, D.A., Kalman filter-based multialternative method for fault detection and estimation, *Automation and Remote Control*, 2010, vol. 71, no. 5, pp. 790-802.
8. Groves, P.D., Principles of GNSS, inertial, and multisensor integrated navigation systems, [Book review], *IEEE Aerospace and Electronic Systems Magazine*, 2015, vol. 30, no. 2, pp. 26-27.
9. Dubrova E. Hardware redundancy, *Fault-Tolerant Design*, 2013, pp. 55-86.
10. Zemlyanyi, E.S. and Tektov, M.V., Quorum-element for determining the parametric fault of heading and vertical reference systems, *Vestnik Tul'skogo gosudarstvennogo universiteta. Tekhnicheskiye nauki*, 2023, no. 6, pp. 104-109.
11. Dai, Y., Lai, J., Zhang, Q., Li, Z., and Shen, Y., An Improved Fault Detection and Isolation Method for Airborne Inertial Navigation System/Attitude and Heading Reference System Redundant System, *Aerospace*, 2023, vol. 10, no. 12, p. 1024.
12. Slim, M., Saied, M., Mazeh, H., Shraim H., Francis C. Fault-Tolerant Control Design for Multirotor UAVs Formation Flight, *Gyroscopy and Navigation*, 2021, vol. 12, no. 2, pp. 166-177. DOI:10.1134/S2075108721020061
13. Humphreys, T.E., Ledvina, B.M., Psiaki, M.L., O'Hanlon, B.W., and Kintner, P.M., Assessing the spoofing threat: Development of a portable GPS civilian spoofer, *Proc. 21st International Technical Meeting of the Satellite Division of The Institute of Navigation (ION GNSS 2008)*, 2008, pp. 2314-2325.
14. Veremeyenko, K.K. and Antonov, D.A., Detection of Satellite Navigation System Faults in the Integrated Navigation System, *XXIII St. Petersburg International Conference on Integrated Navigation Systems*, 2016.
15. Abdi, H. and Williams L.J., Principal component analysis, *Wiley interdisciplinary reviews: computational statistics*. 2010, vol. 2, no. 4, pp. 433-459.
16. Li, B., Wang, H., Mu, L., Shi, Z., & Du, B. A configuration design method for a redundant inertial navigation system based on diagnosability analysis // *Measurement Science and Technology*, 2020, vol. 32, no. 2 p. 025111.

M.A. VLASOVA, A.N. SHEVCHENKO,
 (Concern CSRI Elektropribor, JSC, St. Petersburg, Russia)
 S.V. ERMAK (St. Petersburg Polytechnic University, St. Petersburg, Russia)

OPTIMIZING THE RADIO-FREQUENCY FIELD AMPLITUDE WHEN MONITORING THE VAPOR CELL PARAMETERS IN DIFFERENT QUANTUM SENSORS

The paper studies the dependence of the resonance slope of a quantum optically pumped magnetometer scheme on the radiofrequency (RF) field amplitude. Numerical modeling of the resonance slope vs. RF field amplitude has been performed for the paraffin-coated and buffer vapor cells. Modeling has been experimentally verified on a cell with high buffer gas pressure.

Introduction. A quantum sensor is a high-accuracy measurement device using the quantum effects to detect and measure different physical magnitudes: magnetic field intensity, angular velocity, time, frequency. The key component of the quantum sensors based on the effect of double radio-optical resonance is a vapor cell [1-4] containing the vapors of alkali metals used to spin polarize the atoms by optical pumping. The quality of manufacturing and filling the vapor cell mainly determines the accuracy and sensitivity of the quantum sensor [2, 3]. This quality can be estimated by analyzing the magnetic resonance line [5], the width of which can be used to determine the alkali gas relaxation rate, which directly affects the sensor sensitivity. In the cells with different mechanisms of reducing the alkali metal relaxation rate (with antirelaxation coating [6] and buffer gas [7]) the characteristic relaxation rates may differ by two to three orders of magnitudes, whereas the technological tolerance for one type cells does not exceed 10%. In practice, the width of magnetic resonance line depends not only on the parameters of the measured vapor cell but also on the measurement conditions [8-10], the most important being the amplitude of the alternating RF magnetic field, which excites the precession of magnetic moments. In experimental samples of quantum magnetometers, the RF field amplitude is optimized for the specific cell, however, in serial production it is too labor-consuming. This paper focuses on the optimization of RF field amplitude in characterization of vapor cells of different types and of one type.

Optimization of RF field. The magnetic resonance line is observed using a setup consisting of an M_x -magnetometer on the tested cell with a magnetic shield and a coil system providing the constant bias field [11]. M_x -signal determining the sensitivity of the quantum M_x -magnetometer (minimum detectable variation of the magnetic field) can be presented as [12]:

$$M_x = M_0 \frac{\Delta\omega \cdot \gamma \cdot B_1}{\Delta\omega^2 + \Gamma^2 + (\gamma \cdot B_1)^2} = M_0 \frac{\Delta\omega \cdot \gamma \cdot B_1}{\Delta\omega^2 + W^2}, \quad (1)$$

where M_0 is the longitudinal magnetization caused by the circular component of the pumping light along the magnetic field; γ is the gyromagnetic ratio of the alkali metal; B_1 is the RF field amplitude; $\Delta\omega = \omega_{rf} - \omega_0$ is the mismatch between the frequency ω_{rf} and the resonance frequency ω_0 ; $\Gamma = \frac{1}{T}$ is the alkali metal relaxation rate; $W = \sqrt{\Gamma^2 + (\gamma \cdot B_1)^2}$ is the width of magnetic resonance line.

The M_x -signal is primarily determined by the amplitude of RF field used to excite the resonance transitions between the atomic energy levels. Increasing the RF field amplitude, on the one hand, increases the signal amplitude and thus the sensor sensitivity, on the other hand, widens the resonance line so that it becomes visually unobservable. Therefore, it is needed to select the optimal RF field amplitude ensuring the maximum signal amplitude and acceptable resonance line width.

The optimal amplitude is selected using the resonance slope, which is theoretically calculated as the signal first derivative with respect to frequency mismatch at the point with zero mismatch (i.e., when the RF field frequency equals the Larmor frequency, or at the resonance center) [13]:

$$K = \left. \frac{dM_x(\omega)}{d\Delta\omega} \right|_{\Delta\omega=0} = M_0 \frac{\gamma \cdot B_1}{\Gamma^2 + \gamma \cdot B_1^2} = M_0 \frac{\gamma \cdot B_1}{W^2}. \quad (3)$$

Numerical Modeling. We provide the results from numerical modeling of the resonance slope vs. the frequency of RF field generated on the coils for two types of cells: with antirelaxation coating (characteristic relaxation rate $\Gamma_{char.} = 1$ Hz [6]) and with buffer gas ($\Gamma_{char.} = 1000$ Hz [7]). Figure 1 presents the plots of resonance slopes calculated by (3) normalized to its maximum vs. $\gamma \cdot B_1$ for two types of cells. It is seen that the acceptable values of $\gamma \cdot B_1$ (the slope is max 80% of the maximum achievable value) are within 0.5–2 Hz for the cells with antirelaxation coating and within 500–2000 Hz for buffer gas cells. For both types, the maximum slope is achieved at $\gamma \cdot B_1 = \Gamma$.

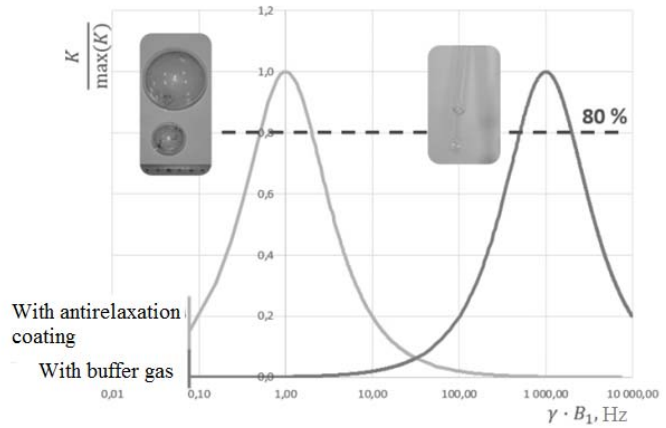


Fig. 1. Modeling the resonance slope for paraffin-coated and buffer gas cells.

Experiment. To experimentally verify the modeling results we used the buffer gas cell. Different amplitudes of the resonance RF field $\gamma \cdot B_1$ were set with the coils, and for each one the width W and amplitude S were calculated and used further to experimentally find the resonance slope [13]:

$$K = \frac{S}{W}. \quad (4)$$

The resonance slope K vs. $\gamma \cdot B_1$ is shown in Fig. 2. For the studied buffer gas cell the resonance slope is maximum at the RF field amplitude $\gamma \cdot B_1 \approx 1000$ Hz, which is close to the characteristic relaxation rate $\Gamma_{char.}$. The resonance slope decreases by no more than 20% under the amplitudes within 500–1800 Hz.

Therefore, setting the RF field amplitude B_1 so that $\gamma \cdot B_1 \approx 1000$ Hz, we can test the buffer gas cells with the characteristic relaxation rate $\Gamma_{char.}$ within 500–1800 Hz. This range is wider than the technological tolerance of characteristic relaxation rates for the cells of one type, which is max 10%. This allows measuring the cells with the same relaxation rate reduction mechanism without changing the setup parameters.

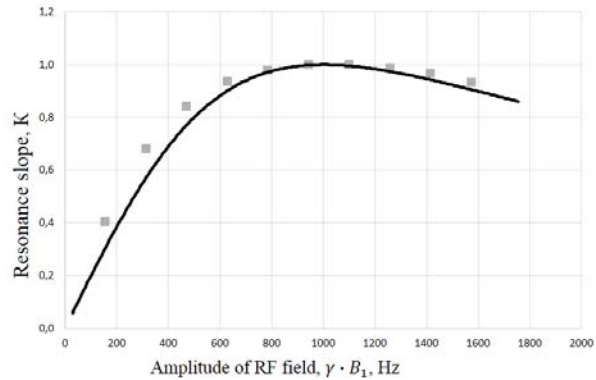


Fig. 2. Resonance slope vs. RF field amplitude.

Conclusions. The paper studies the dependence of resonance slope of a quantum optically pumped magnetometer scheme on the RF field amplitude. Numerical modeling has revealed that different optimal amplitudes provide the maximum resonance slope for different types of cells. For a buffer gas cell, the experimentally determined range of RF field amplitudes ensuring the maximum resonance slope is shown to agree with the numerically obtained range.

REFERENCES

1. Walker T. G., Larsen M. S. Spin-exchange-pumped NMR gyros. *Advances in Atomic, Molecular, and Optical physics*. 2016. Vol. 65. P. 377.
2. Vershovskii A.K., Litmanovich Yu.A., Pazgalev A.S., Peshekhonov V.G. Nuclear magnetic resonance gyroscope: The ultimate parameters. *Gyroscopy and Navigation*. 2018. Vol. 9. No. 3. P. 162.
3. Knapkiewicz P. Technological assessment of MEMS alkali vapor cells for atomic references. *Micromachines*. 2018. Vol. 10. No. 1. P. 25.
4. Vlasova M. A., Shevchenko A. N. Development of alkali vapor cell for miniature nuclear magnetic gyroscope. *IOP Conference Series: Materials Science and Engineering*. IOP Publishing. 2022. Vol. 1215. No. 1. P. 012013.

5. **Alexandrov E.B., Balabas M.V., Pazgalev A.S., Vershovskii A.K., Yakobson N.N.** Double-resonance atomic magnetometers: From gas discharge to laser pumping. *Laser Physics*. 1996. Vol. 6. No. 2. P. 244-251.
6. **Alexandrov E.B., Balabas M.V., Pasgalev A.S., Vershovskii A.K., Yakobson N.N.** Light-induced desorption of alkali-metal atoms from paraffin coating. *Physical Review A*. 2002. Vol. 66. No. 4. P. 042903.
7. **Budker D., Romalis M.** Optical magnetometry. *Nature Physics*. 2007. Vol. 3. No. 4. P. 227-234.
8. **Appelt S., Ben-Amar Baranga A., Young A. R., and Happer W.** Light narrowing of rubidium magnetic-resonance lines in high-pressure optical-pumping cells. *Physical Review A*. 1999. Vol. 59. No. 3.
9. **Bison G., Wynands R., Weis A.** Optimization and performance of an optical cardiomagnetometer. *JOSA B*. 2005. Vol. 22. No. 1. P. 77-87.
10. **Vlasova M.A., Shevchenko A.N., Dement'ev M.M.** Development of thermostabilization systems for quantum sensor vapor cell testing. *Almanakh nauchnykh rabot molodykh uchenykh Universiteta ITMO (Almanac of Papers by Young Researchers of ITMO University)*. 2022. Vol. 2. Pp. 15-18.
11. **Pomerantsev N.M., Ryzhkov V.M., Skrotskii G.V.,** *Fizicheskie osnovy kvantovoi magnitometrii (Physical Foundations of Quantum Magnetometry)*, Moscow: Nauka, 1972.
12. **Bloch F.**, Nuclear induction, *Physics Review*, 1946. Vol. 70. No. 7. Pp. 460-474.
13. **Vershovskii A.K. and Pazgalev A.S.** Optimization of the Q factor of the magnetic M_x resonance under optical pump conditions. *Technical Physics*. 2008. Vol. 53. No. 5. Pp. 646-654.

M. A. SORVINA

(Saint Petersburg Electrotechnical University "LETI", St. Petersburg)

WIRELESS IMPLEMENTATION OF SURFACE ACOUSTIC WAVE ACCELEROMETERS

The operating principle and development trends of surface acoustic wave accelerometers are described. Four methods for implementing wireless data transmission from a sensitive element are proposed. Their advantages and disadvantages are described. A simplified multiphysical model is presented, allowing the proposed methods to be simulated.

Introduction. Surface acoustic wave (SAW) accelerometers have attracted considerable attention from research groups due to their robustness, impact resistance, high sensitivity, and low power consumption [1-2]. These accelerometers use the propagation of acoustic waves along the surface of a piezoelectric material to estimate the acceleration values of the object on which they are installed. With the development of wireless technologies [3], the integration of SAW accelerometers with wireless data transmission systems is becoming increasingly feasible, making them ideal for various applications, such as industrial monitoring [4].

This paper examines ways to organize the sensitive element of a SAW accelerometer for subsequent data transmission.

Wireless Surface Acoustic Wave Accelerometer. The report includes a description of the operating principle of a SAW accelerometer, variants of passive connection schemes, and modeling in Comsol Multiphysics of a sensitive element with two-way signal transmission.

Configuration of the sensitive element of the SAW accelerometer. The sensing element of the SAW accelerometer includes a piezoelectric substrate 1 equipped with interdigital transducers (IDT) 2 and 3 on its surface (Fig. 1a). The input IDT 3 converts the electrical signal into an acoustic wave, which propagates along the substrate to the output IDT 2, which performs the inverse transformation [5]. The acceleration measurement process consists of the following steps: first, acceleration causes deformation of the material; second, internal mechanical stresses cause the density to change; third, the change in the material density affects the wave propagation velocity, and, consequently, the wave propagation time along the substrate changes. It is the time delay that can be used to judge the change in the acceleration of the object. Typical design configurations of these sensors include delay lines and resonators, which are structured to maximize sensitivity and measurement accuracy.

Implementation of wireless data transmission. The basic setup includes a transmitter connected to a SAW accelerometer that converts an electrical signal into a radio frequency signal. The receiver receives this signal and processes it to interpret the data [6]. There are several ways to implement data transmission from the sensing element.

The first method is shown in Figure 1a, when the signal is fed to antenna 4, from which it enters the exciting IDT 3, which generates a SAW that propagates to the receiving IDT, where the reverse conversion into an electrical signal occurs and the data is transmitted via antenna 5. The described method is closest to the wire pickup method. However, its disadvantage is possible interference between the antennas.

The second method (Fig. 1b) involves using one antenna for both receiving and transmitting the signal and placing two reflector blocks, the difference in the distance between their paths can be found by subtracting one from the other: $r_2 - r_1$. In this way, it will be possible to avoid interference between the antennas. But the disadvantage of this will be the potential excessive weakening of the SAW amplitude, which will have to pass through the first reflector twice. The next two methods allow you to avoid this.

The third method (Fig. 1c) suggests placing the reflectors on different sides of the exciting IDT. The disadvantage may be the subsequent passage of the wave front through the IDT on the return path and the superposition of the waves on each other, which will cause an echo and interfere with the identification of the useful signal.

The fourth method suggests using 2 delay lines (Fig. 1d). However, a disadvantage may be the mutual influence of the fronts of waves simultaneously propagating along the surface, as well as the occurrence of an electromechanical connection between two IDTs.

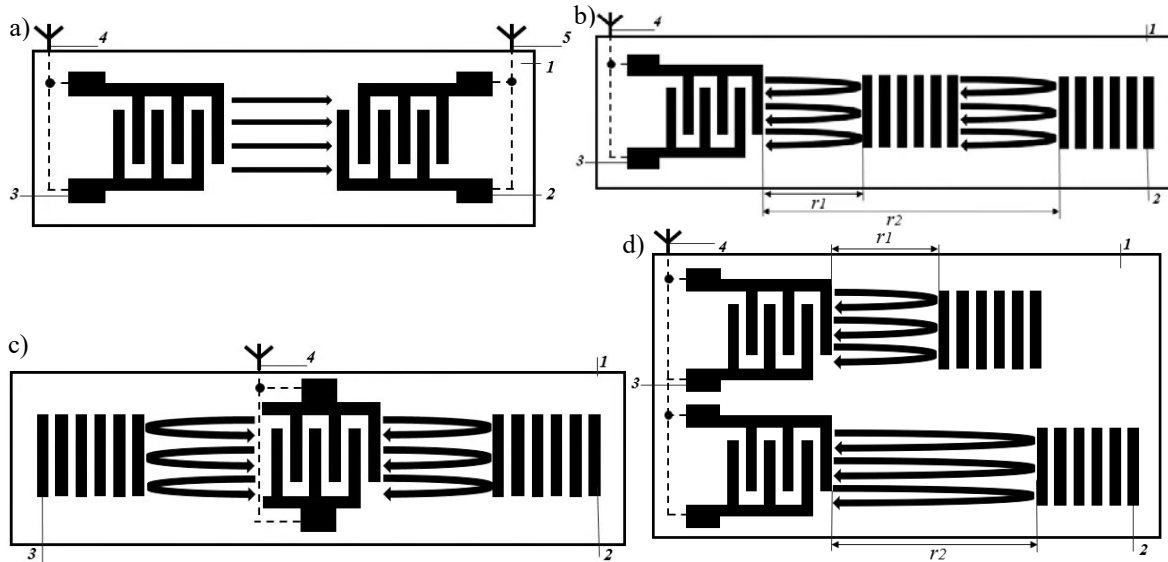


Fig. 1. Topologies of the sensitive element for data transmission

COMSOL Modeling for Bidirectional Signal Transmission. In order to investigate the methods described above, a simplified model was built in the Comsol Multiphysics environment (Fig. 2a). The dimensions of the model were $3.75\lambda \times 0.25\lambda \times 3\lambda$, where λ is the wavelength, which is 0.796 mm. The model specifies two electrodes with a height of 0.01λ , one of them is grounded, and the other is assigned the Terminated condition with the Circuit type. A sinusoidal signal with an amplitude of 1 V and a period of $0.2 \mu\text{s}$ is fed to this electrode.

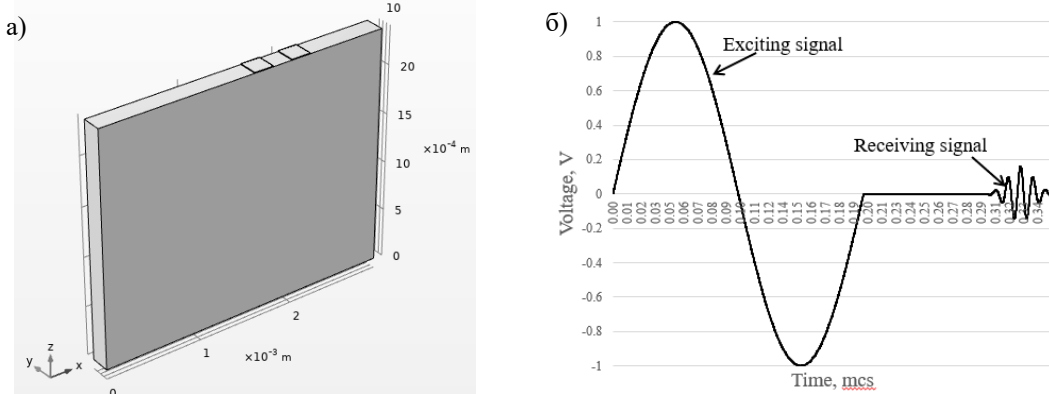


Fig. 2. Simplified model of the sensitive element and graph of voltage change on the IDT

The voltage change graph is shown in Figure 2b. As can be seen, the signal amplitude has decreased by 5 times due to losses. This method of setting the conditions for signal feed and pickup from one IDT is promising for further research.

Conclusion. The report examined the principles of wireless data transmission for a SAW accelerometer. Four methods of signal transmission and reading were proposed. A multiphysical model was developed for calculating the parameters and voltage graphs were obtained.

The work was carried out with the financial support of the Russian Science Foundation within the framework of the RSF grant 23-79-10259 in the form of subsidies in the field of scientific and scientific-technical activities.

REFERENCES

1. **Yihan Zhao et al.** Equal-strength beam design of acoustic wave accelerometers. 2023 Phys. Scr. 98
2. **Juan Zhang, Wen Hua Cheng, Hao Wang, Lei Zhang, Xiang Rong Li, Hong Shuai Ma, Jun Qi Pang & QiuLin Tan.** Langasite-based SAW high-temperature vibration sensor with temperature decoupling. Science China Technological Sciences. Volume 67, pages 1946–1956, 2024

3. **L. Reindl, I. Shrena, S. Kenshil and R. Peter.** Wireless measurement of temperature using surface acoustic waves sensors, IEEE International Frequency Control Symposium and PDA Exhibition Jointly with the 17th European Frequency and Time Forum, 2003. Proceedings of the 2003, Tampa, FL, USA, 2003, pp. 935-941
4. **Debdyuti Mandal, Sourav Banerjee.** Surface Acoustic Wave (SAW) Sensors: Physics, Materials, and Applications. *Sensors* 2022, 22(3), 820
5. **Shevchenko S. et al.** Surface-Acoustic-Wave Sensor Design for Acceleration Measurement. *Sensors* 2018. 18(7), 2301
6. **Fabian Lurz et al.** Reader Architectures for Wireless Surface Acoustic Wave Sensors. *Sensors* 2018, 18(6), 1734

Yu. A. LITVINENKO, O. A. STEPANOV
(Concern CSRI Elektropribor, ITMO University, St. Petersburg, Russia)

THE FEATURES OF FEDERATED FILTERING METHODS IN NONRECURSIVE MEASUREMENT PROCESSING

The paper discusses the features of decentralized processing of measurement information, which is aimed to obtain the desired estimate of the state vector of a dynamic system by weighing the local estimates generated in distributed measuring modules. The recursive and non-recursive schemes of measurements processing in federated filters are compared. Conditions for recursive and non-recursive schemes are considered that ensure the coincidence of the estimates and calculated covariance matrices generated in federated filters and the optimal centralized Kalman filter. A methodical example of the Wiener sequence estimation is given to illustrate the methods under consideration.

It is known that the problem of designing algorithms for estimation of a dynamic system state with measurement redundancy can be solved on the basis of both centralized processing, when all available measurements are fed into a single centralized filter, and different decentralized schemes, or so-called federated filtering (FF) algorithms [1-4].

The main advantage of a centralized scheme is the possibility of obtaining an RMS-optimal estimate when solving the estimation problem for a linear system using linear measurements and the Gaussian nature of the system noise and measurement errors. This is achieved through centralized processing of all measurements by means of an optimal Kalman filter that recursively processes the entire set of measurements. However, the disadvantages of centralized schemes in comparison with FF methods are their lower reliability and higher computational load.

The essence of FF methods is that primary processing of information is carried out in so-called local filters (LF), in which local estimates of the dynamic system state are generated based on measurements obtained in local measuring modules. A general estimate is calculated by averaging the local estimates in the so-called master filter. The main advantages of FF algorithms are lower computational load compared to centralized Kalman filters and their immunity against false measurements obtained in one of the measuring modules [1]. FF algorithms have recently been widely used to solve estimation problems based on data from distributed sensors, in particular, in relation to problems of collaborative navigation of unmanned vehicles [7-10]. The features of recursive FF algorithms and their application to navigation information processing are discussed in detail in [1]. Further development of such algorithms is discussed in [2,4-6], which demonstrate the possibility of ensuring the so-called guaranteeing properties of the FF, the essence of which is that the actual error of the general estimate does not exceed the calculated error obtained in the master filter. The main disadvantage of the FF is the fact that in the general case, these algorithms do not provide optimal estimates, and the accuracy characteristic calculated in the master filter is not the actual covariance matrix of the generated estimate error. Although for some special cases the conditions for the so-called matched adjustment of local filters under which it is possible to derive an optimal estimate in the master filter are formulated [2,4], the authors are not aware of any general answer to the question about the conditions ensuring the coincidence of the estimates and calculated covariance matrices generated in the FF with the results derived in the optimal centralized Kalman filter.

It should be emphasized that the above algorithms are recursive with respect to the incoming measurements. At the same time, in the last decade, there has been an increased interest in nonrecursive processing methods, including algorithms based on factor-graph optimization [11-12]. A number of works show the advantage of nonrecursive schemes over traditional recursive algorithms, for example, the Kalman filter. However, to date, FF methods have only been studied for traditional recursive schemes for processing incoming measurements, and possible advantages of nonrecursive FFs have not been considered in the literature. In this regard, the aim of the proposed work is to study the features of FF methods in the implementation of nonrecursive schemes for processing measurements.

The paper formulates the problem of estimating an unknown random vector x when processing measurements coming from m sensors. The solution of the filtering problem is given for a centralized

filter that provides an optimal estimate and an FF that includes m local filters. We consider the recursive and nonrecursive schemes of solution for the both variants of the filter construction. With regard to the traditional recursive FF, the conditions for the matched adjustment of local filters are formulated, while it is noted that in most estimation problems, they do not provide an optimal solution. Also given are the conditions for matched adjustment for an FF designed using a nonrecursive scheme, but it is proved that they ensure the coincidence of the estimates and covariance matrices of the FF estimates and the centralized (optimal) filter in the general case.

As an illustration, an example of estimating the Wiener sequence using the measurements in two measuring modules is given. For the example considered, the conditions for FF adjustment for recursive and nonrecursive measurement processing schemes are compared. It is shown that in order to ensure an optimal FF estimation for recursive processing, it is necessary to comply with the FF adjustment conditions that require additional consideration of measurement noise variances, whereas for a nonrecursive scheme, this is not required in the FF adjustment conditions.

Thus, the paper studies the features of a nonrecursive FF in comparison with a traditional recursive processing scheme. An important difference is shown for a nonrecursive FF, consisting in the possibility of obtaining an optimal state vector estimate, whereas for a recursive processing scheme, FF methods provide optimal estimates only for special cases.

This work was supported by the grant from the Russian Science Foundation, project no. 23-19-00626, <https://rscf.ru/project/23-19-00626/>.

REFERENCES

1. Carlson, N.A., Federated filter for fault-tolerant integrated navigation systems, *AGARDograph 331, Aerospace Navigation Systems*, June 1995, pp. 265-280.
2. Tupysev, V.A., Methods for designing filtering algorithms with guaranteed quality of parameter estimation in problems of navigation information processing, Dr. Sci. Dissertation, St.Petersburg, 2011.
3. Stepanov, O.A., *Osnovy teorii otsenivaniya s prilozheniyami k zadacham obrabotki navigatsionnoi informatsii* (Fundamentals of the Estimation Theory with Applications to the Problems of Navigation Information Processing), Part 2, *Vvedenie v teoriyu otsenivaniya* (Introduction to the Estimation Theory), St. Petersburg: TsNII Elektropribor, 2012.
4. Tupysev, V.A. and Litvinenko, Yu.A., The Effect of the local filter adjustment on the accuracy of federated filters”, *Proc. MICNON-2015*, pp. 349-354.
5. Zhang, H., Lennox, B., Goulding, P.R., and Wang, Y., Adaptive information sharing factors in federated Kalman filtering, *The 15th IFAC World Congress*, Barcelona, Spain, 2002, July 21–26, pp. 664–664.
6. Selezneva, M.S., Proletarsky, A.V., Neusypin, K.A., and Zhang Lifei, Modification of the federated Kalman filter using the observability degree criterion of state variables, *26th St. Petersburg Int. Conf. on Integrated Navigation Systems*, St. Petersburg: Elektropribor, 2019, pp.
7. Maier, A., Kiesel, S., and Trommer, G.F., Performance analysis of federated filter for SAR/TRN/GPS/INS integration, *Gyroscopy and Navigation*, 2011, vol. 2, no. 4, pp. 293-300.
8. Weiwei Lyu, Xianghong Cheng, and Jinling Wang, Adaptive federated IMM filter for AUV integrated navigation systems. *Sensors 2020*, 20, doi:10.3390/s20236806
9. Pengfei Zhang, Zhenhua Ma, Yin He, Yawen Li, and Wenzheng Cheng, Cooperative positioning method of a multi-UAV based on an adaptive fault-tolerant federated filter. *Sensors 2023*, 23, <https://doi.org/10.3390/s23218823>
10. Tanik Ayabakan, Feza Kerestecioglu. Fault tolerant indoor positioning based on federated Kalman filter. *Journal of Signal Processing Systems*, 2024, pp. 273–285
11. Weisong Wen, Tim Pfeifer, Xiwei Bai, and Li-Ta Hsu, Factor graph optimization for GNSS/INS integration: A comparison with the extended Kalman filter, *NAVIGATION*, 2021; 68:315–331.
12. Stepanov, O.A., Isaev, A.M., Motorin, A.V., Litvinenko, Yu.A., and Zolotarevich, V.P., Estimation algorithms based on factor-graph optimization vs. Bayesian estimation algorithms for navigational data processing: Differences and interrelation , 31st St. Petersburg Int. Conf. on Integrated Navigation Systems, St. Petersburg: Elektropribor, 2024, pp. 336-344.

V. BONDARENKO

(Concern CSRI Elektropribor JSC, St. Petersburg, Russia)

DEVELOPMENT OF A 6-AXIS ROBOTIC MANIPULATOR FOR STEREOTACTIC SURGERY

The paper presents the results of development of a 6-axis robotic manipulator for stereotactic surgery. The robotic manipulator can be used for the surgical treatment of deep-located brain tumors, for the intracerebral implantation of electrodes for brain stimulation in patients with Parkinson Disease, for the treatment of epilepsy, etc. The experimental model of the low-cost robotic manipulator is described in details. Basic requirements for stereotactic robotic manipulator are as follows: workspace is not less than 0.4 m³, position accuracy is ± 0.5 mm, the ability to change the angle of the stereotactic instrument while the coordinates of its end point are the same, compatibility with the surgical navigation systems, and compliance with the requirements for medical equipment. The results of a phantom testing of the manipulator in the neurosurgery operation room using the surgical optical navigation system showed that it is possible to use this manipulator for all types of stereotactic surgery interventions on the brain.

I. Introduction. Currently brain tumors are a very serious problem. The incidence is from 2 to 25 people per 100,000 of populations annually. Brain tumors represent approximately 6-8% of all tumor diseases. The widespread use of tomography has significantly improved the diagnosis of the brain tumors. Many tumors are localized at the motor, visual or speech regions of the brain (approximately 35% of all brain tumors) [1-3]. In this case, tumor removal can lead to damage of the important areas of the brain. So surgical interventions at those areas are very high-risk and are rarely performed. At the same time, the rapid development of surgical navigation and minimally invasive neurosurgery have made it possible to surgically treat brain tumors through stereotactic operations. Stereotactic operations comprise the aiming insertion of a stereotactic instrument through a burr hole on the skull into pre-planned points of the brain using special neurosurgical manipulators. This method allows performing operations on the deep and functionally significant parts of the brain, otherwise inaccessible to standard open neurosurgical interventions. Also, it significantly reduces the risk of postoperative complications. Stereotactic operations are also used for implanting intracerebral electrodes for stimulation in patients with Parkinson disease, for the diagnosis and treatment of epilepsy, and in some other brain diseases [4]. For many years the mechanical frame systems have been used for this type of operations. In 1993 Joint-stock company State Research Centre of the Russian Federation – Concern CSRI Elektropribor and N.P. Bechtereva Institute of the Human Brain of the Russian Academy of Sciences developed and launched serial production of the stereotactic mechanical manipulator named “Oreol” shown in Fig.1 [5,6,7]. Currently, the development of the surgical technique shows a tendency to strengthen the role of automation. The successful introduction of surgical robots in general surgery, cardiac, and ophthalmic surgery aroused interest in the use of robotic manipulators for neurosurgery. Many clinics have been using stereotactic robotic manipulators for several years. The use of robotic manipulators for stereotactic biopsy and implantation of electrodes shows the successful developments of this area [8]. Stereotactic robotic manipulators have many advantages. Some of the most important of them are reducing the complexity of the neurosurgical intervention, reducing the risk of the human factor,



Fig. 1. The mechanical stereotactic manipulator «OREOL»

increasing accuracy of aiming for the target points, and shortening the total duration of neurosurgical interventions [9]. But most of the modern manipulators for stereotactic neurosurgery are expensive and need special operating space. The main participants in the market of stereotactic robots are "Renishaw Plc" (UK) and MedTech SAS" from France (in 2014 was bought by a Zimmer Biomet USA). Both companies sell stereotactic robotic manipulators with a 5 or 6 axes. Price of these systems is about a one million USD. Therefore, creation of an inexpensive and compact robotic manipulator for stereotactic neurosurgery is highly pertinent.

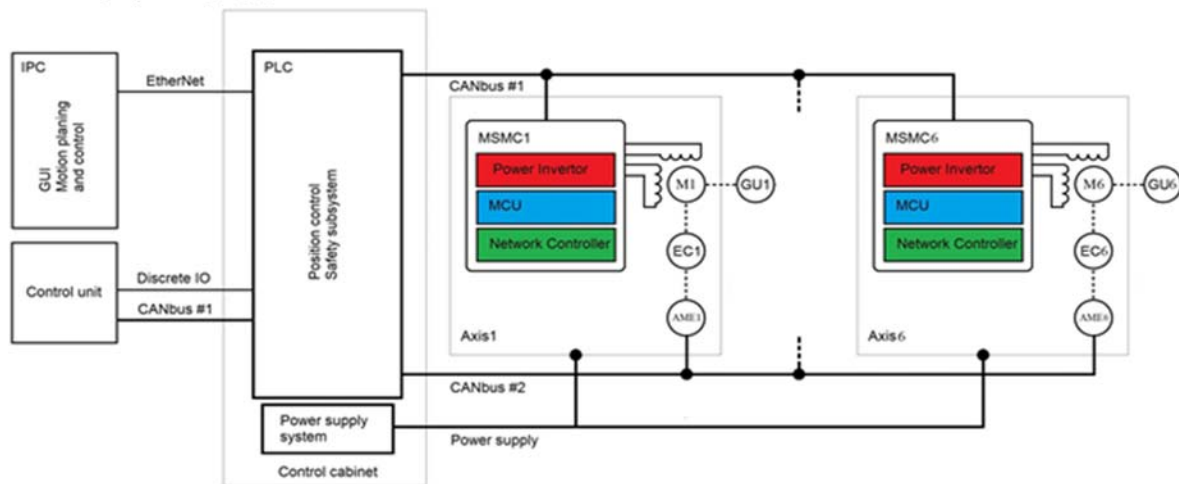


Fig. 2. The functional scheme of the robotic manipulator

II. Concept. The main idea of this project is to create low-cost medical equipment suitable for effective and safe surgical treatment of common diseases of the central nervous system. Basic requirements for stereotactic robotic manipulator, given by medical partners are as follows: workspace is not less than 0.4 m³, position accuracy is ± 0.5 mm, the ability to change the angle of the stereotactic instrument while the coordinates of its end point are the same, compatibility with optical and electromagnetic surgical navigation systems, and compliance with the requirements for medical equipment. This project's main goal of price reduction is achieved by eliminating several expensive parts such as torque motors, precision encoders, and slip rings. The function scheme of the manipulator is shown in fig.2. The stepper motor M and harmonic gear unit GU were chosen to drive all axes. Design life of the chosen gear units is 15000 hours and its cost in Russia is less than 1000 USD. Absolute multi turn encoder AME was used for a close loop. Bearing lifetime of the encoder is 3.6×10^8 revolutions and a mean time to dangerous failure (EN ISO 13849-1) is 230 years. This type of encoder is widely used and it is available in Russia for 400 USD. Patient safety, which is always of the highest priority, was the main reason for using an electromagnetic brake clutch EC for each axis. The miniature stepper motor controller MSMC is used on each axis to reduce wiring and provide electromagnetic compatibility. Two CAN-buses are used to control drives and for feedback. This architecture makes it possible to fully stop the manipulator and keep its position during surgical intervention. As we know, a 6-axis robotic manipulator can reach any point in its area with any given orientation, so the described system has 6 axes. Programmable logical controller PLC is used for position control and as a safety system. Power supply system makes it possible to power parts of the system

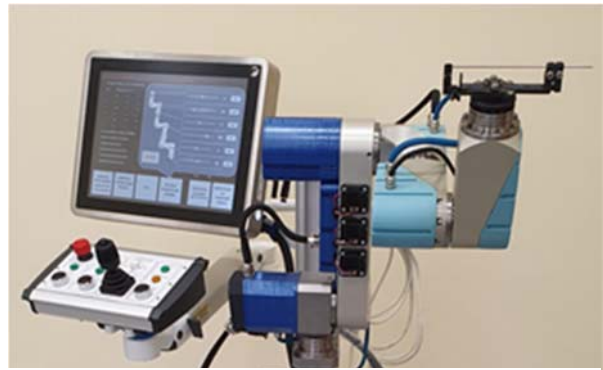


Fig.3 The prototype of the system

separately. It can power down all of MSMC and to activate all EC at the same time for keeping orientation of manipulator in case of power failure or any emergency situation. The MSCM and AME has internal safety subsystems, so PLC receives their actual state each 10 ms via CAN-bus. The PLC continuously monitors the rate and position of all axes. If an axis is blocked or its rate of movement is too fast, PLC will immediately activate the emergency stop procedure. The same procedure will activate in case of emergency state of any MSCM or AME. Graphic user interface, motion planning and all calculations are based on industrial personal computer IPC with a touch screen. The data exchange between PLC and IPC is managed via fast Ethernet connection. The motion of manipulator is controlled by operator via joystick placed in the control unit CU. CU also has mechanical buttons that make it possible to change the operation mode, control power supply and immediately stop the manipulator in case of emergency situation. Therefore, the manipulator is quite simple and most parts of it have a low cost.



Fig.4 Situational tests in the neurosurgical operating room

III. The Prototype of the System. The prototype of the system has been created. The prototype is shown in fig.3. The prototype has been developed as a combination of all main parts fixed to the common base. The manipulator, control unit, control cabinet and industrial PC are mechanically connected via pivot arms to the special made medical cart. The prototype of a manipulator was manufactured using simple aluminum milled parts. The bearings of the gearboxes are used like a load-bearing. Stepper motors and encoders are enclosed with plastic decorative covers made by 3D printing. Control unit is made of aluminum and has a plate-face with pictograms for operator. A compact, low-profile joystick utilizing non-contact Halls effect is placed at the centre of control unit. Joystick has a connection via PLC thru CAN-bus. The 15-inch IPC has a stainless steel housing specially designed to meet harsh environment applications. Assembled parts of the manipulator were measured by using a high precision coordinate measuring machine. Obtained data are used for calculations in algorithms of motion planning and control.

IV. Motion planing and control. The relative position and orientation of the end-effector frame and a base-frame are required to control any manipulation system. The mentioned frames relations can be determined using the kinematics tasks. The screw theory and dot product of exponentials have been used to solve the direct and inverse kinematics. The exponentials-based approach has been selected as the fastest approach which can provide quick calculations because it utilizes integration instead of derivatives [9]. In addition to the high precision of calculation, high precision of mechanical parts is required to provide total precision, which would lead to increasing of the manipulator cost. To avoid the increased

manufacturing cost, the deviations have been measured and taken into account on side of kinematics model. All screw axes have been determined after measuring the relative orientations of the joints with high accuracy (10^{-8}), since manufacturing errors had to be considered to ensure high accuracy. To solve the direct problem, the exponential products have been used. The inverse kinematics task has been solved using Newton-Raphson's iterative numerical root finding method. The problem arises from numerical calculation, where the small numerical errors can lead to violation of the basic properties of the special orthogonal group SO(3) elements. Various methods have been tested to solve this problem. Most accurate is the projection of numerical values into SO(3) space, i.e., kind of normalization. The trajectory planning task was the next task. The robot joints control has been provided by velocity control since the speed of motion has to be low enough to allow good control in any dangerous situation. Since the control should be independent of the environment and its own dynamics, the control by velocity is the preferred technique. The specific method of error derivation was selected to be used in control. The calculation has been done in task space according to (1), where R_d is the desired end-effector orientation and p_d is desired coordinates, the current orientation and current position has been marked without any index.

$$X_e(t) = \begin{bmatrix} \log R^T(t) R_d(t) \\ p_d(t) - p(t) \end{bmatrix} \quad (1)$$

Except the screw control error calculation, the screw trajectory generating method has been implemented to provide the smooth trajectory of motion for end-effector according to (2) where $s \in [0,1]$

$$X(s) = X_{start} \exp(\log(X_{start}^{-1} X_{end})s) \quad (2)$$

This approach provides end-effector motion simultaneously changing the orientation and position of the tool from the initial to the target configuration [10]. Based on the requirements for use of surgical navigation system, the manipulator has two special modes for the operator. First mode makes it possible to move stereotactic instrument in three dimensions. Second one makes it possible to change the angle of the stereotactic instrument while the coordinates of its end point remain unchanged. All movement is easy to control by joystick. A graphic user interface makes it possible to preset stereotactic instrument near one of the 24 anatomic zones of the skull by a single touch. At the same time, the configuration of the manipulator is designed for optimal visibility for the surgical navigation system. The safety subsystem checks all parameters of the manipulator and its parts in real time. The main features of the safety subsystem are data integrity verification, over speed, over current, over temperature and obstacle control. The safety subsystem has logging for all types of alarms and keeps the state of the system before an emergency event.

V. Tests. After manufacturing, the prototype of manipulator has passed the position accuracy validation test. The position accuracy test was made for each axis. The regular 24-face polygon and optical autocollimator was used. The measurements have confirmed the position accuracy is 55 ± 5 arc-seconds for any axis. A high precision coordinate measuring machine was used for testing. The position accuracy of 0.35 mm in terms of ISO 9283 was confirmed. The prototype of the system has passed situational tests in the neurosurgical operating room. Phantom model was used as a test object [11]. The adhesive markers have been used for intraoperative registration and as simulators of intracerebral target points. General Electric Healthcare Discovery 710 PET/CT machine was used to scan a phantom as follows: slices 0.625 mm and a pixel size is 0.5×0.5 mm. Tomography data were loaded to the Medtronic StealthStation S7 system that enables real-time optical surgical navigation. During tests, the surgical navigation system tracked the position of the Medtronic Navigus probe mounted at the end-frame of the manipulator. The software of surgical navigation system displays data from a variety of perspectives: axial, sagittal, coronal, oblique. During all tests a virtual extension of the end point of the probe was used. The manipulator, a probe and software example screen are shown in fig.4. The real part of the probe is marked as blue and a virtual part is marked as yellow. The targeting was realized by three simple steps.

At first, the probe was automatically moved by manipulator to the nearest anatomic zone. At the second step, the movement of manipulator in three dimensions made it possible to find alignment of the end point of the virtually extended probe with the target point in orthogonal planes of the brain. At the third step, it was possible to change the angle of the probe while the coordinates of the end point of the probe virtual extension remained unchanged. The joystick was only used to control of the manipulator. After targeting, the probe was replaced with a stereotactic instrument, immersed into the phantom. The length of the stereotactic instrument was equal to a virtually elongated probe. During all tests, the target marks of the phantom were precisely achieved by stereotactic instrument. Modern optical measurement solution provides real-time 3D position tracking of markers attached to tools. Measurement data is captured with sub-millimeter accuracy [12]. During tests, it was possible to move end-frame of the manipulator by steps as small as 0.06-0.07 mm in any direction and optical navigation system displayed the new value of the measured data after 2-3 steps only.

VI. Conclusion. The prototype of stereotactic manipulator was produced. During the tests the position accuracy of 0.35 mm in terms of ISO 9283 was confirmed. The manipulator showed the ability to change the angle of the stereotactic instrument while the coordinates of its end point remained the same. It has successfully passed phantom tests in the neurosurgery operation room with the use of the surgical optical navigation system. The design of the prototype makes it possible to move the stereotactic instrument more accurately than the surgical optical navigation system can measure. Tests showed it possible to use this manipulator for all types of stereotactic surgery interventions on the brain including biopsies, intracerebral implantation of electrodes, as well as stereotactic destruction of intracerebral tumors and subcortical structures in functional neurosurgery. While the system's working load capacity is somewhat limited at 1 kg, the low cost of parts, precise controls and other features make it useable for different applications. The development of commercially available manipulator is underway.

REFERENCES

1. Martynov B.V., Kholyavin A.I., Nizkovolos V.B., Parfenov V.E., Trufanov G.E., Svistov D.V. Stereotactic cryodestruction of gliomas / Chernov M.F., Muragaki Y., Kesari S., McCutcheon I.E. (eds): Intracranial Gliomas. Part III - Innovative Treatment Modalities. Prog Neurol Surg. Basel, Karger, 2018, vol 32, pp 27-38.
2. A.I. Kholyavin, V.B. Nizkovolos, V.N. Ochkolyas, A.D. Anichkov, A.F. Gurchin, R.Yu Seliverstov, T.Yu.Skvortsova. Stereotaxicheskoe neirokhirurgicheskoe lechenie glial'nykh opukholei golovnogo mozga s primeneniem kriokhirurgii i pozitronno-emissionnoi tomografii: uchebno-metodicheskoe posobie/ pod red. A.D.Anichkova. Spb: RIC PSPbGMU, 2018. 20 p.
3. B.M. Nikiforov. Klinicheskie lektsii po nevrologii i neirokhirurgii. – SPb: Piter, 1999 r. – 352 p.
4. W.J. Marks, Jr (ed.). Deep brain stimulation management. – Cambridge University Press, 2010. – 168 p.
5. A.D. Anichkov, M.A. Nikitin, Yu.Z. Polonskii, A.B. Popov, V.B. Nizkovolos, A.V. Oblyapin, N.G. Shkurina, Novaya universal'naya stereotaksicheskaya sistema, Aktual'nye voprosy stereoneirokhirurgii epilepsii, pod red. V.P. Bersneva. – SPb.: RNKhI, 1993, pp. 177–187.
6. M.A. Nikitin, Stereotaksicheskii manipulyator «Oreol», Klinicheskii stereotaksis. Opyt i perspektivy primeneniya otechestvennogo neirokhirurgicheskogo manipulyatora «Oreol»: SPb., 2001, pp. 6-8.
7. Yu.Z. Polonskii, A.I. Kholyavin, B.V. Martynov, V.E. Parfenov, G.E. Trufanov, Bezramnaya raschetnaya magnitno-rezonansnaya tomografiya so stereotaksicheskimi manipulyatorami klassa «Oreol», Vestnik Rossiiskoi Voenno-meditsinskoi akademii 2009 – № 4 (28), pp. 71-78.
8. D. von Langsdorff, P. Paquis, D. Fontaine, In vivo measurement of the frame-based application accuracy of the neuromate neurosurgical robot, J Neurosurg. – 2015. – Vol. 122(1), pp. 191-194.
9. F. Cardinale, M. Rizzi, P. d'Orio et al., A new tool for touch-free patient registration for robot-assisted intracranial surgery: application accuracy from a phantom study and a retrospective surgical series, Neurosurg Focus. – 2017. – Vol. 42 (5). – E8.
10. M.L. Kevin, C.P. Frank, Modern robotics: mechanics, planning and control, Cambridge University Press, 2017.
11. A.I. Kholyavin, V.B. Nizkovolos, A.A. Bogdan. Assessment of the Targeting Quality of a Stereotactic Instrument to an Aiming Point in the Brain Using a Frameless Navigation System / Biomedical Engineering (2018) Vol.52, Issue 2., p. 92-95.
12. A.D. Wiles, D.G. Thompson, D.D. Frantz, Accuracy assessment and interpretation for optical tracking systems, Medical imaging 2004: visualization, image-guided procedures, and display. International Society for Optics and Photonics, pp. 421–432.

E.V. BARINOVA, I. V. BELOKONOV, I. A. TIMBAI
(Samara National Research University, Samara)

PROBLEMS OF ANGULAR MOTION OF CUBESAT 6U NANOSATELLITES IN LOW EARTH ORBITS

This paper study the passive angular motion of the 6U CubeSat nanosatellites relative to its center of mass in low circular orbits under the influence of aerodynamic and gravitational moments, taking into account the features of the mathematical model of the aerodynamic drag force. A system of equations for determination of the nanosatellite equilibrium positions is obtained. It is shown the possibility of the occurrence of resonant motion modes.

Introduction. When performing a number of target tasks, it is necessary to maintain a certain orientation of the nanosatellite (NS), while in order to reduce energy consumption, preference is given to passive or combined stabilization systems. When designing passive stabilization systems, information on stable equilibrium positions under the action of external moments and an analysis of the uncontrolled motion of the NS relative to the center of mass are used. Therefore, an important task is to determine the equilibrium positions, as well as to study the motion of the NS in their vicinity under the action of gravitational and aerodynamic moments, which are predominant in low circular orbits. Since CubeSat NS have the shape of a rectangular parallelepiped, which entails changes in the mathematical model of the aerodynamic drag force, a new class of problems arises related to the search for equilibrium positions and the study of the possibility of the emergence of resonant motion modes.

Previously, the authors obtained a system of equations for determining the equilibrium positions of the angular motion of the CubeSat 1U–3U NS in a circular orbit under the action of aerodynamic and gravitational moments and found its analytical solution for two special cases [2, 3]. In development of the previously conducted studies, this paper analyzes the dynamics of CubeSat 6U nanosatellites. A system for determining the equilibrium positions in the orbital coordinate system under the action of aerodynamic and gravitational moments was obtained. For the special case of the displacement of the center of pressure from the center of mass along one of the main axes of inertia, analytical expressions were obtained. For the case of using aerodynamic stabilization along the velocity vector of the center of mass, the possibility of occurrence of resonant motion modes was shown and recommendations for their prevention were given.

Passive angular motion of CubeSat 6U nanosatellites relative to the center of mass under the action of aerodynamic and gravitational moments. Euler angles are used to orient the NS-related coordinate system relative to the trajectory: α is the spatial angle of attack, ψ is the precession angle, φ is the angle of proper rotation.

At the considered altitudes of motion, it is assumed that the flow around the nanosatellite is free-molecular and the impact of gas molecules is absolutely inelastic. In this case, the aerodynamic force is the drag force, which is determined by the area of the projection of the NS on the plane perpendicular to the velocity vector of the incoming flow [1]. Unlike the CubeSat 1U-3U NS, the CubeSat 6U NS has all three different linear dimensions ($l_x > l_z > l_y$), and, therefore, the expression for the area of the projection of the NS on the plane perpendicular to the velocity vector of the incoming flow is also different:

$$S_x \cdot \tilde{S}(\alpha_n, \varphi) = S_x \cdot \left(|\cos \alpha_n| + \sin \alpha_n \left(\frac{l_x}{l_y} |\sin \varphi| + \frac{l_x}{l_z} |\cos \varphi| \right) \right), \quad (1)$$

where $S_x = l_y l_z$ is the characteristic area of the NS (in this case, the area of the smallest face).

The equations of spatial motion of a NS relative to the center of mass under the action of aerodynamic and gravitational moments in a circular orbit can be written in the following form:

$$\mathbf{I}\dot{\boldsymbol{\omega}} + \boldsymbol{\omega} \times \mathbf{I}\boldsymbol{\omega} = \mathbf{M}_a + \mathbf{M}_g, \quad (2)$$

where \mathbf{I} is the NS inertia tensor; $\boldsymbol{\omega}$ is the NS absolute angular velocity vector; \mathbf{M}_a is the aerodynamic moment; \mathbf{M}_g is the gravitational moment.

Equilibrium positions of the CubeSat 6U nanosatellite under the action of aerodynamic and gravitational moments. In [2, 3], the equilibrium positions of the angular motion of a dynamically symmetric CubeSat 1U – 3U nanosatellite in a circular orbit under the action of aerodynamic and gravitational moments are determined for two special cases: displacement of the center of pressure of a dynamically symmetric NS from its center of mass along three coordinates and a NS with three different principal moments of inertia when the center of pressure is displaced from the center of mass along one of the principal axes of inertia.

In this paper, a system of equations is obtained for determining the equilibrium positions of a CubeSat 6U nanosatellite under the action of aerodynamic and gravitational moments, taking into account the features of the aerodynamic moment model. Its analytical solution is also found for the particular case of a CubeSat 6U NS with three different principal moments of inertia when the center of pressure is displaced from the center of mass along one of the principal axes of inertia.

Resonance Motion Modes. When using uniaxial aerodynamic stabilization of the longitudinal axis of the NS relative to the velocity vector, it is necessary to take into account the possibility of occurrence of resonant motion modes. Resonant motion modes are manifested themselves in a sharp change in the amplitude of oscillations along the spatial angle of attack. In this paper, the resonant motion modes are studied in accordance with the algorithm described in [4], considering the differences caused by the features of the 6U format. It was found that, compared to the case of CubeSat 1U-3U [4], the CubeSat 6U NS has a greater number of resonant frequency ratios generated exclusively by the shape of the nanosatellite. For the case of "direct" precession, there are 7 ratios compared to 5, for the case of "reverse" - 3 ratios compared to 1. In addition, ratios were obtained for determining the critical values of the longitudinal angular velocity of the NS, at which the conditions for occurrence of resonant motion modes are met.

Conclusion. The results presented in this work may be useful for developers of CubeSat 6U nanosatellite, which continue to gain popularity at present.

The research was supported by the Russian Science Foundation grant No. 23-67-10007, <https://rscf.ru/project/23-67-10007/>.

REFERENCES

1. **Beletskii V.V.** Dvizhenie iskusstvennogo sputnika otnositel'no tsentra mass (Motion of an Artificial Satellite Relative to the Center of Mass), Moscow: Nauka, 1965.
2. **Barinova E.V., Timba, I.A.** Relative equilibria of dynamically symmetric CubeSat nanosatellite under the action of aerodynamic and gravitational torques, Vestnik of Samara University. Aerospace and Mechanical Engineering, 2019, Vol. 18, No. 2, pp. 21-32 (in Russian).
3. **Barinova E.V., Timbai I.A.** Determining of Equilibrium Positions of CubeSat Nanosatellite under the Influence of Aerodynamic and Gravitational Moments. in *27th Saint Petersburg International Conference on Integrated Navigation Systems. ICINS 2020. Proceedings. 2020.*
4. **Barinova E.V., Belokonov I.V., Timbai I.A.** Preventing Resonant Motion Modes for Low-Altitude CubeSat Nanosatellites. *Gyroscopy and Navigation.* 2021. Vol. 12. № 4. pp. 350–362.

I.S. ARKHIPOV
(Saint Petersburg State University, Saint Petersburg)

MULTI-AGENT REAL-TIME OPERATING SYSTEM FOR COLLABORATIVE ROBOT CONTROL

The article presents a multi-agent real-time operating system designed for collaborative robot control. It covers the system architecture, current functionalities, and plans for further development, as well as key features that distinguish this solution from existing analogues.

Introduction. In recent years, multi-agent technologies have attracted increasing attention, especially in the context of collaborative robot control. Researchers are actively working on the development of integrated systems that combine multiple end-devices with AI-agents into a single ecosystem. Specialised technological solutions are needed to address such challenges. Although current approaches are often based on general-purpose real-time operating systems such as FreeRTOS, the use of specialised software can greatly simplify the process. This paper will present a developed solution focused on real-time multi-agent management.

Review of existing solutions. As an example, consider one of the most popular operating systems on the market, FreeRTOS (<https://github.com/FreeRTOS>). FreeRTOS is open source with an MIT licence and is supported by Amazon. FreeRTOS supports over 35 microprocessor architectures. The Task Manager supports both preemptive and cooperative multitasking, as well as process priorities, semaphores, and queues. It has several narrowly focused variants, such as Amazon FreeRTOS, SafeRTOS, OpenRTOS, and ESP-IDF FreeRTOS. However, the operating system does not have a specialised API for collaborative robot control, such as a network interface. This interface is usually implemented as libraries by hardware manufacturers.

Proposed solution. This paper presents a specialised operating system called Martos (<https://github.com/IvanArhipov1999/Martos>), designed with a focus on multi-agent technology and collaborative robot control. Martos includes a non-preemptive task manager that provides efficient resource allocation, minimising the overhead of context switching. The system also features memory management mechanisms to optimise the use of available resources and prevent memory leaks.

In addition, Martos provides timer functionality, which is critical for synchronising agent actions and performing time-sensitive tasks. A network interface allows agents to communicate with each other and share data in real time, enabling more efficient, collaborative problem solving.

The operating system is developed in the Rust programming language, which is known for its security and performance, making Martos a reliable solution for embedded systems. In addition, Martos has been successfully ported to the ESP32 and ESP32-C6 microcontrollers, which extends its scope and allows the OS to be used in a variety of devices and scenarios requiring high-performance multi-agent control.

Planned functionality. In the future, it is planned to develop an application programming interface (API) that will allow searching for the average value of different values residing on different agents in the system. This functionality could be extremely useful in several ways. Firstly, it will allow time synchronisation across different nodes, which in turn will ensure consistency of process execution between different agents. This is especially important for tasks that require precise coordination, such as distributed sensor networks or collaborative robotic operations.

Secondly, this API can be used for distributed computation of neural network weights in a multi-agent system consisting of inexpensive microcontrollers. In such systems, it is often necessary to average the weights received from different agents to improve the quality of model training and increase the overall performance of the neural network.

To implement the search for the mean value within a multi-agent system, we propose to use the local voting algorithm [1]. This algorithm allows each agent to exchange information with its neighbours and make decisions based on the received data, which contributes to a more efficient and faster consensus on the mean value. This approach not only reduces the load on the network, but also

increases the resilience of the system to failures of individual agents, which makes it particularly suitable for use in resource-constrained environments.

Conclusion. To conclude the paper, the current development of a real-time multi-agent operating system for collaborative robot control shows significant progress in the areas of task, memory and network management. The implementation of a task manager and timer handling functionality already lays the foundation for an efficient system. Future plans include the implementation of an API to search for averages across different agents using a local voting protocol, which will improve the coordination and synchronisation of robot actions. These steps are aimed at creating a more robust and efficient multi-agent system capable of solving complex problems in real time.

REFERENCES

1. **Amelina N. et al.** Approximate consensus in stochastic networks with application to load balancing //IEEE Transactions on Information Theory. – 2015. – T. 61. – №. 4. – C. 1739-1752.

A. V. BRAGIN
(Lomonosov Moscow State University, Moscow)

GYROSCOPE BIASES ESTIMATION USING ZERO-VELOCITY UPDATES IN PEDESTRIAN NAVIGATION

Pedestrian navigation system based on foot-mounted inertial measurement units is considered. The problem of gyroscope biases estimation with the help of zero-velocity updates in case of simplified motion equations usage is studied. Analytical observability analysis done with several assumptions shows that gyroscope biases are observable. However numerical analysis done for simulated data indicates that "vertical" gyroscope bias estimates convergence is slow which is unacceptable for practical applications. Further studies should uncover the reason for such behavior of formally observable variables.

Introduction. Autonomous pedestrian navigation is on a high demand in different cases: military personnel in a GNSS-denied area, emergency units or firefighters in a large buildings, etc. In the paper pedestrian navigation system based on foot-mounted micromechanical inertial sensors is considered. Foot-mounted configuration allows to use information about foot zero velocity in the stance phase of the step. Zero velocity updates (ZUPT's) make navigation with low-cost and low-accurate micromechanical inertial sensors possible, but cannot prevent the growth of heading error. Heading error is a result of gyroscopes biases which should be estimated and compensated.

A common approach in inertial navigation is to estimate sensors biases during navigation with the help of different external information such as GNSS. In pedestrian navigation the main correction method is ZUPT, but in the literature there is no consensus on the possibility of gyroscopes biases estimation via ZUPT. In [1] authors state that modeling errors in the system affects the navigation accuracy harder than the biases and thus their estimation is not recommended. In [2] analysis of multiple algorithms tests on real data shows that gyros biases estimation shows positive effect in some cases. In [3] authors state that biases are "weakly observable", based on simulated data analysis.

It is shown in the paper that gyroscopes biases are observable during ZUPT in case of simplified motion equations usage. Using simulated data it is shown that despite the observability estimates of "vertical" gyro bias doesn't converge to true values in a reasonable time.

Gyroscopes biases estimation. Here are the motion equations and corresponding error equations:

$$\begin{aligned}
 \dot{p}'_n &= v'_n & \dot{\delta p}_n &= \delta v_n + \hat{p}'_n C'^T_{sn} (\Delta v_s^0 + v_s^s) & f'_s &= f_s + \Delta f_s \\
 \dot{v}'_n &= C'^T_{sn} f'_s + g_n, & \dot{\delta v}_n &= \hat{g}_n \beta_n + \Delta f_n + \hat{v}'_n C'^T_{sn} (\Delta v_s^0 + v_s^s), & \omega'_s &= \omega_s - v_s \\
 \dot{C}'_{sn} &= (\hat{\omega}'_s + \hat{v}'_s^0) C'_{sn} & \dot{\beta}_n &= C'^T_{sn} (\Delta v_s^0 + v_s^s) & v_s &= v_s^0 + \Delta v_s + v_s^s \\
 \dot{v}_s^0 &= 0 & \dot{\Delta v}_s^0 &= 0
 \end{aligned} \tag{1}$$

Here p'_n, v'_n denote coordinates and velocities in navigation frame, C'_{sn} denotes orientation matrix describing transition from navigation frame to sensor frame, $\delta p_n, \delta v_n$ denotes the so-called dynamic coordinates and velocity errors [4], β_n denotes orientation error. f'_s, ω'_s denotes accelerometers and gyroscopes measurements respectively, $\Delta f_s, v_s$ – measurements errors, v_s^0, v_s^s stands for constant and stochastic components of gyroscope biases and Δv_s^0 stands for bias estimation error. Navigation errors are written for flat Earth model [5], these simplified model is widely used in pedestrian navigation.

Scientific supervisor associate professor, professor of the applied mechanics and control chair of the mathematics and mechanics department Lomonosov Moscow state university, Bolotin Y.V.

System (1) is aided with zero velocity. Measurements are formed when the stance phase is detected. SHOE detector was used for this purpose [6].

$$\begin{aligned} Z' &= v'_n & z &= Z' - Z = \delta v_n + r_n = Hx + r_n, & x &= \begin{pmatrix} \delta p_n^T & \delta v_n^T & \beta_n^T & \Delta v_s^{0T} \end{pmatrix}^T \\ Z &= v_n - r_n, & H &= [0_3 & I_3 & 0_3 & 0_3] \end{aligned} \quad (2)$$

Here Z, Z' denotes measurements in terms of state vector and z denotes measurements in terms of error vector, r_n denotes measurement errors, H denotes measurement matrix, corresponding to the EKF state vector x . Conventional EKF is used.

Observability analysis. Observability analysis was done with a few simplifications. First, stance phase of the step is instantaneous. Second, all steps of the pedestrian are exactly the same. Observability matrix is given for the state vector $x = (\delta v_n^T \ \beta_n^T \ \Delta v_s^{0T})^T$, since position error is obviously unobservable:

$$\mathcal{O}_k = \begin{bmatrix} HF^k \\ \dots \\ HF \\ H \end{bmatrix} = \begin{bmatrix} I_3 & k\hat{g}_n^T & k(\hat{g}_n C_2 + C_3) + \frac{k(k-1)}{2} \hat{g}_n^T C_1 \\ I_3 & \hat{g}_n^T & \hat{g}_n C_2 + C_3 \\ I_3 & 0_3 & 0_3 \end{bmatrix} \quad \begin{aligned} C_1 &= \int_{\tau=t_k}^{t_{k+1}} C'_{ns}(\tau) d\tau \\ C_2 &= \int_{\tau=t_k}^{t_{k+1}} d\tau \int_{s=t_k}^{\tau} C'_{ns}(s) ds \\ C_3 &= \int_{\tau=t_k}^{t_{k+1}} \hat{v}'_n(\tau) C'_{ns}(\tau) d\tau \end{aligned} \quad (3)$$

It can be shown that the unobservable subspace corresponding to the matrix \mathcal{O}_k contains only the vector $v = (0_{1 \times 3} \ g_n^T \ 0_{1 \times 3})^T$, i.e. only β_3 is unobservable.

Gyroscopes biases estimability for the simulated data. Algorithm tests were performed with the help of the simulator, similar to the one, presented in [3]. Coordinates and orientation angles in the swing phase are modeled as harmonic functions. Velocity in the stance phase equals zero. Pitch and roll angles were in the stance phase were different in different experiments modeling different sensor position on the foot.

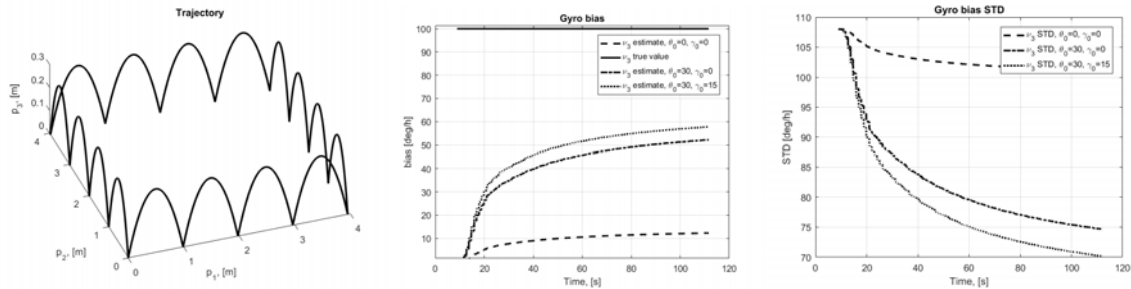


Fig.1. Left – example of the foot trajectory, center – “vertical” gyro bias estimation result for different sensor mounting positions (different pitch/roll angles in the stance phase), right – corresponding covariances.

Conclusions. It is shown that for simplified motion equations gyroscopes biases are observable, but the estimates don’t converge in a reasonable time. This conclusion is based on a modeling results. Real data differs from the simulated one in the sense that conditions for biases estimation become worse, so further research should be conducted to uncover the influence of the factors not modeled in the presented study.

REFERENCES

1. Nilsson J. O., Skog I., Handel P. A note on the limitations of ZUPTs and the implications on sensor error modeling //2012 International Conference on Indoor Positioning and Indoor Navigation (IPIN), 13-15th November 2012. – 2012.

2. **Wagner J. F., Kohl M., Gyorfı B.** Reevaluation of algorithmic basics for ZUPT-based pedestrian navigation //IEEE access. – 2022. – Vol. 10. – P. 118419-118437
3. **Zhu M., Wu Y., Luo S.** A pedestrian navigation system by low-cost dual foot-mounted IMUs and inter-foot ranging //2020 DGON Inertial Sensors and Systems (ISS). – IEEE, 2020. – P. 1-20.
4. **Bolotin Y., Bragin A., Gartseev I.** Covariance error analysis for pedestrian dead reckoning with foot mounted imu // CEUR Workshop Proceedings. — 2019. — Vol.2498. — P. 243–250
5. **Saab S. S., Gunnarsson K. T.** Automatic alignment and calibration of an inertial navigation system //Proceedings of 1994 IEEE Position, Location and Navigation Symposium-PLANS'94. – IEEE, 1994. – P. 845-852
6. **Skog I. et al.** Zero-velocity detection—An algorithm evaluation //IEEE transactions on biomedical engineering. – 2010. – Vol. 57. – №. 11. – P. 2657-2666

T.O. BERGER, I. A. LOMAKA

(Samara National Research University named after Academician S. P. Korolev, Samara)

PARAMETER SELECTION FOR MAGNETIC ATTITUDE CONTROL OF SMALL SATELLITES IN SUN-SYNCHRONOUS ORBIT

A methodology for selecting parameters of passive magnetic attitude control systems to ensure the required orientation of small spacecraft in sun-synchronous orbits is presented. This methodology is implemented in dedicated software that evaluates the angular velocity damping time, optimal placement and quantity of magnetic materials, and models the attitude dynamics of small spacecraft with a passive magnetic stabilization system.

Introduction. The rapid growth in the number of small satellites, especially those built to the CubeSat standard, over the past decade is driven by their numerous advantages, such as shorter development timelines, cost-effective manufacturing and launch options, and a wide range of potential uses. These characteristics have captured the attention of not only research and educational institutions but also private companies, with the latter now offering services such as Earth remote sensing and satellite-based communication using small satellites. As applications expand and mission requirements become more sophisticated, demands on satellite functionalities and subsystems are higher. This particularly affects attitude control systems, as the majority of scientific research with nanosatellites requires specific spatial orientation [1].

For missions where a pointing accuracy of 10–15 degrees is sufficient, passive control systems that exploit the natural interaction between the spacecraft and external environmental torques are often the optimal choice. Among those, passive magnetic attitude control systems (PMACS) are particularly popular for small satellite missions. By incorporating permanent magnets and hysteresis dampers on board, these systems generate torque through interaction with Earth's magnetic field, aligning the spacecraft with the geomagnetic field vector. With no moving parts, PMACS are highly compatible with the size, weight, and power constraints of small satellites, providing a reliable and simple implementation [2].

Despite its numerous advantages, the complexity of magnetic forces and their behavior in space conditions result in comprehensive modeling of spacecraft angular motion essential yet challenging. Although the literature provides several cases of successful PMACS implementations, it offers limited insight into the criteria guiding key decisions, such as the sizing, positioning, and selection of magnetic materials. Understanding how these parameters influence spacecraft attitude dynamics is crucial; however, the lack of comprehensive methodologies limits the ability to design these systems optimally.

This work presents a methodology developed at the Department of Space Research at Samara University for selecting parameters of magnetic control systems that ensure the required orientation within the desirable deviation range. The methodology is applied to sun-synchronous orbits, where the near-polar trajectory introduces both control challenges and leverageable characteristics. The methodology is then implemented through dedicated software designed to model the attitude dynamics and estimate the angular velocity damping of small spacecraft equipped with magnetic materials in different configurations.

Passive magnetic attitude control systems. In PMACS, two types of magnetic materials are used: permanent magnets and hysteresis dampers. Permanent magnets generate a torque that aligns their axes with Earth's magnetic field lines, thus providing a restoring force. However, due to changes in the magnetic field direction during orbital motion, oscillations can arise. To dampen these oscillations, the hysteresis rods are installed in the spacecraft. These changes are particularly pronounced in polar and near-polar orbits, where the satellite passes over nearly all latitudes, from the North to the South Pole, exposing it to a broad range of magnetic field intensities and directions. This

results in more dynamic magnetic conditions compared to equatorial or mid-latitude orbits, where field variations are less extreme.

Sun-synchronous orbits, a specific type of near-polar orbit, are designed to pass over the same region of Earth at approximately the same local solar time each day. This timing consistency provides stable and predictable conditions for Earth observation, scientific research, and other tasks that require regular and uniform lighting conditions. Furthermore, the near-polar nature of these orbits enhances the interaction between magnetic materials and Earth's magnetic field, contributing to the effectiveness of PMACS compared to orbits with lower inclinations.

The dipole moments of permanent magnets must be selected so that their restorative action effectively counteracts external torques [3]. This is especially crucial for small satellites, whose low inertial properties make them highly susceptible to gravitational gradient effects and external forces. Additionally, at low Earth orbits, atmospheric drag must be considered, as the ballistic coefficient of nanosatellites is significantly higher than that of larger satellites with comparable volumetric density [4].

The developed methodology takes into account the dynamics of both near-polar orbits and small satellites. In the initial stage, the parameters of PMACS are determined, including the characteristics of the permanent magnet, the required attitude accuracy, and the material of the hysteresis rod. An analysis of the hysteresis loop is performed to compare the properties of various materials, after which the minimum magnetic moment is calculated, and resonance conditions are checked. The optimal placement and quantity of magnetic materials along each axis are then assessed. The methodology is implemented in specialized software that includes an internal library of key hysteresis materials commonly used in small satellite missions, while also allowing for customizable parameters where available.

The complex nature of hysteresis functions, combined with the interaction of onboard magnetic materials with Earth's magnetic field in a sun-synchronous orbit, underscores the need for an accurate methodology for effectively modeling angular motion. Improper placement of these materials can lead to ineffective attitude control, potentially jeopardizing mission success. The developed methodology provides a theoretical foundation for understanding the motion of small satellites under external forces, with onboard magnetic materials to ensure attitude control and stabilization. The specialized software serves as a tool for evaluating effectiveness and selecting optimal system parameters, thus ensuring precise attitude control necessary for mission objectives.

REFERENCES

1. **Belokonov I.V., Timbai I.A., Barinova E.V.** Selection of design parameters for CubeSat-format nanosatellites with passive stabilization systems. // *Gyroscopy and Navigation*. 2020. Vol. 28. No. 1 (108). pp. 1–7.
2. **Ovchinnikov M.Yu., Roldugin D.S.** A survey on active magnetic attitude control algorithms for small satellites // *Progress in Aerospace Sciences*. 2019. V. 109. Article 100546.
3. **M. Ovchinnikov, V. Pen'kov, O. Norberg, S. Barabash,** Attitude control system for the first Swedish nanosatellite "MUNIN", *Acta Astronautica* 46 (2000).
4. **Belokonov I.V., Timbai I.A.** Motion of a nanosatellite relative to its center of mass in near-Earth orbits: Study Guide. Samara: Samara University Press, 2020. 128 p.

D.G. ARSENIYEV, A.E.MISNIK, M.A.SHALUKHOVA
(Peter the Great St. Petersburg Polytechnic University, St. Petersburg,
Inter-state Educational Institution of Higher Education "Belarusian-Russian University", Mogilev)

MANAGEMENT OF PATIENT REHABILITATION IN MEDICAL CYBERPHYSICAL SYSTEMS

The method of patient rehabilitation management in medical cyberphysical systems based on the use of artificial intelligence is considered. To create a digital model of the musculoskeletal system, computer vision technologies and trajectory analysis of the obtained points are used. By individualising recommendations, the method contributes to improving the effectiveness of patient treatment.

Introduction. Medical cyberphysical systems represent a distinct category of cyberphysical systems that integrate physical components and computing technologies with the objective of enhancing the quality of medical care. The effective management of processes in modern medical cyberphysical systems, including patient rehabilitation, necessitates the integration of advanced technologies and methods, as well as an individualised approach to each patient. Among the key challenges associated with the creation and implementation of classical control systems are the complexity of integration into existing workflows, the necessity for subsequent technical support and knowledge updates, and the limited applicability of systems based on statistical data processing [1-3].

The objective of this paper is to present a method for controlling the process of patient rehabilitation in medical cyber-physical systems. The method involves creating a digital model of the musculoskeletal system, which will facilitate more accurate predictions regarding the course of rehabilitation. The proposed approach enhances the availability and efficiency of treatment while reducing the burden on medical personnel.

The management of the rehabilitation process in medical cyberphysical systems. In collaboration with the Federal State Budgetary Institution 'Federal Centre for Traumatology, Orthopaedics and Endoprosthesis' of the Ministry of Health of the Russian Federation (Smolensk), which specialises in the provision of high-tech medical care to patients with diseases of the musculoskeletal system, a cyberphysical system for the rehabilitation of patients after joint endoprosthesis has been developed. The ontological approach to system development was implemented using the ontological engineering module of the software and tool environment, which is based on a meta-associative graph including process components in the form of methods and events. The developed system assumes the use of mobile devices equipped with a camera (tablet or mobile phone) to obtain video footage and their interaction with the server module of the system responsible for analysing the obtained data.

The proposed approach to rehabilitation management is based on the use of technical and software tools for the creation and subsequent analysis of a digital model of the human musculoskeletal system. The application of complex assessment, combining qualitative and quantitative methods, allows to comprehensively study the process of changing the state of the musculoskeletal system and to ensure the correct functioning of the developed system. The applied method of functional diagnostics includes the consideration of kinematic parameters, which allow us to determine the characteristics and form of movements, to track and record data on the compliance of the position of the body's support points during the performance of restorative exercises [3-7].

Obtaining the coordinates of the initial points of the joint position in space is carried out with the help of frame-by-frame analysis of the video sequence of the test movement: to determine the angle, the method of functional diagnostics allocates reference points, then, depending on the tested node, the connection vectors are determined. As a result, the obtained measurement information can be considered as the position of the reference points of the human body, the angles of bending of its joints, obtained after processing the video sequence. Each extracted frame is passed through a pre-trained EfficientNet convolutional neural network that extracts features for each frame, which are

Academic advisor Professor, Vice-Rector for International Activities, Chief Scientific Officer of the Laboratory 'Intelligent Control Systems' Arseniev, Dmitry, Germanovich.

numerical representations of important aspects of the image characterising physical features of objects. The features are aggregated across all frames to form a digital model of the patient's musculoskeletal system, which is stored in the database of the intelligent decision support system.

The data obtained on the patient's musculoskeletal condition are combined with the patient's profile information for further processing and identification. This is achieved by employing a recurrent LSTM model, which is used to discern patterns between physical features, compliance with recommendations and the effectiveness of individual rehabilitation plans. The clustering of data based on the functional state of the musculoskeletal system enables a more accurate prediction of recovery for patients with similar features. Based on the clusters obtained, a rehabilitation plan is formulated and updated in accordance with the individualised recovery trajectory [8].

In order to evaluate the extent to which the individual rehabilitation plan derived from numerical modelling correlates with the actual outcomes, we examined two groups of patients. The first group (n=46) underwent endoscopic knee joint endoprosthesis and completed their rehabilitation using the prototype of the decision support system. The second group (n=34) did not utilise the decision support system during their rehabilitation. The developed system demonstrated a high degree of predictive capability, with 89.1% of cases (64.1% in the group rehabilitated in accordance with general recommendations) aligning with or exceeding the trajectory constructed by the system and the actual course of rehabilitation. In order to provide an objective evaluation, data on the progress of rehabilitation is still being collected. However, at this stage, rehabilitation therapists have already noted a positive effect of the prototype decision support system due to increased awareness of the functional state of the musculoskeletal system and direct involvement of the patient in the rehabilitation process.

The ability of systems developed based on artificial intelligence to manage and control recommendations in quasi-real time, adapting and modifying them according to the current state of the patient is an important advantage, allowing the creation of a personalised recovery trajectory and an effective plan for further treatment.

Conclusion. The results obtained confirm the significant potential for application of the developed system in clinical practice. As the data accumulates, the system will continue to be improved, providing more accurate and effective interventions in process management, which will open new opportunities for further development and integration of additional functionalities. Further development and adaptation of the system will not only improve the quality of the rehabilitation process, but also significantly reduce the economic costs associated with the long-term treatment and rehabilitation of patients. Further work is being carried out in several directions: extending the system's functionality by integrating new virtual and augmented reality modules to create a visual image of the patient's digital model, and improving machine learning algorithms to analyse large amounts of data and improve the accuracy of the resulting predictions of the most effective rehabilitation strategy and duration.

This work was supported by the Ministry of Education and Science of the Russian Federation (project № FSWF-2023-0012)

REFERENCES

1. **Burdukovsky, V. N., Chudesova G. P.**, Actual issues of the use of medical cyberphysical systems / V. N. Burdukovsky, G. P. Chudesova // Strategies and tools of economic management: sectoral and regional aspect : Proceedings of the IX International Scientific and Practical Conference, St. Petersburg, 15 May 2020 / Under the general editorship of V. L. Vasilyonok. - St. Petersburg: Saint-Petersburg National Research University of Information Technologies, Mechanics and Optics, LTD " Scientific and Production Association of Fire Safety Automated Systems ", 2021. – P. 5-9. – EDN QDCDLB.
2. **Levonevskiy D., Motienko A.**, "Using Mobile Applications for Patient Monitoring in Smart Medical Wards," 2024 International Russian Automation Conference (RusAutoCon), Sochi, Russian Federation, 2024, pp. 833-837, doi: 10.1109/RusAutoCon61949.2024.10694098.
3. **He, S., Meng, D., Wei, M.**, [et al.] Proposal and validation of a new approach in tele-rehabilitation with 3D human posture estimation: a randomized controlled trial in older individuals with sarcopenia. BMC Geriatr 24, 586 (2024). <https://doi.org/10.1186/s12877-024-05188-7>
4. **Misnik A.E.** Metagraphs for ontological engineering of complex systems. Prikladnaya informatika= Journal of Applied Informatics, 2022, vol.17, no.2, pp.120-132 (in Russian). DOI: 10.37791/2687-0649-2022-17-2120-132.

5. **Kustova O.V., Khoziainova S.S., Abuseva G.R., Makhotkina N.N., Ponomarenko G.N.**, Reabilitatsionnye tekhnologii u patsientov posle total'nogo endoprotezirovaniya krupnykh sustavov nizhnikh konechnostei: naukometricheskiy analiz [Rehabilitative technologies in patients after total endoprosthesis of lower limbs' major joints: scientometric analysis]. *Vopr Kurortol Fizioter Lech Fiz Kult.* 2024;101(1):54-61. Russian. doi: 10.17116/kurort202410101154. PMID: **38372738**.
6. **Namazov, A. K., Namazov, K. A.**, Physical rehabilitation as the most important component in the system of medical rehabilitation / A. K. Namazov, K. A. Namazov // Health is the foundation of human potential: problems and ways to solve them. – 2019. – vol. 14, № 2. – P. 903-907. – EDN CEHQUH.
7. **Wang, J., Qiu, K., Peng, H., Fu, J., & Zhu, J.** (2019). AI coach: Deep human pose estimation and analysis for personalized athletic training assistance. In Proceedings of the 27th ACM international conference on multimedia, P. 374-382. <https://doi.org/10.1145/3343031.3350910>
8. **Arseniev D. G., Borisov V. V., Misnik A. E., Gomzhina E. A., Shalukhova M. A.**, "Intelligent Synthesis of Individual Rehabilitation Plans for Patients after Joint Endoprosthesis Based on Computer Vision Technologies," 2024 7th International Conference on Information Technologies in Engineering Education (Inforino), Moscow, Russian Federation, 2024, pp. 1-5, doi: 10.1109/Inforino60363.2024.10552027.

A.A. GOLOVAN, V.S. VYAZMIN
(Lomonosov Moscow State University, Moscow)

THE CURRENT STATE OF STRAPDOWN AIRBORNE GRAVIMETRY. METHODOLOGY OF GRAVIMETER DATA POSTPROCESSING

Airborne gravimetry is a branch of geophysics that studies the methods of measuring Earth's gravity on board an aircraft. The paper discusses the current state of airborne gravimetry and the methodology of data postprocessing in the case of using a strapdown gravity meter based on a strapdown inertial navigation system and GNSS receivers.

Introduction. Airborne gravimetry is a method of airborne geophysics that deals with determining the vertical component of the gravity disturbance vector (gravity disturbance) from airborne gravimeter measurements on board an aircraft (a fixed-wing aircraft or helicopter). Inertial gravimeters based on a gyro-stabilized platform are traditionally used in airborne gravimetry, e.g., L&R, Chekan-AM, GT-2A and others instruments [1]. In the paper, we discuss the use of a strapdown airborne gravimeter, which is alternative to the traditional inertial gravimeters. A strapdown airborne gravimeter is based on a strapdown inertial navigation system (INS) (or an inertial measurement unit) and global navigation satellite system (GNSS) receivers [2-4]. The gravity disturbance determination from strapdown gravimeter measurements is carried out in the postprocessing mode and includes several stages. The paper describes the key stages of data postprocessing (the determination of GNSS solutions, INS initial alignment, and INS-GNSS integration) and the corresponding approaches (algorithms). A brief description of the developed methodology for raw data postprocessing is presented.

Methodology of strapdown gravimeter data postprocessing. We formulate the gravimeter data postprocessing problem as determining the gravity disturbance $\Delta g = g - g_0$ (where g and g_0 are the vertical components of the actual and normal gravity vectors, respectively) on the aircraft flight path from the raw measurements of the gravimeter's INS inertial sensors (accelerometers and gyroscopes) and GNSS onboard and ground-based receivers. The developed data postprocessing methodology includes the following stages:

1. Raw data quality control (checking for possible data loss and instruments failures, analyzing the temperature variations inside the gravimeter, etc.).
2. The initial alignment of the gravimeter's INS and calibration of the INS accelerometers (determining the in-run biases and scale factor errors).
3. Determining the GNSS antenna position and velocity from the raw GNSS measurements (using the carrier-phase differential mode).
4. The INS-GNSS integration.
5. Determining the gravimetric solution (gravity disturbance estimation on the flight path).

Now we briefly describe the key aspects of the developed data postprocessing methodology. At the INS initial alignment (stage 2), the attitude angles of gravimeter's INS at the aircraft standstill are determined and the INS accelerometers are calibrated (the accelerometer biases and scale factor errors are estimated) [2]. The difficulty of the problem is the uncontrolled angular motion of the gravimeter due to the wind at the aerodrome, turning on and off the aircraft engines, the work of the crew, etc.

At the INS-GNSS integration (stage 4), the parameters of the aircraft flight path and the INS inertial sensor instrumental errors are estimated. The mathematical formulation of the problem is based on the INS error propagation equations and observation equations derived for a GNSS aided INS (with the GNSS positions and velocities used as the observations) [1, 5]. The state vector of the constructed spate-space model includes the following parameters:

- the latitude, longitude and height of the accelerometers proof mass above the reference ellipsoid;
- the INS dynamic velocity errors (the east and north components);
- the INS attitude errors (the misalignments of the vertical and azimuthal error);
- the accelerometers and gyroscopes in-run biases;

- the GNSS antenna offsets with respect to the INS (lever arm);
- the time-synchronization errors.

It is well known that the INS-GNSS integration problem given the measurement error stochastic models is reduced to the standard linear optimal estimation problem. The solution to the problem is provided by Kalman filtering and smoothing [6].

The formulation of the gravimetric problem (stage 5) is based on the fundamental equation of airborne gravimetry [1], which is the equation of the INS accelerometers proof mass motion. We use the form of the equation in the projection onto the geodetic frame (East, North, Up). However, other forms can also be used [1]. After replacing the unknown terms in the equation by the inertial sensor measurements and GNSS data, the gravimetric problem can be reduced to a standard linear optimal estimation. The state vector includes the following unknown parameters: the gravity disturbance, residual angular errors (misalignments of the vertical), vertical accelerometer scale factor error, lever-arm errors, and time-synchronization errors. The estimates of the parameters are provided by the Kalman filter and optimal smoother.

Numerical example of gravimeter data postprocessing. In Fig. 1, the numerical results from the airborne gravimeter data postprocessing using the developed methodology are presented. The survey flight was carried out in 2021 with the use of a strapdown gravimeter and the traditional gravimeter based on a stabilized platform (GT-2A) [1]. A fixed-wing aircraft was used in this survey flight. In Fig. 1 (on the left), the position errors of the strapdown gravimeter's INS dead-reckoning (the autonomous mode) are presented. The GNSS positions were used as a reference solution. The maximum error of the gravimeter's INS position solution is 3 km, which is the accuracy level of the gravimeter's sensors after the calibration.

In Fig. 1 (on the right), the gravity disturbance estimates based on the raw data from the strapdown and traditional airborne gravimeters are presented. The standard deviation of the difference between two gravity disturbance estimates is 1.1 mGal, which shows a good agreement of the results. Also shown are the gravity data derived from an Earth's global gravity field model of high degree and order (XGM2019) [7]. Fig. 1 shows that the global gravity data have much lower spatial resolution comparing to the airborne gravimetry gravity data.

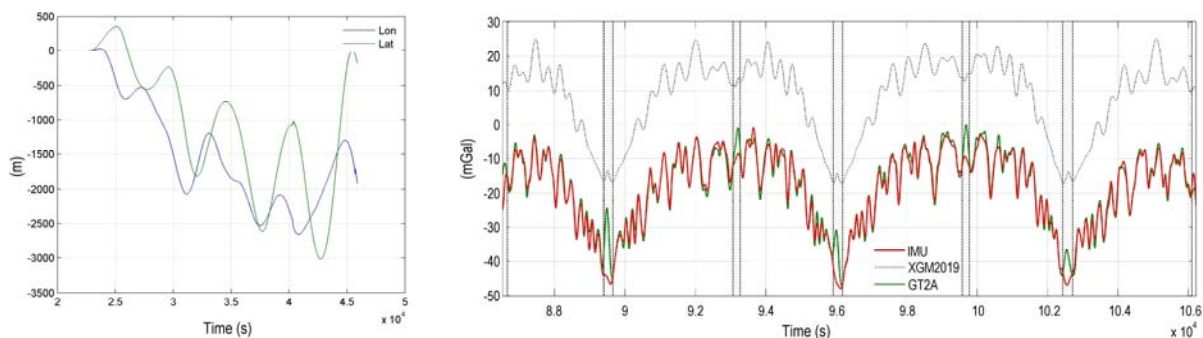


Fig. 1. On the left: the strapdown gravimeter's INS dead-reckoning errors, km. On the right: the gravity disturbance estimates from the strapdown airborne gravimeter data (red) and stabilized-platform gravimeter data (green); the global gravity field model data (black), mGal.

Conclusions. The current trend in airborne gravimetry is to use strapdown gravity meters rather than traditional ones, which are based on stabilized platforms. In the paper, the key aspects of postprocessing raw data from a strapdown gravimeter are briefly described. The numerical example from a survey flight with a state-of-the-art strapdown gravimeter are also presented. The results of the data postprocessing (the gravity disturbance estimates) are in good agreement with the results from a classical airborne gravimeter.

REFERENCES

1. **Methods and technologies** for measuring the earth's gravity field parameters. Cham, Switzerland, Springer. 2022. 388 p.
2. **Golovan A.A., Vyazmin V.S.** Methodology of Airborne Gravimetry Surveying and Strapdown Gravimeter Data Processing, Gyroscopy and Navigation, 2023, vol. 14, no. 1, pp. 36-47.

3. **Cai S., Zhang K., Wu M., Huang Y.** The method on acceleration extraction from strapdown airborne scalar gravimeter based on flight dynamics. *Adv. Mater. Res.* 2012. P. 2152–2156.
4. **Senobari M.S.** New results in airborne vector gravimetry using strapdown INS/DGPS. *J. Geod.* 2010. V. 84: P. 277–291.
5. **Jekeli C.** Inertial navigation systems with geodetic applications. Walter de Gruyter, New York. 2001.
6. **Kailath T., Sayed A.H., Hassibi B.** Linear Estimation. Prentice Hall, Upper Saddle River, NJ, USA, 2000. 854p.
7. **Zingerle P., Pail R., Gruber T., Oikonomidou X.** The combined global gravity field model XGM2019e. *J Geod.* 2020. V. 94. P. 1-12

F.S. KAPRALOV
(Lomonosov Moscow State University, Moscow)

MODERN PRECISION OF ATTITUDE DETERMINATION USING MULTI-ANTENNA SATELLITE NAVIGATION SYSTEM

The report focuses on the analysis of the precision of attitude determination by range satellite measurements from a multi-antenna navigation system. Results are presented from the processing of a real experiment with five satellite antennas within one meter of each other. A reference orientation is obtained with a precision multiple times higher than the current typical precision of attitude determination using a multi-antenna satellite system. This allows for a comprehensive examination of attitude angle errors.

Introduction. The problem of attitude determination with sub-tenths of a degree accuracy occurs frequently in many applications. It is well-known that the problem can be solved with the accuracy by a high-grade strapdown inertial navigation system (INS). The main drawbacks that make the use of INS in some applications unreasonable are its typical mass, size, power supply, and price. To overcome these strapdown INS limitations, multi-antenna Global Navigation Satellite Systems (GNSS) with more than two antennas can be used to determine attitude angles to within 0.1° . The modern accuracy of attitude determination using dual- or triple-antenna systems is about the first tenth of a degree, adjusted to a 1-meter baseline length [1]. A baseline is defined as a vector between the phase centers of GNSS antennas.

The most common approach to solving the problem is as follows. For each baseline, the coordinates of which are known a priori in the body reference frame, the estimate of the baseline coordinates in the navigation, e.g., geodetic, reference frame must be obtained. So, for each baseline we have a linear mixed integer least squares problem. The problem arises from the integer ambiguity of the phase measurement difference and, as a rule of thumb, is solved numerically using LAMBDA [2]. We use its numerical modification, so called MLAMBDA [3]. After resolving the integer ambiguity and estimating the baseline coordinates in the navigation and body reference frames, it is possible to determine the attitude of the body reference frame relative to the navigation frame by solving the optimization problem for the corresponding attitude matrix [4].

Real experiment. In August 2023, a multi-antenna GNSS experiment was performed in Moscow under relatively favorable urban conditions. GNSS antennas were mounted on a wooden board, which is the body of the navigation system carrier object. The board is positioned approximately horizontally. During the record of the satellite measurements, 7 static positions were realized using three 90° rotations around the vertical in a clockwise direction and then three similar rotations in the opposite direction. The duration of each static position is 20 minutes, and the total duration of the experiment is approximately 2.5 hours. The main features of the experiment are as follows:

- multiple antennas: 2 Antcom 743GNSSA-XT-1 GNSS antennas are connected to the NovAtel PwrPak7D GNSS receiver, 1 NovAtel GNSS-804 GNSS antenna is connected to the NovAtel PwrPak7 GNSS receiver, 2 Javad AirAnt GNSS antennas are connected to the 2 Javad Prego GNSS receivers;
- multiple GNSS: all GNSS receivers process GPS and GLONASS signals, and NovAtel receivers also process Galileo and Beidou signals;
- short baselines: the maximum distance between any two GNSS antennas is less than 1 meter.

Attitude angles reference. The main objective of the experiment is to estimate the accuracy of attitude determination using multi-antenna GNSS. The experiment is designed to provide reference attitude angles with an accuracy several times better than the typical accuracy of the multi-antenna

GNSS solution. In this work, the attitude of the carrier object relative to a geodetic reference frame is described by the three angles of roll, pitch, and yaw (heading).

Reference yaw angle. The carrier object was in the initial position after the end of the main experiment. One of the five antennas was then repositioned so that the long baseline (more than 4 meters) could be formed with all the other antennas on the wooden board. Satellite measurements were recorded separately for the five antennas in this static configuration. The antenna positions relative to the body reference frame were measured, and an estimate of its accuracy was obtained. Exploiting the fact that the yaw angle error is inversely proportional to the baseline length, a reference yaw estimate can be obtained for the short baselines in the main experiment.

Reference pitch and roll angles. To estimate the reference roll and pitch angles in all static positions of the experiment, accelerometer measurements from a pre-calibrated microelectromechanical INS were used. The INS was mounted on top of the wooden board together with GNSS antennas. We reduce the problem of estimating pitch and roll angles to a least squares problem. In the measurement model, we consider a variability of the object body's rotational axis, and angular misalignments of the INS instrumental axes relative to the carrier body reference frame. An upper bound on the accuracy of the roll and pitch angles for each baseline is also estimated.

Attitude angles analysis. The results of analyzing the attitude angle errors in the experiment for different baselines are presented. The attitude errors of the baselines are decomposed into two components: low-frequency systematic and high-frequency stochastic. For each component, its partial influence on the total attitude error is analyzed.

REFERENCES

1. **Raskaliyev, A., Patel, S.H., Sobh, T.M., Ibrayev, A.** GNSS-based attitude determination techniques—a comprehensive literature survey. *IEEE Access*, 8, 2020, pp. 24873-24886. DOI: 10.1109/ACCESS.2020.2970083.
2. **Teunissen P.J.** Least-squares estimation of the integer GPS ambiguities. *Invited lecture, section IV theory and methodology, IAG general meeting, Beijing, China*, 1993, pp. 1-16.
3. **Chang, X.W., Yang, X., Zhou, T.** MLAMBDA: A modified LAMBDA method for integer least-squares estimation. *Journal of geodesy*, 79, 2005, pp. 552-565. DOI: 10.1007/s00190-005-0004-x.
4. **Wahba G.** A least squares estimate of satellite attitude. *SIAM review*, 7(3), 1965, pp. 409-409. DOI: 10.1137/1007077.

I. A. AKIMOV¹

(Lomonosov Moscow State University, Moscow, Russia)

AN APPROACH TO ESTIMATING THE GRAVITY VECTOR DISTURBANCE BASED ON REPEATED AIRBORNE OBSERVATIONS

An approach to estimating the gravity vector disturbance from airborne observations at repeated lines is presented. The use of a strapdown gravimeter is assumed. The approach is based on the error equations of gravimeter's inertial measurement unit and GNSS. A model of the gravity vector is constructed using the cubic splines. The unknown coefficients are estimated by the Kalman filter. The numerical results from simulated data processing are presented.

Introduction. This paper is devoted to the airborne vector gravimetry problem with using a strapdown airborne gravimeter that includes an Inertial Measurement Unit (IMU) and Global Navigation Satellite System (GNSS) receivers. Usually, only the vertical component of the gravity disturbance vector (GDV) is determined [1, 2]. The determination of the horizontal components of the gravity disturbance vector is more complicated because they are observed in a combination with the IMU systematic errors [3]. Some approaches use an a priori information about the GDV, while the others use additional measurements [3-5]. Our approach proposed in this paper uses both.

Several methods based on an a priori model of the GDV as a time-dependent function were proposed previously [1, 3], but the achieved accuracy of the GDV estimates is not sufficient to use them in practice. We propose a new approach that assumes repeated flight lines and uses a new a priori model of the GDV horizontal components: they are assumed to depend on the distance along the flight lines. Mathematically, the model of the GDV components is introduced as a linear combination of the cubic B-splines at a line and the problem of airborne gravimetry is reduced to the IMU-GNSS integration and Kalman filtering. We show that the new approach allows to increase an accuracy of the GDV estimation.

Problem statement and estimation algorithm. Let us introduce the geodetic frame as M_{E,N,U_p} , where M is the origin of the frame and coincides with in the IMU accelerometers proof mass. Then introduce the gravity disturbance vector $\Delta g = g - g_0$ as the difference between the actual gravity and normal gravity (e.g., computed using Helmert's formula) vectors in the geodetic frame. There are two parts of airborne vector gravimetry problem: estimation of the vertical component and estimation of the horizontal components. Solution to the first problem is well established, see, for example, [1, 2]. Our aim is to solve the second problem.

Estimation of the GDV at the repeated lines. The basics of the problem is the error equations of an IMU aided by GNSS [6]. The state vector of the error equations includes the following variables (the indices $_{E,N,U_p}$ mean the projections to the geodetic frame, indices $_{z1,2,3}$ mean the projections to the IMU body frame):

- $\Delta g_E, \Delta g_N$ are the east and north components of GDV;
- $\Delta f_{z1}, \Delta f_{z2}$ are the biases of the IMU accelerometers;
- v_{z1}, v_{z2}, v_{z3} are the drifts of the IMU gyroscopes;
- $\beta_1, \beta_2, \beta_3$ are the attitude errors;
- $\delta V_E, \delta V_N$ are the dynamic velocity errors.

The a priori GDV model is introduced as a linear combination of cubic B-splines [7]:

$$\Delta g_E(s(t)) = \sum c^E_i B_i(s(t)), \quad \Delta g_N(s(t)) = \sum c^N_i B_i(s(t)), \quad (1)$$

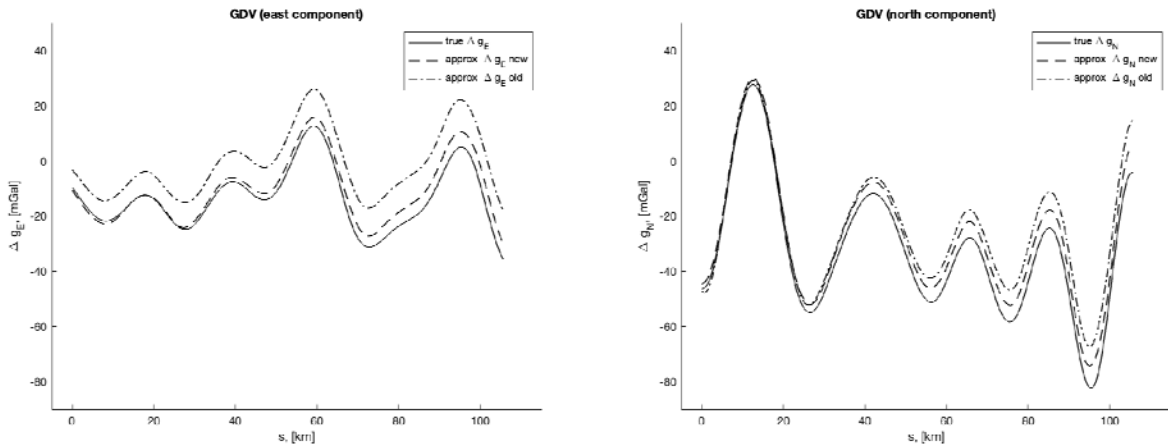
where $s=s(t)$ is the distance along the line, $B_i(s)$ is the B-spline, c^E_i, c^N_i are the unknown constants, $i=1, \dots, N$, i is the knot number, and N is the total number of knots at the flight line.

¹ The supervisor: Leading Researcher, Docent V.S.Vyazmin

Let us include $c_{i_i}^E, c_{i_i}^N$ in the state vector of IMU error equations and set the optimal stochastic estimation problem [8]. The estimate of the state vector (that consists of $2N+10$ components) is determined through Kalman filtering [8]. The GDV component estimates are computed using (1) from the estimates of $c_{i_i}^E, c_{i_i}^N$ obtained at the last iteration of the Kalman filter, $i=1, \dots, N$.

Data processing results. Below are the results of the algorithm testing based on the simulated data processing. The ideal IMU and GNSS data were simulated at two repeated lines. The systematic errors and noises were added to the ideal data according to the typical errors of a modern strapdown gravimeter and included the accelerometer biases and gyroscopes drifts. The values of the systematic errors are $\Delta f_{z1}=30$ mGal, $\Delta f_{z2}=-40$ mGal, $v_z=0.003$ deg/h.

The results of the GDV estimation are shown in Fig. 1. The reference gravity data is given by the global gravity model *EGM2008*. The standard deviation (STD) of the estimation error is 2 mGal, the mean value is 3-4 mGal. Note that a standard approach that uses the model of GDV as a time-dependent function shows much lower accuracy: the STD is 3-5 mGal and the mean value is 8-12 mGal. The results are shown in Fig. 1 and summarized in Table 1.



Pic. 1. The GDV estimates in the new approach (dashed), in the standard (time-dependent) approach (dashed with dots) and the reference data (solid) at a line. Left: the east component, right: the north component, mGal.

Table 1

The statistics from GDV estimation at two repeated lines

Statistics	New approach	Standard approach
Mean of Δg_E estimate error, mGal	2,74	12,24
Mean of Δg_N estimate error, mGal	4,72	7,82
STD of Δg_E estimate error, mGal	2,40	3,44
STD of Δg_N estimate error, mGal	1,78	5,19

Conclusions. The problem of the GDV estimation from strapdown airborne gravimeter measurements at repeated lines was solved. The a priori model of GDV was designed using the cubic B-splines parametrized by the distance along the line. The airborne vector gravimetry problem was reduced to optimal stochastic and Kalman filtering. The efficiency of the estimation algorithm was approved in simulated data processing, which showed good results even with two repeated lines (low STD and mean values were achieved).

REFERENCES

1. **Methods and technologies** for measuring the earth's gravity field parameters. Cham, Switzerland, Springer. 2022. 388 p.
2. **Golovan A.A., Vyazmin V.S.** Methodology of airborne gravimetry surveying and strapdown gravimeter data processing. Gyroscopy Navig. 2023. V. 14. P. 36–47.
3. **Kwon J.H., Jekeli C.** The effect of stochastic gravity models in airborne vector gravimetry. J. Geoph., 2002. P. 770–776.

4. **Cai W., Zhang K., Wu M.** Improving airborne strapdown vector gravimetry using stabilized horizontal components. *J. Appl. Geophys.*, 2013. V. 98. P. 79–89.
5. **Fang K., Cai T.** An algorithm for strapdown airborne gravity disturbance vector measurement based on high-precision navigation and EGM2008. *Sensors*. 2024. V. 24. P. 5899.
6. **Farrell J. A.** Aided navigation systems: GPS and high rate sensors. 2008. New York, NY, McGraw-Hill.
7. **Cheney E.W., Kincaid D.R.** Numerical Mathematics and Computing. Brooks/Cole Publishing Co., 2007. 784p.
8. **Kailath T., Sayed A.H., Hassibi B.** Linear Estimation. Prentice Hall, Upper Saddle River, NJ, USA, 2000. 854p.

P. S. MIKHAILOV, V. N. KONESHOV ¹, V. N. SOLOVYEV
(Schmidt Institute of Physics of the Earth of the RAS, Moscow)

ASSESSMENTS OF THE ACCURACY OF MODERN GLOBAL MODELS OF THE EARTH'S GRAVITY FIELD AND EXPERIENCE OF THEIR USE IN PERFORMING MARINE GRAVIMETRIC SURVEYS

Presents estimates of the accuracy of modern global models of the Earth's gravity field, obtained from comparisons with area surveys. As a result of estimates made at different latitudes and over different structures, patterns of error distribution in models and features of their change were revealed. Examples of practical application of models in marine surveys are considered.

Introduction. The global satellite model of the Earth's gravitational field contains data about anomalies in free air at the geoid level. The possibilities for practical use of models depend on such characteristics as resolution and accuracy of anomaly representation. Thanks to the satellite altimetry method, modern models have better detail and accuracy specifically in the World Ocean. The maximum resolution of a modern model based on altimetry data has now reached 1 arc minute. This resolution allows the creation of anomaly maps at a scale of up to 1:200000. At the same time, satellite data contain larger errors than instrumental measurements, therefore, using data from area marine surveys as more highly accurate, we can judge the reliability of global models. In addition, global satellite models of the Earth's gravity field are currently already finding effective application in the process of performing marine gravimetric surveys. Below are some examples of how the authors have used global models to clarification the systematic drift of a marine gravimeter and to perform a marine survey without initial and final still readings at ports calls. [1].

Estimates of Global Models. The most effective and simple way to estimate a model field is to compare the model data with high-precision direct area surveys, for example with marine surveys. At the Schmidt Institute of Physics of the Earth, global comparisons of modern global gravity models with high-precision marine surveys at different latitudes and over various geomorphological structures of the World Ocean were carried out. The objective of these studies was to determine the actual accuracy of the models, identify the main trends in their development and patterns in the distribution of errors.

The assessments showed that in the area of abyssal plains, all the studied models have close accuracy relative to marine gravity surveys. The error of the model data in terms of the standard deviation in such regions is estimated to be around 1 mGal. However, with the increase in the magnitude of the horizontal gradient of the change in the anomalous field, the error of the models increases significantly, as do the discrepancies in accuracy between the early and new models. For example, in the areas of mid-ocean ridges, the error of the EGM2008 model according to the standard deviation is estimated at 5 mGal, the Chinese SGG-UGM-2 model [2] at 4 mGal, and the latest Sandwell and Smith [3] and DTU [4] models are already at 2.5 – 2.7 mGal. It was also revealed that the errors of modern global models in almost all areas of the World Ocean depend to a greater extent on the magnitude of the full gradient of the anomalous field itself and do not depend on latitude [5].

Using estimates obtained in regions containing different values of the horizontal gradient of the anomalous field structure, it is possible to determine the general functional dependence of the error of the global model on the value of the horizontal gradient and, thus, obtain estimated information about the expected error of this model in any region of interest in the World Ocean.

Using global models in marine surveys. The increasing accuracy of global models allows them to be effectively used in the practice of performing marine gravimetric surveys. Using model data on the Earth's anomalous gravity field, such problems as clarification the systematic drift of a marine gravimeter and quality control of the devices operations can be solved.

¹ Scientific supervisor - professor, Head of scientific direction, Vyacheslav Nikolaevich Koneshov.

As a rule, a marine gravimeter has a continuous zero drift, individual for each device over a certain range. The drift velocity is usually determined during initial still readings and is refined during final still readings. Another well-known way to refine the drift rate of a gravimeter, if it is linear, is to evaluate the instrument readings at the intersection points of the survey lines. However, in modern practice, gravity surveys are often carried out together with seismic surveys, and modern seismic vessels can operate practically without port calling. Moreover, 3D seismic surveys often do not involve intersecting (tie) lines. In such a situation, the only way to determine the operating parameters of the gravimeter is to use model data on gravity field anomalies.

Since the global model does not contain systematic error components, comparison of gravimeter measurements with the model field allows us to identify systematic drift in the instrument readings. Moreover, with the increasing accuracy and detail of modern models, it becomes possible to determine not only the speed, but also the nature of the drift and take this into account when processing the survey. Figure 1 shows an example of the gravimeter performance evaluation at the testing site, after it was switched on from a "cold" state directly into the sea. The figure also shows the change in drift velocity caused by the transient process.

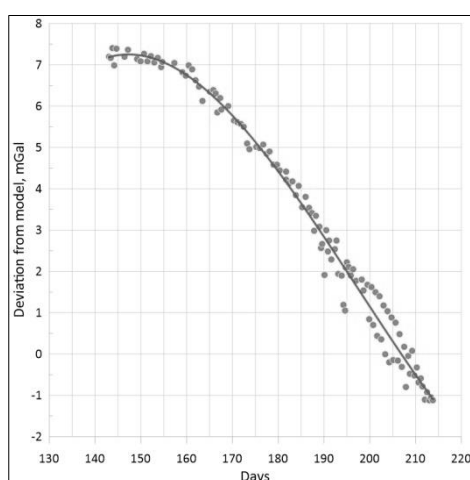


Fig. 1. Determination of the speed and nature of the gravimeter drift in the sea by comparing measurements on lines with data from the global model.

The second task in which the global model finds its applicability is quality control of the correct operation of devices. At the stage of quality control of marine measurements, it is necessary to promptly evaluate the gravimeter readings. If there are several gravimeters on board, this is done by comparing their readings, but differences in the readings of two gravimeters also lead to ambiguity. Using a model field allows us to identify deviations in the operation of one or several gravimeters on board and take measures to eliminate possible problems.

The third task is to reduce the survey to the level of a global model field. In the practice of modern marine gravimetry, reliable IGSN71 stations are not always available in all ports of departure of the vessel. And in the case of turning on the gravimeter directly at the sea, there is no tie to the absolute value of gravity in principle. The global model field is represented at sea at the geoid level, so it can be used to calculate the absolute level of the marine survey, which also allows for joint processing of surveys performed from

different coastal GSN71 stations or in their absence.

Conclusion. Actual estimates of modern gravity field models in open areas of the World Ocean are shown. In terms of accuracy and detail of anomaly representation, satellite models cannot yet replace instrumental marine and airborne gravimetric surveys. However, they can be used to plan surveys and during their production in order to improve the quality and reliability of the data obtained.

REFERENCES

1. **Peshekhonov V. G., Stepanov O. A. (eds.)**. Methods and Technologies for Measuring the Earth's Gravity Field Parameters. Springer Nature (Switzerland). 2022. P. 396. DOI: 10.1007/978-3-031-11158-7.
2. **Wei Liang, Jiancheng Li, Xinyu Xu, Shengjun Zhang, Yongqi Zhao** A High-Resolution Earth's Gravity Field Model SGG-UGM-2 from GOCE, GRACE, Satellite Altimetry, and EGM2008 // Research Geodesy and Survey Engineering. 2020. Vol. 6. Issue 8. Pp. 860 – 878. DOI: 10.1016/j.eng.2020.05.008
3. **Sandwell, D. T., Müller R. D., Smith W. H. F., Garcia E., Francis R.** New global marine gravity model from CryoSat-2 and Jason-1 reveals buried tectonic structure. Science. 2014. Vol. 346. No. 6205. pp. 65-67. DOI: 10.1126/science.1258213.
4. **Andersen O.B., Knudsen P.** The DTU17 global marine gravity field: First validation results, in International Association of Geodesy Symposia. Cham. Springer. 2020. pp. 83-87. DOI: 10.1007/1345_2019_65
5. **Mikhailov, P.S., Koneshov, V.N., Solovyev, V.N., Zheleznyak L. K.** New Results of Estimation of Modern Global Ultrahigh-Degree Models of the Earth's Gravity Field in the World Ocean. Gyroscopy Navig. 2022. 13, pp. 210–221 DOI: 10.1134/S2075108722040095

M.M. MURZABEKOV, D.S. BOBROV, V.P. LOPATIN, E.S. SKVORTSOV
(FSUE "VNIIFTRI", Mendeleevo settlement, Moscow region)

FIELD GEOPHYSICAL COMPLEX FOR CREATING NAVIGATION GRAVITY-MAGNETIC MAPS FOR AUTONOMOUS NAVIGATION SYSTEMS

The paper presents a field geophysical complex, including a plumb line deviation meter and a high-precision relative gravimeter for creating maps of the Earth's gravity field (EGF) parameters and an onboard quantum magnetometer and a magnetovariation station for creating maps of the Earth's magnetic field (EMF) parameters. These maps can become the basis for autonomous navigation systems by EMF and EGF. The maps measured using the proposed geophysical complex and directions for further research are presented.

Introduction. The components of integrated systems of autonomous navigation using the Earth's magnetic and gravitational fields (EMF and EGF) are the user navigation equipment (UNE) of the GNSS, the inertial navigation system (INS), the onboard measuring device and the reference navigation map of the parameters of these fields [1-6]. In such a navigation system, when external conditions do not affect the operation of the GNSS NAP, the "INS+NAP" integration mode is used. In cases where the NAP is not capable of solving the navigation problem, the correction of the deviation of the INS readings is carried out based on measurements of the parameters of the EMF and EGF. In this case, the reference map of the EMF and EGF is used to determine the current location based on the results of comparison with the measurement data of the onboard measuring device.

It should be noted separately, according to the works [7, 8], that the EGF maps are also needed as a source of corrective information for the INS. These works highlight that for promising INS, the error in determining the parameters of the GPS will make a significant contribution to the accuracy of the navigation solution.

The paper presents a field geophysical complex that allows creating maps of GPZ and MPZ parameters with previously unattainable accuracy and discreteness, which can be used in the creation and testing of integrated autonomous navigation systems.

The geophysical complex. The geophysical complex includes: 1) EGF parameter meters – deflection of the vertical [9] and high-precision relative gravimeter of the Scintrex CG-5 type (Fig. 1a); 2) EMF parameter meters – an onboard quantum magnetometer placed on a quadcopter and a magnetovariation station (Fig. 1b).



Fig. 1. Geophysical complex

Map creation results. EGF maps. Joint measurements of the acceleration of gravity g (AGG) and the components of the deflection of the vertical (DoV) ξ, η using a gravimeter and an astrometer were carried out on the territory of the Moscow region at a test site with linear dimensions of approximately 20x20 km. The polygon includes 32 points with an average distance of approximately 4 km from each other; the measurement time at each point does not exceed 1 hour.

Scientific supervisor – Doctor of Technical Sciences, professor, Honored Scientist of the Russian Federation, chief researcher FSUE "VNIIFTRI", Fateev Vyacheslav Filippovich.

To create DoV and AGG maps, a uniform grid with a step of 100 m was created, including measurement points. The interpolation of the DoV and AGG values into points of a uniform grid was performed using the well-known "removal-recovery" method, which allows taking into account the influence of topographic masses and increases the accuracy of map creation [10].

Additionally, the components of the AGG g_x, g_y and the gravitational gradients T_{ij} were calculated using these maps [11]. Fig. 2 shows examples of maps of some parameters of the EGF.

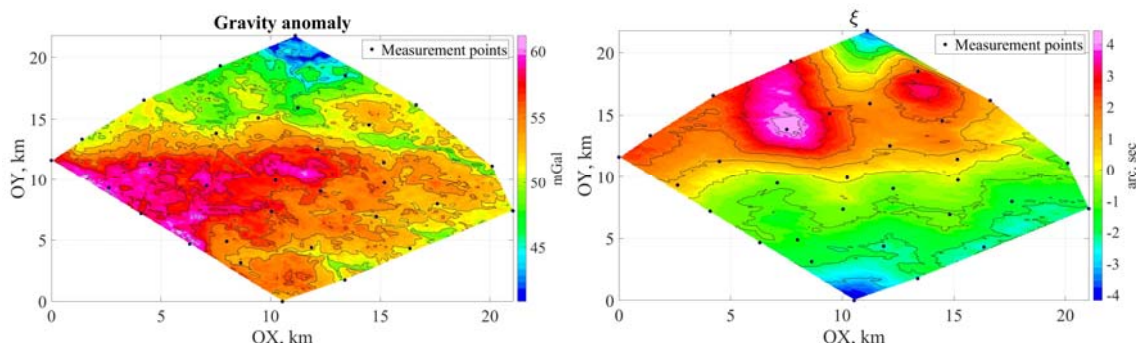


Fig. 2 Examples of created EGF maps

EMF maps. To create maps of the anomalous component of the magnetic field induction, measurements were carried out in tacks at a flight altitude of 150 m with a distance between tacks of 200 m. A magnetovariation station was located in the measurement area. The map of the anomalous component of EMF induction, created based on the results of these measurements, is shown in Fig. 3a. The created map of the EMF is planned to be used in testing the model of the navigation system, which is being created at the Federal State Unitary Enterprise VNIIFTRI. The model includes the above-mentioned magnetometers and quadcopter, as well as a INS on MEMS sensors (Fig. 3b).



Fig.3 Anomalous EMF map

Conclusion. The paper presents a geophysical complex including EGF and EMF parameter meters. This complex allows creating maps of AGG, DoV, components of AGG, gravity gradients, as well as a map of the anomalous component of the EMF. These maps can be used, in particular, in the creation and testing of integrated navigation systems for the EGF and EMF.

The EMF map created using the complex will become a reference when testing the developed layout of the navigation system.

The material for this article was prepared with the support of the Russian Science Foundation grant No. 23-67-10007.

REFERENCES

1. **Denisenko O.V., Pustovoi V.I., Silvestrov I.S., Fateev V.F.** Problems of development of seamless assistive navigation technology in GNSS GLONASS based on measurements of geophysical field parameters // Almanac of modern metrology. 2020. No. 4 (24). P. 127-160.
2. **Sazonova T.V.** Experimental studies of the accuracy characteristics of correlation-extreme navigation systems based on the Earth's magnetic field // Almanac of modern metrology. 2020. No. 4 (24). P. 86-96.
3. **Stepanov O.A., Nosov A.S.** Algorithm for correcting a navigation system based on map and measuring device data that does not require preliminary estimation of the field values along the traveled trajectory // Gyroscopy and navigation. 2020. Vol. 28, No. 2 (109). P. 70-90. DOI 10.17285/0869-7035.0029.
4. **Canciani, A.J., Raquet, J.F.** Airborne Magnetic Anomaly Navigation // IEEE Transactions on Aerospace and Electronic Systems. 2017. Vol. 53, no. 1. P. 67-80. DOI: 10.1109/TAES.2017.2649238.

- V. G. Peshekhonov and O. A. Stepanov (eds.) «Methods and Technologies for Measuring the Earth's Gravity Field Parameters» // *Earth Systems Data and Models* 5, <https://doi.org/10.1007/978-3-031-11158-7>.
5. **H. Liu et al.**, «Comprehensive Features Matching Algorithm for Gravity Aided Navigation» // *IEEE Geoscience and Remote Sensing Letters*, vol. 19, pp. 1-5, 2022, Art no. 1505305, doi: 10.1109/LGRS.2022.3192408.
 6. **V. G. Peshekhonov and O. A. Stepanov** (eds.) «Methods and Technologies for Measuring the Earth's Gravity Field Parameters» // *Earth Systems Data and Models* 5, <https://doi.org/10.1007/978-3-031-11158-7>.
 7. **Popadyev V.V., Soroka A.I., Polubekhin A.I., et al.** Correction capabilities of inertial navigation systems based on gravimetric maps of the earth // *Scientific Bulletin of Moscow State Technical University of Civil Aviation*. 2015. No. 222. Pp. 90-97.
 8. **Peshekhonov V.G.** The problem of plumb line deviation in high-precision inertial navigation // *Gyroscopy and Navigation*. 2020. Vol. 28, No. 4 (111). P. 3-15. DOI 10.17285/0869-7035.0046.
 9. **Murzabekov M.M., Fateev V.F., Yuzefovich P.A.** Measurements of plumb line deviations at a well-known Moscow attraction using a digital astrometer // *Astronomical Journal*. 2020. Vol. 97, No. 10. Pp. 873-880. DOI: 10.31857/S0004629920100059.
 10. **Meng Y., Hirt C., Pail R.** TGF: A New MATLAB-based Software for Terrain-related Gravity Field Calculations // *Remote Sensing*. 2020. 12. 1063. DOI: 10.3390/rs12071063.
 11. **Ogorodova L.V.** Normal field and definition of anomalous potential. Moscow: MIIGAiK. 2010. P. 106.

D. O. GAVRILOV, A. V. IVLIEV
(Samara National Research University, Samara)

DEVELOPMENT OF AN ACTUATOR FOR A MAGNETIC ORIENTATION SYSTEM FOR A NANOSATELLITE

The issue of orientation of satellites is important for small-sized spacecrafts. In this paper, a magnetic executive device of the orientation system is designed, which has competitive efficiency compared to samples presented on the market, due to less energy consumption and compact sizes.

Introduction. To conduct most studies and experiments in space requires a certain orientation of the spacecraft. Magnetic executive bodies are gaining more and more widespread in application in the tasks of orientation of small spacecraft, the number of launches of which increases. This is due to affordable element database of devices, low cost and high reliability [1]. It is worth noting that magnetic systems of active stabilization without a magnetic core require great energy consumption to create the necessary control moment. The proposed report is devoted to the development of an executive device of the magnetic system of orientation with a core, which has high efficiency in small energy consumption.

The purpose of the work: Development of an executive device of the magnetic system for orientation of nanosatellites, which would generate the greatest magnetic moment with minimal energy consumption and ensure efficiency at the level of the best modern samples.

It was decided to make a magnetic coil rod from a magnetic metal with a 1J85 Permalloy's brand, since it has the greatest relative magnetic permeability of available materials [2]. The general view of the experimental installation is presented in the photograph, Fig. 1.



Fig. 1. Experimental installation

In the course of the work, the theoretical calculation, the design and manufacture of the executive device was carried out, as well as the experimental definition of the achieved parameters of the magnetic orientation executive device.

To conduct the experiment, a current of 0.2A (voltage 1.8V) and a current of 0.38A (voltage 3.3V) were supplied to the coil, due to the limitation of the maximum permissible current of the SamSat satellite power supply system.

The experimental data presented in Tables 1 and 2 showed that they practically coincide with the theoretically calculated values of the parameters of the developed magnetic executive body. Additional studies have also been conducted to determine whether the magnetic moment is influenced by the housing of the magnetic actuator. As tests have shown, the housing of the magnetic actuating device did not have a disturbing effect on the created magnetic moment.

Table 1

№	J = 0.2A, U = 1.8V			J = 0.38A, U = 3.3V		
	Mx, A·m ²	My, A·m ²	Mz, A·m ²	Mx, A·m ²	My, A·m ²	Mz, A·m ²
1	0.8942	0.0473	0.0406	1.1271	0.0525	0.0895
2	0.9041	0.0649	0.0132	1.1504	0.0571	0.0118
3	0.8752	0.0416	0.0382	1.1599	0.0772	0.0263

Table 2

Experimental data on the magnetic moment of a magnetic actuator with housing

№	J = 0.2A, U = 1.8V			J = 0.38A, U = 3.3V		
	Mx, A·m ²	My, A·m ²	Mz, A·m ²	Mx, A·m ²	My, A·m ²	Mz, A·m ²
1	0.8268	0.0411	0.0061	1.1437	0.0713	0.0291
2	0.9447	0.0146	0.0454	1.1767	0.0059	0.0155
3	0.8532	0.0423	0.0234	1.1623	0.0693	0.0371

A comparative table of the resulting magnetic actuator with analogues available on the market is presented below.

Table 3

Comparative table of magnetic actuators

Name	Dimensions, mm	Magnetic moment, A·m ²	Consumption, W	Weight, g
The developed magnetic actuator	7×150	0.9	0.36	70
SX-MT-1 [4]	16×140	1.00	0.4	200
CUBETORQUER M [5]	18×77	0.66	0.75	72
iMTQ Magnetorquer [3]	96×90×17	0.2	1.2	196

The novelty of the research is confirmed by the patent of the Russian Federation [6].

Conclusion. In that way, the developed magnetic actuator has compact dimensions, lower energy consumption and a comparable magnetic moment, which confirms the relevance of this development and further research in this direction for use in small spacecrafts.

LITERATURE

1. **Ovchinnikov, M.Y.** Investigation of the speed of the active magnetic damping algorithm / M.V.Keldysh Preprints. 2010. No. 16. 32 p.
2. GOST 10160-75 Precision magnetically soft alloys. Technical specifications [Text]. – Introduction. 1976-01-01
3. Magnetic executive bodies [Electronic resource]. – URL: <https://sputnix.ru/ru/priboryi/pribory-microsputnik/ispolnitelnyie-organyi-sistemyi-orientaczii-stabilizaczii-i-navigaczii/magnitnie-ispolnitelnie-organi> (date of application: 05/23/2024).
4. CUBESPACE CUBETORQUER [Electronic resource]. – URL: <https://www.cubespace.co.za/products/gen-1/actuators/cubetorquer/> (date of application: 05/23/2024).
5. **Kostyukov, A. S.** Development of executive bodies of an active magnetic orientation system for the SIBCUBE class CubeSat student nanosatellite / A.S. Kostyukov, D. M. Zuev, S. A. Babich // Reshetnev readings. - 2014. – Vol. 1. – pp. 502-503.
6. Patent No. 2823985. Russian Federation. Magnetic orientation system for nano- and microsatellites. Belokonov I.V., Ivliev A.V., Kumarin A.A.; applicant and patent holder - Samara National Research University named after Academician S.P. Korolev; application No. 2023130442; priority dated 11/21/2023; published 05/28/2024.

V. V. POTEKHIN, E. V. KUKLIN, P. K. SMIRNOV[□]
(Peter the Great Saint Petersburg Polytechnic University, Saint Petersburg)

CONTROL OF INDUSTRIAL DISTRIBUTED SYSTEMS BASED ON OPEN INFORMATION TECHNOLOGIES

This paper discusses the Open Process Automation Standard (OPAS), which is intended for industrial automated systems. The article analyzes the difference between information technology (IT) and operational technology (OT), as well as the main problems that the OT sector currently faces. The article discusses existing OPAS prototypes and test stands that demonstrate the possibility of using open standards in industry. The paper highlights the importance of moving to open architectures that foster collaborative development and innovation in automation.

Introduction. With the advent of open source software and open architectures, organizations' business structures and working methods are undergoing significant changes. While there is a rapid growth of open solutions in the field of information technology, the field of operational technologies (OT) is still dominated by proprietary systems. Restrictions related to closed interfaces and lack of compatibility between devices from different manufacturers are hindering the development of the sector. In this regard, the Open Process Automation Forum (OPAF) develops the OPAS standard, aimed at creating open solutions for process automation.

Management of the rehabilitation process in medical cyberphysical systems. Information technology (IT) covers the systems and tools used to process and manage data, including software, servers, and networks. Operational technologies (OT), in turn, are concerned with the management of physical processes and systems such as production lines, power grids, and transportation systems. The main difference between them is that IT is more focused on data and information, while OT is focused on physical interaction with the world around you. Despite the differences, IT and OT are beginning to overlap, especially in the context of the Internet of Things (IoT) and Industrial Internet of Things (IIoT) concepts, which requires organizations to rethink their strategies and approaches to system development.

The main challenges facing the OT sector include:

1. Closed systems: Proprietary solutions limit the integration and collaboration of different devices and platforms.
2. Long service life of equipment: Outdated technologies can be difficult to upgrade, which hinders the introduction of new solutions.
3. Security: Increasing the number of connected devices creates new vulnerabilities and security risks for production systems.

The transition to open standards in the field of OT provides the following advantages:

- Increased compatibility: Open interfaces allow devices from different manufacturers to work on the same system.
- Lower costs: Using open solutions reduces dependence on specific vendors and reduces licensing costs.
- Faster adoption of new technologies: Thanks to open standards, developers can adapt and implement new solutions faster.

Conclusion. The OPAS standard represents an important step towards modernizing and opening up operational technologies. Moving to open architectures can solve many of the current challenges of the OT sector, including integration, security, and innovation. Implementing such standards will allow organizations not only to improve their production processes, but also to create more competitive and adaptive business models.

REFERENCES

1. **Potekhin V.V., Alekseev A.P., Kuklin E.V., Misnik A.E., Khitrova A.D.** Programming of open distributed industrial systems based on the international standard IEC 61499, Computing, Telecommunications and Control, 2024, pp. 12-13

2. **Potekhin V.V., Alekseev A.P., Kuklin E.V., Khitrova A.ДA.D., Kozhubaev Yu.H. N.,** CLOUD DISTRIBUTED CONTROL SYSTEM BASED ON OPEN PROCESS AUTOMATION PLATFORM, COMPUTING, TELECOMMUNICATIONS AND CONTROL, 2023, pp. 19-21
3. **Zoitl, T., Strasser, C., Sunder, Baier T.** Is IEC 61499 in harmony with IEC 61131-3? IEEE Ind. Electron. Mag. 2009, Vol. 3, pp. 49–55.
4. **Church P., Mueller H., Ryan C., Gogouvitis S.V., Goscinski A., Tari Z.** Migration of a SCADA system to IaaS clouds – a case study. Church et al. Journal of Cloud Computing: Advances, Systems and Applications. 2017, pp. 6-12.
5. **O-PAS Standard, Version 2.1: Part 1** – Technical Architecture Overview, pp. 6-10.
6. **O-PAS Standard, Version 2.1: Part 1** – Technical Architecture Overview, pp. 12-17.

A. K. GOLUBEV, A. A. PYRKIN, V. M. FOMIN
(ITMO University, Saint Petersburg)

SENSORLESS CONTROL OF INDUCTION MOTOR

In this paper, solves the problem of sensorless control of induction motor. A control algorithm able to operate under parametric and signal uncertainty is proposed. The proposed algorithm allows to expand the application area of induction motors in robotic technical systems with changing load and incomplete information about the parameters of the model. The performance is confirmed by the results of computer modeling.

Introduction. Induction motors are used in automation systems because of their efficiency and reliability. However, when controlled by traditional methods, under conditions of changing load, external and internal uncertainty, problems arise, in which case systems using adaptive control algorithms have a high relevancy index.

In this paper, we propose a sensorless vector control algorithm for a discrete model of an induction motor. The algorithm works in a wide range of parametric and signal uncertainty, which makes it promising for use in modern robotic systems, with increased requirements for accuracy and reliability, as well as when there is a lack of a priori information about the modes of operation and operating conditions.

Results. The dynamic model of an induction motor in a stationary frame of reference related to the stator in continuous time is defined by the following equations [1]:

$$\begin{aligned} \dot{\lambda} &= -\left(\frac{R_r}{L_r} \mathbf{I} - n_p \mathbf{J} \omega\right) \lambda + \frac{R_r L_m}{L_r} i, \\ \frac{di}{dt} &= -\left(\frac{R_s}{L_s \sigma} + \frac{R_r L_m^2}{\sigma L_s L_r^2}\right) i + \frac{L_m R_r}{\sigma L_s L_r} \left(\frac{R_r}{L_r} \mathbf{I} - n_p \mathbf{J} \omega\right) \lambda + \frac{1}{\sigma L_s} v, \\ \dot{\omega} &= \frac{1}{D} (\tau - \tau_L), \end{aligned} \quad (1)$$

where: λ – rotor flux; i – stator current; v – stator voltage; ω – rotor velocity; R_r и L_r – rotor resistance and inductance, respectively; R_s и L_s – stator resistance and inductance, respectively; L_m – mutual induction; $\sigma = 1 - \frac{L_m^2}{L_s L_r}$ – inductance leakage factor; n_p – number of pole pairs; D – inertia torque; τ – electromagnetic torque; τ_L – load torque; \mathbf{I} – 2x2 identity matrix; $\mathbf{J} = \begin{bmatrix} 0 & -1 \\ 1 & 0 \end{bmatrix}$.

As can be seen, the model (1) is nonlinear, which largely complicates the synthesis of regulators. In practical implementation, a regulator with a large gain is used in the current loop:

$$v = \frac{1}{\epsilon} (i^d - i), \quad (2)$$

where: i^d – desired stator current value; ϵ – small positive coefficient.

In the limiting case, the coefficient in equation (2) tends to 0 and the motor model (1) is simplified. Performing the transition to the frame of reference rotating with the rotor and sampling the motor model, the following is obtained [2, 3]:

$$\begin{aligned} \lambda_{k+1} &= a \lambda_k + (1 - a) u_k, \\ \tau_k &= b u_k^T \mathbf{J} \lambda_k, \\ \omega_{k+1} &= \omega_k + c \tau_k - d \tau_L, \end{aligned} \quad (3)$$

where: $a = e^{-\frac{R_r T}{L_r}}$; $b = \frac{n_p}{L_r}$; $c = \frac{(1-a)L_r}{DR_r}$; $d = \frac{T}{D}$; T – sampling period; u – stator voltage in the rotating reference frame.

Assuming that the rotor inductance L_r and the lower bound of the inertia torque D are known, the equations of the adaptive discrete-time regulator are obtained:

$$\begin{aligned}
 u_k &= e^{J\rho_k^d} \left(\frac{\Psi_{k+1}^d}{1-\hat{a}} \cos(\beta_k) - \frac{\hat{a}}{1-\hat{a}} \Psi_k^d \frac{L_r}{\Psi_k^d n_p} \tau_k^d \right), \\
 \rho_{k+1}^d &= \rho_k^d + \beta_k, \\
 \beta_k &= \arcsin \left(\frac{L_r(1-\hat{a})}{n_p \Psi_{k+1}^d \Psi_k^d} \tau_k^d \right), \\
 \tau_k^d &= C(z)(\omega^d - \omega_k), \\
 C(z) &= K_p + K_I \frac{z}{1-z},
 \end{aligned} \tag{4}$$

where: Ψ^d – desired value of amplitude of rotor flux; τ^d – desired value of torque; ω^d – desired value of rotor velocity; $a = e^{\frac{-R_r}{L_r}}$; \hat{R}_r – rotor resistance estimation value, obtained, for example, using the DREM method [4]; K_p, K_I – values of proportional and integral coefficients of the torque regulator.

Replacing in equations (4) the value of rotor velocity by its estimation obtained using an observer, the algorithm of which is given in [4, 5], it turns out that the algorithm (4) does not require direct information about the rotor velocity, and thereby becomes sensorless.

In Figure 1 shows the results of computer modeling in MATLAB/Simulink environment of the algorithm of sensorless control of induction motor. The following values of motor parameters were used: $L_s = L_r = 420$ mH, $L_m = 117$ mH, $R_s = R_r = 2.76$ Ω , $D = 0.06$ kg*m², $\Psi^d = 0.0455$ Wb, $\omega^d = 50$ rad*s⁻¹, $n_p = 2$. The sampling period T was taken as 1 second and the load torque as 0.1 N*m. The modeling was performed in scenarios with parametric and signaling uncertainties.

Conclusion. In the result of this work, a sensorless adaptive control algorithm for a discrete induction motor model was synthesized. The proposed algorithm has demonstrated good performance under conditions of different kinds of uncertainties of the motor model. Various applications in robotic tasks, where inaccurate knowledge of the values of the model parameters is possible, under noise of the measured electrical signals, as well as the impossibility of using the rotor position sensor, are highlighted as prospects for the use of the algorithm. In the future it is planned to tighten some of the introduced assumptions, as well as experimentally verify the presented results on real technical systems.

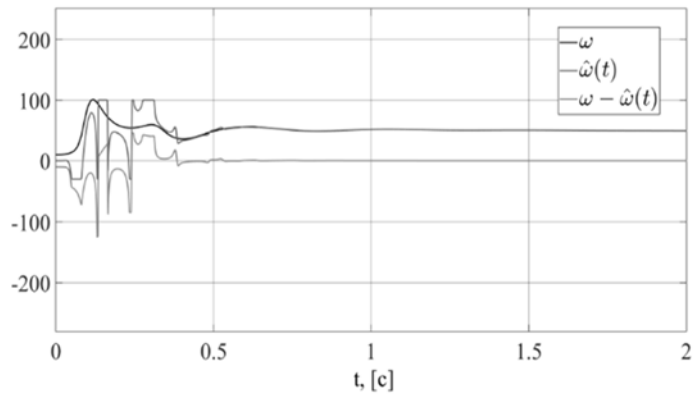


Fig. 1. Modeling results in sensorless mode

REFERENCES

1. Pyrkin A., Bobtsov A., Vedyakov A., Ortega R., Vediakova A., Sinetova M. A flux and speed observer for induction motors with unknown rotor resistance and load torque and no persistent excitation requirement // Intern. Journal of Adaptive Control and Signal Processing. 2021. Vol. 35, N 8. P. 1578–1593.
2. Romeo O., Damia T. On Discrete-time Control of Current-fed Induction Motors // System & Control Letters. – 1996. – T. 28, №3. – C. 123-128.
3. Ngyen Q. C., Pyrkin A. A., Golubev A. K. Sensorless control algorithm for induction motor using adaptive observers. Journal of Instrument Engineering. 2024. Vol. 67, N 7. P. 551–558 (in Russian). DOI: 10.17586/0021-3454-2024-67-7-551-558.
4. Pyrkin, A., Q. C. Nguyen, M. Sinetova, R. Ortega, and A. Bobtsov. 2024. “Adaptive Field-Oriented Control of Current-Fed Induction Motors: A Discrete-Time Implementation.” *International Journal of Control*, July, 1–11. doi:10.1080/00207179.2024.2368056.
5. Pyrkin A., Bobtsov A., Vedyakov A., Ortega R., Vedyakova A., Sinetova M.M. DREM-Based Adaptive Observer for Induction Motors // Proceedings of the IEEE Conference on Decision and Control (CDC), 2019, pp. 648-653.

M.A. TIT, A.G. SCHERBAK
(Concern CSRI Elektropribor, JSC, St. Petersburg)

O.S. YULMETOVA
(Concern CSRI Elektropribor, JSC, ITMO University, St. Petersburg)

EXPERIENCE IN DEVELOPING A TECHNOLOGY OF PRECISION SPHERICAL UNITS MANUFACTURE

The article presents the experience of developing the advanced technological solutions for correcting imbalance and applying a contrast pattern to the surface of precision spherical units used in gyroscope instrument making.

Introduction. Spherical units are the basis for the most promising products in gyro instrument making [1,2]. Strict requirements for shape accuracy and imbalance are imposed on these units. An equally important technological task is the process of applying contrasting patterns that determine the operation of the optoelectronic data readout system [1]. The originality of the approaches presented in the paper consists in solving the above tasks through the use of laser processing methods.

Spherical units manufacturing technology. A spherical unit is a precision beryllium sphere with a pronounced moment of inertia created by reinforcing elements formed in the unit body [3], with an imbalance rated by hundredths of a micrometer, and a contrasting pattern marked on the surface of the unit. The spherical units manufacturing technology includes a number of successive operations that determine the redistribution of masses and the structural and phase modification of the material. These processes are described rather completely using the chemical thermodynamics approach [4, 5].

At the same time, traditional balancing methods based on the use of directed finishing [6] do not always provide the required imbalance and accuracy of the shape of spherical units.

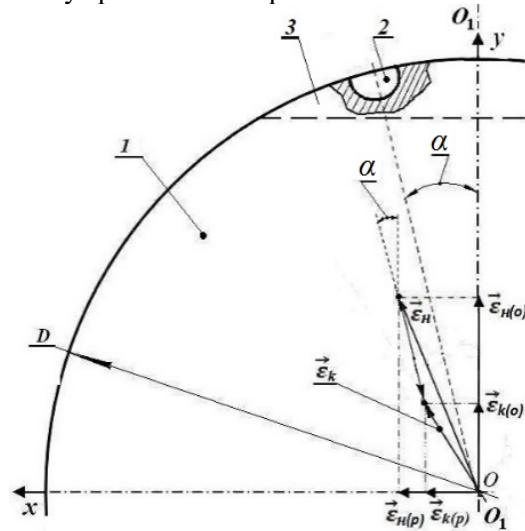


Fig. 1. Imbalance correcting scheme: 1 – spherical unit, 2 – recess, 3 – spherical segment where the recess is made.

by the relation: $\alpha = \arctg \frac{\epsilon_n(p) - \epsilon_k(p)}{\epsilon_n(o) - \epsilon_k(o)}$, where $\vec{\epsilon}_n(p)$ and $\vec{\epsilon}_k(p)$ are the radial components of the initial and final imbalance vectors, respectively.

The final operation in the beryllium spherical unit manufacturing cycle is the generation of a contrast pattern. The evolution of this process can be represented as follows: the electrochemical method (before 2012) [8, 9], limited in the attainable optical parameters of the pattern and reducing the accuracy of the spherical unit shape, and method of laser marking (from 2012 to the present day) [10, 11].

In this paper, the **imbalance correction** was performed by local evaporation of a point mass from the surface of a spherical unit [7] until the required final imbalance $\vec{\epsilon}_k$ was obtained, at an angle α of the recess axis tilt to the symmetry axis O_1O_1 of the spherical unit 1 (Fig. 1). In this case, the conditions are provided: laser evaporation of a given mass m and formation of a point recess 2 are performed outside the raster pattern zone, and the mass m is determined from the relationship $m = 2M \frac{\epsilon_n(o) - \epsilon_k(o)}{D \cos \alpha}$, where M is the mass and D is the diameter of the spherical unit, $\vec{\epsilon}_n(o)$ and $\vec{\epsilon}_k(o)$ – are the axial components of the initial $\vec{\epsilon}_n$ and final $\vec{\epsilon}_k$ imbalance vectors, respectively. An important factor is the determination of the recess position specified by the inclination angle α , defined

Laser technology has provided a number of advantages in terms of the quality of the applied pattern, including uniformity of the contrast of the resulting pattern, as well as minimization of the spherical unit deformations, as compared to the electrochemical method [7].

In this case the generation of a pattern on the beryllium surface is well described by the chemical thermodynamics approach [3], which can serve as the basis for a descriptive model of the laser treatment process. Modeling is associated with the calculation of the Gibbs energy values for possible interactions in the “metal surface – gas environment components” system:

$$\Delta Z_T^0 = \Delta H_{298}^0 - T \cdot \Delta S_{298}^0 + \int_{298}^T C_p dt - T \cdot \int_{298}^T 1/T \Delta C_p dt + RT \ln P_g^{-k},$$

where C_p – heat capacity; T – temperature; P_g – relative partial pressure of the gas environment component g taking part in the reaction, R – absolute gas constant, k – stoichiometric factor.

Comparison of the Gibbs energy values and selection of the chemical reaction with the lowest value of this factor allows us to determine the phase composition of the compound that forms a contrast pattern in the process of laser treatment on the spherical unit surface [2, 3]. Varying the partial pressures of the gas environment components during laser treatment allows us to change the surface conductivity of the spherical unit in the pattern area, which is illustrated by the differential conductivity curves obtained by scanning probe microscope investigation (NT-MDT Nanoeducator) (Fig. 2). The analysis of the Gibbs energy values shows that after laser marking of beryllium in a nitrogen environment, the composition of the laser raster is determined by the Be_3N_2 nitride [5], which is completely consistent with the X-ray phase analysis data (Fig. 3).

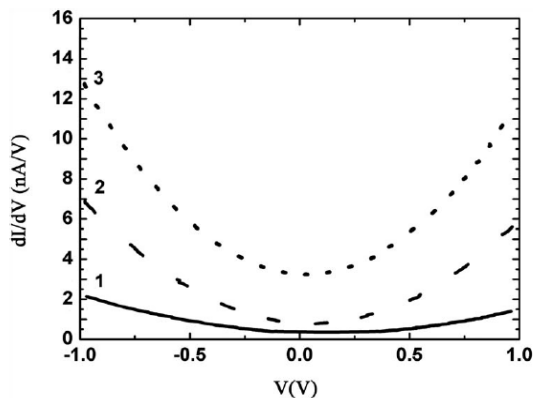


Fig. 2 Curves of differential conductivity of a laser pattern generated in the air environment (1), in nitrogen environment (2), and on the base surface of beryllium (3)

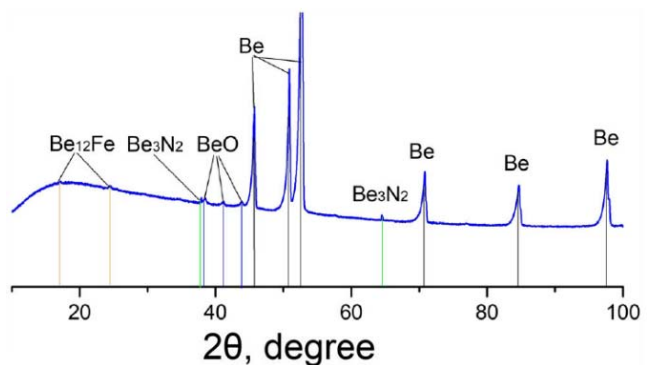


Fig. 3 X-ray diffractograms of a laser pattern obtained in the process of treatment of the beryllium spherical unit in nitrogen environment

Conclusion. The example of a precision spherical unit shows the efficiency of applying the laser treatment methods in generation of the most important functional parameters of the unit during its manufacture. Mathematical models describing the relationship between the parameters of the spherical unit and the geometrical arrangement of the evaporated mass are used as tools for modeling of technological processes for correcting the imbalance. The use of a chemical thermodynamics approach for studying contrast patterns obtained by means of laser surface treatment is proposed.

REFERENCES

1. Landau, B.E., *Elektrostaticheskii giroskop so sploshnym rotorom* (Electrostatic Gyroscope with a Solid Rotor), St. Petersburg: CSRI Elektropribor, 2020, 150 p.
2. Landau, B.E. et al., 2021 *J. Phys.: Conf. Ser.* 1864012008
3. Belyaev, S.N., Landau, B.E., Butsyk, A.Ya., et al., Method of ball gyro rotor manufacturing, Patent RU 2286535, 2006.
4. Yulmetova, O.S., Scherbak, A.G. Contrast image formation based on thermodynamic approach and surface laser oxidation process for optoelectronic read-out system, *Optics and laser technology*. 2018. Vol. 101, pp. 242–247.
5. Yulmetova, O.S., Scherbak, A.G., Composition analysis of thin films formed on beryllium surfaces under pulsed laser action by the method of chemical thermodynamics, *International Journal of Advanced Manufacturing Technology*. 2018. Vol. 97, No. 9–12, pp. 3231–3236.

6. **Filippov, A.Yu., Fedorovich, S.N., Shcherbak, A.G.** Integrated approach to the technology of manufacturing electrostatic gyro rotors, *Journal of Physics: Conference Series*, 13th Multiconference on Control Problems, MCCP 2020, 2021, p. 012023
7. **Yulmetova, O.S., Scherbak, A.G., Filippov, A.Yu., Landau, B.E., et al.**, Method of electrostatic gyro rotor manufacturing, Patent RU 2592748, 2016.
8. **Agroskin, B.N., Gallai, V.I., et al.**, Comparative assessment of electrochemical and photochemical methods of forming a light-contract image on the rotor of a gimballess electrostatic gyro, *Giroskopiya i navigatsiya*, 1996, no. 3, pp. 39–45.
9. **Yulmetova O.S., Tit M.A., Sisyukov A.N., Yulmetova R.F.** Comparative analysis of electrochemical and laser marking for gyroscopic application. *Proc. of the 2020 IEEE Conference of Russian Researchers in Electrical and Electronic Engineering (EIConRus)*, 2020, pp. 1053–1055.
10. **Yulmetova, O.S., Scherbak, A.G., Butsyk, A.Ya., Landau, B.E., Veiko, V.P., and Valetov, V.A.**, Method of electrostatic gyro rotor manufacturing, Patent RU 2498224, 2013.
11. **Fedorovich, S.N., Filippov, A.Yu., Shcherbak, A.G., and Leonova, T.G.**, Method of electrostatic gyro rotor manufacturing, Patent RU 2812538, 2024.

M.A. VLASOVA, V.V. CHALKOV
(Concern CSRI Elektropribor, JSC, St. Petersburg)

DEVELOPMENT OF A MODULAR STAND FOR TESTING QUANTUM SENSOR OPTICAL CELLS BASED ON A REFERENCE STANDARD

The paper presents the results of development of a modular stand for testing optical cells used in quantum sensors. The test stand development is aimed at providing the high accuracy of positioning and efficient testing of the cells during the laboratory research. The testing results show the effectiveness of the proposed approach and its potential for further research in the field of quantum technologies.

Introduction. Quantum sensors include both advanced [1 - 2] and proven units [3 - 4] designed to perform high-accuracy measurements of various physical quantities, such as magnetic field, angular rate, time and frequency. These units include quantum magnetometers, atomic frequency standards and gyroscopes, which use the quantum properties of atoms to achieve the exceptional accuracy and stability. Although some quantum sensors are still under development, their present characteristics show significant advantages in the dedicated applications [6, 7]. However, a number of quantum sensors still require further research. The key element of quantum sensors is the cells with a working agent, in which atoms interact with electromagnetic radiation. The quality of such cells directly affects the accuracy and stability of measurements that makes their testing an important stage in the development of quantum sensors. At present, the cells production technology and selection of vapors, optimal for particular applications, remain experimental. Parameters of cells in different batches can vary significantly, and this requires strict quality control and evaluation of their characteristics. One of the efficient non-destructive methods for the cells quality control and assessment of their characteristics is the measurement of the optical resonance width [8, 9]. The use of classical optical equipment [10, 11] for testing such cells can be expensive and difficult, especially in conditions of unstable or non-standard cell geometry.

The purpose of this work is to develop a test stand for comparative analysis of optical cells using a modular structure. The proposed stand allows for non-destructive quality control of cells manufacturing and filling by comparing the reference and tested cells [12]. Additive technologies in developing the stand made it possible to apply a concept of modular design thus ensuring flexibility of adapting the stand to different types of cells. If it is necessary to test a non-standard cell, a module conforming to its size and shape can be quickly developed and printed, providing independent temperature control for the cell thus minimizing the costs and time for preparing to the experiment not decreasing stability of measurements.

Spectroscopic analysis of vapor cells. The spectroscopic analysis of the alkali metal absorption line is an efficient method for non-destructive testing of vapor cell parameters [13], because it allows us to identify defects that occur during their filling, such as the absence of buffer gas, its insufficient amount, or damage to the cell integrity, while leaving the cell suitable for use [14]. In this study, the cell is tested using a laser with a wavelength of 895 nm, corresponding to an optical transition in cesium 133 atoms. When light interacts with cesium atoms, resonant absorption of radiation occurs, associated with transitions between hyperfine levels [15-17].

Energy transitions in cesium 131 atoms have a hyperfine splitting of 9.2 GHz for the ground state and 1.2 GHz for the excited state, which creates four clear resonance lines. The increased buffer gas pressure in the test cell as compared to the reference cell reduces the time of cesium atoms relaxation due to collisions with buffer gas atoms, which in turn leads to a broadening of the resonance line.

Evaluation of the resonance line broadening relative to the reference cell allows us to judge the quality of filling the cell under study. The use of a reference cell makes it possible to carry out such measurements without the use of expensive optical spectrum analyzers.

Test stand description. For the approach described above, a stand was designed, which included two optical cells: one serves as a reference cell, and the other is a test sample. Both cells are illuminated by a single laser source, which ensures identical conditions for measurements. The light flux is divided by a beam splitting cube with a factor of 90/10, where 10% of the light is directed to

the reference cell, and the remaining 90% – to the test cell. Such splitting was chosen because the shape of each test cell can vary, increasing the light loss.

Due to the expected differences in gas composition, the cells require different temperature conditions to achieve a similar concentration of alkali metal. This is achieved by the modular design of the stand: each cell is located in its own module with independent temperature control, which allows the required temperature to be set for each cell. A vertical-cavity surface-emitting laser (VCSEL laser L895VH1) is used as a light source. A lasing wavelength can be controlled by changing both the temperature and the current. To simplify setting the wavelength of the laser, it is also located in a module with independent temperature control, which allows us to change the wavelength by varying only the strength of the injection current.

It should be noted that the VCSEL family of light sources have low power and light beam concentration compared to emitters with an external resonator, which restricts the accuracy of positioning the cells, laser cube and photodetector on the same optical axis, with an acceptable deviation of no more than 0.5 mm.

A photodetector is installed behind each optical cell, which records the intensity of the transmitted light. The signals received from the photodetectors are transmitted to the data analysis device. A schematic representation of the stand is shown in Figure 1.

Since the concentration of the alkali metal in the cell directly depends on its temperature, and the lasing wavelength is subject to temperature changes, the testing process requires reliable temperature protection against the environment and easy access to all elements of the stand. Therefore, a material with high heat capacity was chosen for manufacturing the stand. The stand is designed with provision for testing cells of various shapes without the need for additional modification of the whole stand; to test non-standard cells, it is enough to replace the module for the cell being tested with a suitable one. To ensure such functionality, separate modules are integrated into the main body of the stand, each of the modules having independent temperature control.

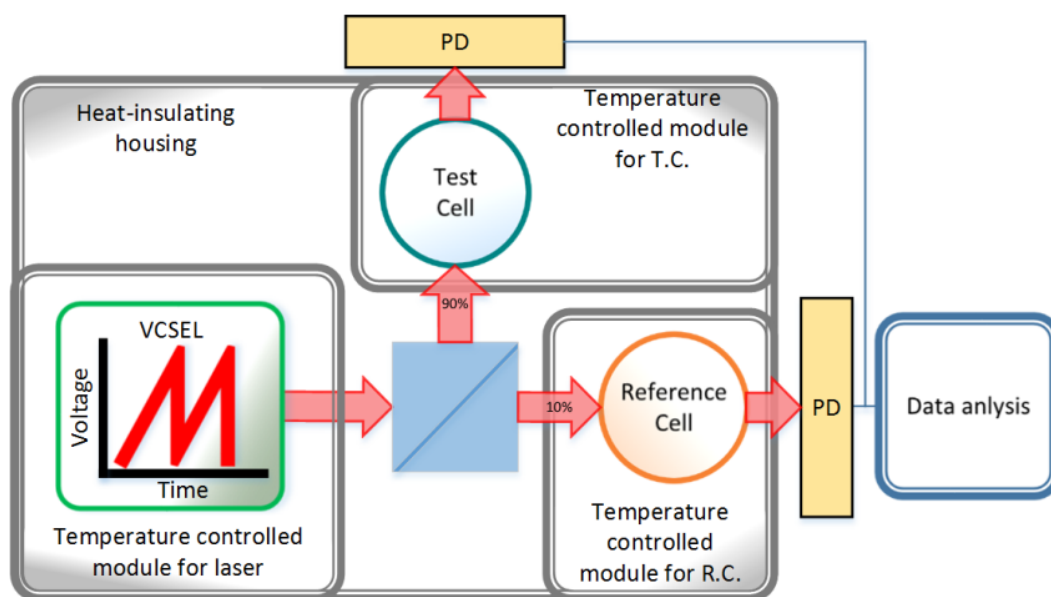


Fig. 1. Schematic view of the stand for testing optical cells: R.C. – reference cell; T.C. – tested cell; VCSEL - vertical-cavity surface-emitting laser; PD - photodetector

Experiment procedure. Injection current, changing according to a sawtooth law within the range of 1.2-1.4 volts, is supplied to the laser heated to the operating temperature. As the cells heat up, the concentration of alkali metal vapors increases, and when the absorption peak is reached, equal to 60-100% of the amplitude of the laser scanning signal for the tested cell and 160-190% for the reference cell, the signals from the photodetectors are recorded. These values are valid only for the checked cells and should be determined experimentally based on the saturation of cesium in the cells, which indicates the termination of the absorption peak increasing during resonance broadening.

The signals recorded by the photodetectors represent the dependence of the intensity of light, which has passed through the cell and interacted with the substance in it, on the laser injection current (on the

laser radiation frequency). An example of such signals is shown in Figure 2. These signals are used to evaluate the characteristics of the cells being tested. First, the stand allows us to find the cells that were not filled, which indicates a manufacturing defect. For cells successfully filled with the necessary gases, the stand measures the magnitude of the shift of absorption peaks and the half-width of the resonances in the cell being tested relative to the reference cell. These characteristics are subsequently taken as parameters when using the cells.

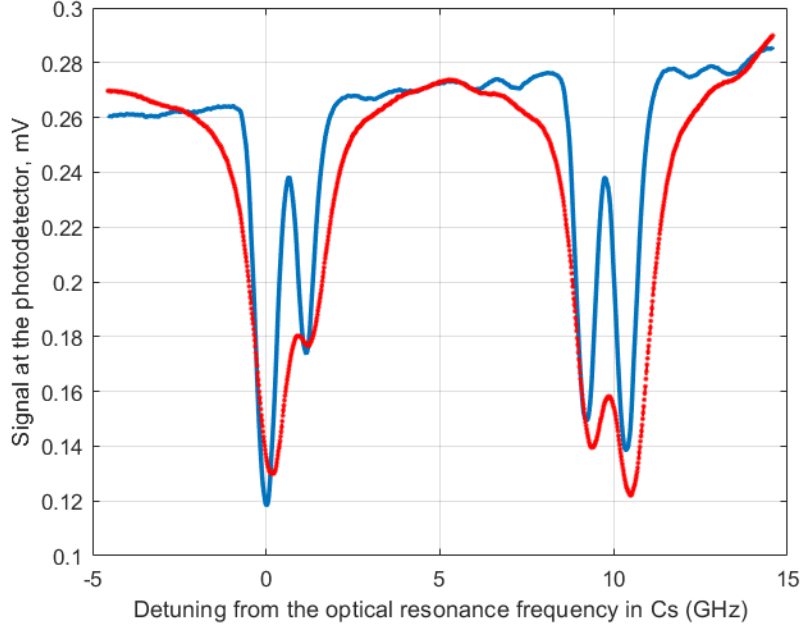


Fig. 2. Results of testing the cells: solid curve — a signal obtained when scanning through the reference cell; dashed curve — a signal received from the cell being tested

The processing of signals, an example of which is shown in Fig. 2, is performed using approximation by four Lorentz profiles [18, 19], taking into account the dependence of the intensity of light emitted by the laser on the injection current:

$$S(\nu) = V + K_p L(\nu - \nu_0) - K_p K_M \left(\frac{\Gamma_{2,1} A_1}{(\nu - \nu_1)^2 + \Gamma_1^2} + \frac{\Gamma_{2,2} A_2}{(\nu - \nu_2)^2 + \Gamma_2^2} + \frac{\Gamma_{2,3} A_3}{(\nu - \nu_3)^2 + \Gamma_3^2} + \frac{\Gamma_{2,4} A_4}{(\nu - \nu_4)^2 + \Gamma_4^2} \right) + V_{ns},$$

where ν is the laser injection voltage; V is the base voltage of the laser injection; K_p is the power/lasing wavelength coefficient; L is the signal slope coefficient; K_M is the coefficient of the laser injection current conversion into the laser radiation frequency; ν_n are currents at which the appropriate resonances are achieved; $\Gamma_{2,n}$ are the relaxation constants of transverse magnetization; Γ_n are sought-for half-widths of the corresponding resonances; A_n are amplitudes of the corresponding resonances; V_{ns} is the noise component, which is a white noise; $n = 1, 2, 3, 4$.

Benefits of additive manufacturing. The accuracy of positioning the optical elements of the stand, taking into account the described restrictions on tolerances, is a complex and high-technology task when using subtractive manufacturing methods, especially without additional adjustment during the experiment. In this context, photopolymer printing provides the required accuracy, reaching values within 0.1 mm, which allows for an efficient and fast implementation of the modular design of the stand.

Conclusions. The paper presents a modular stand for testing optical cells used in quantum sensors, which provides adjustment flexibility and quick replacement of components. An experiment for determining the broadening of the resonance line in a vapor cell relative to the reference cell is described. It is noted that due to the modular approach, the stand maintains high positioning accuracy of optical elements (up to 0.1 mm), and remains cost-effective regardless of the cell geometry and simplifies the stand setup for different experimental conditions.

REFERENCES

1. **Peshekhonov, V.G.**, The outlook for gyroscopy, *Gyroscopy and Navigation*, 2020, vol. 11, no. 3, pp. 193–197. DOI 10.17285/0869-7035.0028.
2. **Popov, E.N., Barantsev, K.A., and Litvinov, A.N.**, Theoretical simulation of a signal for a scheme of an atomic spin gyroscope with optical detection, *Kvantovaya Elektronika*, vol. 49, no. 2, 2019, pp. 169–177.
3. **Ding, M.** Development and prospect of quantum sensing technology, *Proceedings of the 20th Conference of Young Scientists with International Participants "Navigation and Motion Control"*, Eds.: Prof. Peshekhonov, V.G., and Prof. Stepanov O.A., St. Petersburg: Concern CSRI Elektropribor, 2018, 443 p.
4. **Petrov, A.A.**, Methods for improving accuracy characteristics of quantum frequency standards, RIRT, 2021.
5. **Basov, N.G. and Belenov, E.M.**, Ultra-narrow spectral lines and quantum frequency standards, *Priroda*, 1972, no. 12.
6. **Basov N.G. and Gubin M.A.** Quantum frequency standards, *IEEE Journal of Selected Topics in Quantum Electronics*, 2000, vol. 6, no. 6, pp. 857-868.
7. **Alexandrov, E.B. et al.**, Gradiometric study of a quantum magnetometer on cesium vapors, *Zhurnal tekhnicheskoi fiziki*, 2007, vol. 77, no. 3, pp. 100-102.
8. **Nwaboh, J.A. et al.**, Optical path length calibration: a standard approach for use in absorption cell based IR spectrometric gas analysis, *International Journal of Spectroscopy*, 2014, vol. 2014, no. 1, p. 132607.
9. **Yulmetova, O.S. et al.**, Analysis of chemical interactions during filling a cesium vapor cell for a quantum magnetometer, *Nauchno-tekhnicheskii vestnik informatsionnykh tekhnologii, mekhaniki i optiki*, 2024, vol. 24, no. 3, pp. 438-447.
10. US20160349481A1. Monolithic optical mounting element. United States Patent and Trademark Office. Published on 2016-12-01
11. Thorlabs, Inc. (2024). Method of making a pre-aligned optical mount (U.S. Patent No. US11982861B2). U.S. Patent and Trademark Office
12. **Đujić, M. et al.** Comparative analysis of light storage in antirelaxation-coated and buffer-gas-filled alkali vapor cells, *Scientific Reports*, 2024, vol. 14, no. 1, p. 14467.
13. **Bulgakova, V.V. et al.**, Experimental stand for optical pump-terahertz probe diagnostics for studying ultra-fast dynamics of charge carriers in photoconductive media, *ITMO University Conference "Nevsky Photonics-2023"*, St. Petersburg, 2023.
14. **Shevchenko, A.N., Kuzmin, A.G., and Titov, Yu.A.**, Mass-spectrometric measurement of the gas mixtures composition in the cells of a quantum rotation sensor, *Nauchnoe priborostroenie*, 2018, vol. 28, no. 2, pp. 62-68.
15. **Boldyrev, K.N. et al.**, The first observation of the hyperfine level's anticrossing in the optical spectra, *13th International Workshop on Quantum Optics (IWQO-2019)*, 2019, pp. 49-50.
16. **Sargsyan, A.G. et al.**, Investigation of atomic transitions of cesium in strong magnetic fields by an optical half-wavelength cell, *Pis'ma v zhurnal eksperimental'noi i teoreticheskoi fiziki*, 2013, vol. 98, no. 8, pp. 499–503.
17. **Alexandrov, E.B., Vershovskiy, A.K., and Pazgalev, A.S.**, Magnetometer based on a pair of symmetric transitions in the 87Rb hyperfine structure, *Technical Physics*, 2006, vol. 76, no. 7, pp. 103-107.
18. **Vershovskiy, A.K., Dmitriev, S.P., and Pazgalev, A.S.**, Optically pumped quantum magnetometer with combined advantages of Mx and Mz devices, *Technical Physics*, 2013, vol. 58, no. 10, pp. 1481–1488.
19. **Vlasova, M.A. et al.**, Special aspects of the VCSEL lasers use in an installation for monitoring the parameters of quantum sensors gas, 2022.

S.A. FEDOROV, F.S. KAPRALOV
(Lomonosov Moscow State University, Moscow)

SMOOTHING FILTER FOR MICROMECHANICAL GYROSCOPE UNSTABLE BIAS ESTIMATION IN DYNAMIC CALIBRATION EXPERIMENT

Smoothing filter in Rauch-Tung-Striebel form is applied to calibration of a 6-axis low-precision microelectromechanical inertial sensor to obtain more accurate estimates of unstable low-frequency stochastic gyroscope error component. Real experimental data processing indicates that estimates of the unstable gyroscope bias are close to those obtained with the direct method of averaging gyroscope measurements in pre-defined identical static positions. The proposed method, however, does not require any static positions, thus simplifying the calibration experiment while retaining possibility to analyze low-frequency sensor error variation.

Introduction. Microelectromechanical inertial sensors (MEMS) have many advantages such as low power consumption, compactness and low cost. However, accuracy characteristics of such sensors are relatively low in most cases, and use of MEMS sensors in applications requires more complex bias model than a constant value. This applies to calibration experiments as well. The goal of calibration is to estimate parameters of the a priori model of the systematic sensor errors. In 2005, N.A. Parusnikov (Lomonosov Moscow State University) proposed a method for calibrating inertial sensors measurement unit with an algorithm based on the estimation of a linear dynamic system state vector using Kalman filter [1,2]. As in other techniques, quality of calibration parameter estimates can be affected by unstable low-frequency component of gyroscope measurements. This paper considers a modified version of the Parusnikov's method [1,2], based on the application of the Rauch-Tung-Striebel (RTS) smoother [3], which uses the entire set of measurements to estimate the state vector at each time instant. It is expected to provide more accurate estimates for the unstable component of gyroscope measurements over time, as well as less biased estimates for other parameters affected by it.

Estimation problem for calibration parameters. We use the following a priori models for instrumental errors of accelerometers and gyroscopes:

$$f' - f \equiv \Delta f = \Delta f^0 + \Gamma f + \Delta f^s, \quad \omega' - \omega \equiv v = v^0 + \Theta \omega + v^s \quad (1)$$

where f' is a triplet of accelerometer measurements, f contains true components of the measured specific force, Δf^0 is an accelerometer bias, Γ is a matrix of scaling coefficients and sensitive axis misalignments, Δf^s is a stochastic component of accelerometer measurements, ω' is a triplet of gyroscope measurements, ω contains true components of the absolute angular rate, v^0 is a gyroscope bias independent of angular velocity, Θ is a matrix of scaling coefficients and sensitive axis misalignments, v^s is a stochastic component of gyroscope measurements.

We introduce linear dynamic system with the state vector x :

$$x = (\beta_{x^0}, v^0, \Delta f^0, \Gamma, \Theta) \in R^{24}, \dot{\beta}_{x^0} = \hat{u}_{x^0} \beta_{x^0} + L^T v, \Delta \dot{f}^0 = q_{\Delta f}, \dot{v}^0 = q_{v^0}, \dot{\Gamma} = 0, \dot{\Theta} = 0 \quad (2)$$

The calibration problem is stated as the estimation of the state vector x using measurements y , which are:

$$y \equiv L'^T f' - \begin{pmatrix} 0 \\ 0 \end{pmatrix} \approx \begin{pmatrix} 0 & g & 0 \\ -g & 0 & 0 \\ 0 & 0 & 0 \end{pmatrix} \beta_{x^0} + L^T \Delta f \quad (3)$$

where L is an attitude matrix of the instrumental frame, fixed to the accelerometers sensitivity axes, relative to the geodetic frame (East-North-Up), L' is a computed value of L , obtained by integrating kinematic Poisson attitude equation with gyroscope measurements as angular rate components, and a certain initial orientation $L'(0)$, β_{x^0} is a small rotation vector of the orientation error, g is a reference value of local gravity acceleration, $q_{\Delta f}, q_{v^0}$ – white noises with a priori defined variances.

The estimate of the system state vector can be obtained using either standard forward time Kalman filter [3] or smoothing filter in the RTS form [3]. The RTS form of the optimal smoother is preferred because it does not require the Kalman filter to be implemented in reverse time.

Results of experimental data processing. A calibration experiment for an inertial measurement unit (STMicroelectronics, model ISM330DCHX) was performed using a single axis turntable. The

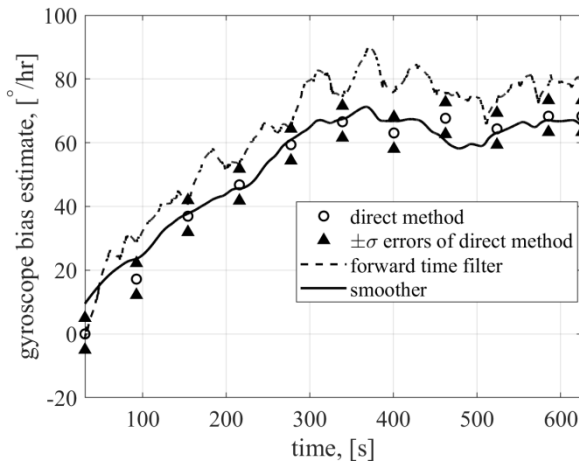


Fig. 1. Gyroscope unstable bias estimates

experiment scheme consisted of sequential rotations around the horizontal turntable axis by 90° , with stops at each angular position for 10 seconds. Such experiment scheme allows a direct method of estimating unstable gyroscope bias by averaging gyroscope measurements in identical static positions. Figure 1 shows a graph of gyroscope bias estimates produced by different methods. The graph indicates that the estimate obtained by the RTS smoother approximates the low-frequency component of the bias variation more accurately than the estimate obtained by the Kalman filter. Moreover, for the RTS smoother to work, it is not necessary to follow a special experiment scheme with static positions. According to simulation results, the

smoothing filter also shows good performance, for example, in case of rotations with constant angular velocity.

Conclusion. The paper considers the problem of a 6-axis MEMS inertial sensor calibration using a smoothing filter in Rauch-Tung-Striebel form to estimate the low-frequency unstable component of gyroscope errors. The results of real and simulated data processing show the advantage of this approach over both the conventional forward-time Kalman filter and the direct method of bias estimation using averaged gyroscope measurements in pre-defined identical static positions.

REFERENCES

1. Parusnikov N.A., Tikhomirov V.V., Trubnikov S.A. *Opreleniye instrumental'nykh pogreshnostey inertial'noy navigatsionnoy sistemy na nepodvizhnom osnovanii [In Russian]* – Fundamental'naya i prikladnaya matematika, Vol. 11, N. 7., P. 159 – 166, 2005.
2. Vavilova N.B, Vasineva I.A., Golovan A.A., Kozlov A.V., Papusha I.A., Parusnikov N.A. – The Calibration Problem In Inertial Navigation. – *Journal of Mathematical Sciences*, Vol. 253, N.6, P. 818-836, 2021
3. Dan Simon – *Optimal State Estimation: Kalman, H_∞ , and Nonlinear Approaches*. P. 123-124, 286-294

M. A. PONOMAREVA, A. V. KRAMLIKH
(Samara National Research University, Samara)

DETERMINATION OF THE SPACECRAFT ORIENTATION USING INSTANTANEOUS MEASUREMENTS

The paper presents a comparison of the most popular algorithms for determining the orientation of a spacecraft based on instantaneous measurements of various physical nature according to the following terms: the speed of algorithms, the accuracy and the type of output information.

Introduction. Information about the angular position of the spacecraft is used to link measurements carried out by the on-board equipment and in the spacecraft angular motion control system. There are many algorithms for determining the orientation of the spacecraft. In this paper, algorithms using instantaneous measurements are reviewed. They can determine orientation from two or more vector measurements obtained instantaneously (or with a negligible delay between measurements). Such algorithms are simple, do not require a priori information about the spacecraft position, have high speed, but low accuracy. The proposed report is devoted to the research and comparison of a number of the most commonly used instantaneous algorithms.

Mathematical formulation of the problem. The problem of determining the orientation of the spacecraft is to determine the angular position of the coordinate system (CS) associated with the spacecraft relative to some reference CS, for example, the orbital CS, based on available measurements in the associated CS and models of these measurements in the orbital CS. The angular position of the associated CS relative to the orbital CS is described by a rotation matrix \mathbf{M} , which can be parameterized by Euler angles or a quaternion [1].

The formula for the relationship of measurements and models of these measurements:

$$\mathbf{b}_i = \mathbf{M} \cdot \mathbf{r}_i, \quad (1)$$

where: \mathbf{b}_i – measurement vectors ($i = \overline{1, N}$, N – the number of unit measurement vectors in the associated CS); \mathbf{r}_i – measurement models vectors in the orbital CS; \mathbf{M} – rotation matrix.

Therefore, the problem is came down to finding the rotation matrix \mathbf{M} .

In this paper, the following algorithms for instantaneous measurements are researched: TRIAD [2-4], Optimized TRIAD [5], q-method [4,6,7], QUEST [3,4,7], ESOQ [4,7], ESOQ2 [4,7], SVD [4,7].

Results. To compare the algorithms, mathematical modeling was done in Matlab under the following conditions.

The orientation angles were set randomly and the true rotation matrix was calculated.

The elements of the vectors in the orbital CS were generated according to an equally probable law in the range of [-1000;1000]. Then the vectors were normalized, because the directions of these vectors and the angle between them are important, not their length.

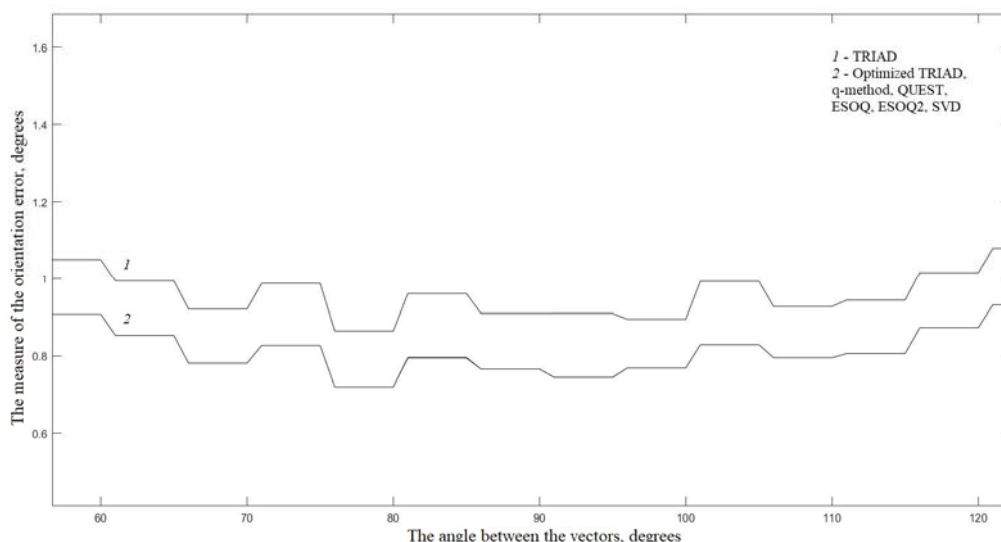
The vectors in the associated CS are calculated by formula (1) with the addition of Gaussian noise (the average value is zero, the value of the root mean square (RMS) was taken as 1% and 10% of the vector modulus). Then the vectors were normalized.

The measure of the error in determining the orientation of the spacecraft is found by the formula

$$\Phi = \arccos\left(\frac{1}{2}(tr(\mathbf{B}_{ou}) - 1)\right),$$

where $\mathbf{B}_{ou} = \mathbf{M} \cdot \mathbf{M}_1^T$, \mathbf{M} – true rotation matrix, \mathbf{M}_1 – found rotation matrix.

For each algorithm, the measure of the orientation error and the speed of operation for 10000 iterations were calculated. And the number of floating point operations was determined for one iteration of the algorithm.



The measure of the orientation error for RMS 1%

Table 1

Results

Algorithm	Speed*, s	Number of floating point operations **	Type of output information
TRIAD	0,053	11	Rotation matrix
Optimized TRIAD	0,169	42	Rotation matrix
q-method	0,241	59(900)***	Quaternion
QUEST	0,253	227	Quaternion
ESOQ	0,356	125	Quaternion
ESOQ2	0,152	79	Quaternion
SVD	0,175	53(650)***	Rotation matrix

* The running time of the algorithms is shown for computing 10,000 iterations.

** A function implemented in Matlab was used to calculate floating-point operations [8].

*** The q-Method and SVD algorithms use complex built-in functions for which it is impossible to determine the number of floating-point operations, so the values obtained in other papers are shown in table [7].

Conclusion. From results, it can be seen that the least accurate algorithm is TRIAD, other algorithms work with approximately the same accuracy. The fastest algorithms are TRIAD and ESOQ2, the slowest are ESOQ and QUEST. The algorithms with the fewest floating point operations are TRIAD and ESOQ2. According to the results of the comparison, TRIAD and ESOQ2 algorithms performed the best.

REFERENCES

1. Branets V.N., Shmyglevsky I.P. Application of quaternions in problems of orientation of a rigid body. Moscow: Nauka, 1973. 320 p.
2. Black H.D. A Passive System for Determining the Attitude of a Satellite. AIAA Journal. 1964. Vol. 2. №7. P. 1350-1351.
3. Shuster M.D., Oh S.D. Three-Axis Attitude Determination from Vector Observations. Journal of Guidance and Control. 1981. Vol. 4. №1, Jan.-Feb. P. 70-77.
4. Markley F.L., Crassidis J.L. Static Attitude Determination Methods. Fundamentals of Spacecraft Attitude Determination and Control. 2014. Chap.5. P. 183-233.
5. Bar-Itzhack Y.I., Harman R.R. Optimized TRIAD algorithm for attitude determination. Collection of Technical papers (A96-34712 09-12). 1996. P. 422-427.
6. Davenport P. A vector approach to the algebra of rotations with applications. NASA TN D-4696. 1968.
7. Markley F.L., D. Mortari. How to estimate attitude from vector observations. AAS 99-427, presented at the AAS/AIAA Astrodynamics Specialist Conference, Girdwood, Alaska. – 1999.
8. Qian, H. Counting the Floating Point Operations (FLOPS) [Электронный ресурс]. URL: <https://www.mathworks.com/matlabcentral/fileexchange/50608-counting-the-floating-point-operations-flops> (дата обращения 22.05.2024).

V.G. KARAULOV

(ITMO University, Concern CSRI Elektropribor, JSC, Saint Petersburg),

A.M. GRUZLIKOV, M. D. KORABLEVA

(Concern CSRI Elektropribor, JSC, Saint Petersburg)

SOLVING THE PROBLEM OF RELATIVE NAVIGATION USING DEEP NEURAL NETWORKS

The problem of relative navigation of an underwater vehicle (UV) for bringing it to a bottom station (BS) is considered. Within the deterministic approach, the statement of the corresponding problem of estimating the UV relative coordinates and orientation angles is presented. The stated problem is solved using the least squares method. To reduce the a priori knowledge uncertainty of the coordinates and orientation angles, it is proposed to use the architecture of deep neural networks. Based on the performed simulation, the root-mean-square errors (RMSE) of estimating the UV relative coordinates and orientation angles are compared using various methods of training fully connected neural networks.

Introduction. The paper deals with the problem of determining the coordinates and orientation angles of an underwater vehicle (UV) for solving the problem of bringing it to the bottom station (BS).

The hydroacoustic system of the UV (Fig. 1) includes receiving antennas located under the vehicle keel in the stern and bow parts, and emitters installed at the edges of the base and performing non-directional emission of a signal. It should be noted that the emitted signals are tone signals of the same frequency, the emission of which is spaced in time so that the source of the emission could be uniquely identified by the signal detection period.

The proposed paper continues the authors' works [3-5]. The purpose of the paper is to rectify the drawback associated with the great expenditure of computer memory resources. This is due to the fact that it is necessary to store a large amount of data in the form of a kd-tree used in the K-nearest neighbors method. The present paper is aimed at correcting this problem by using a deep neural network.

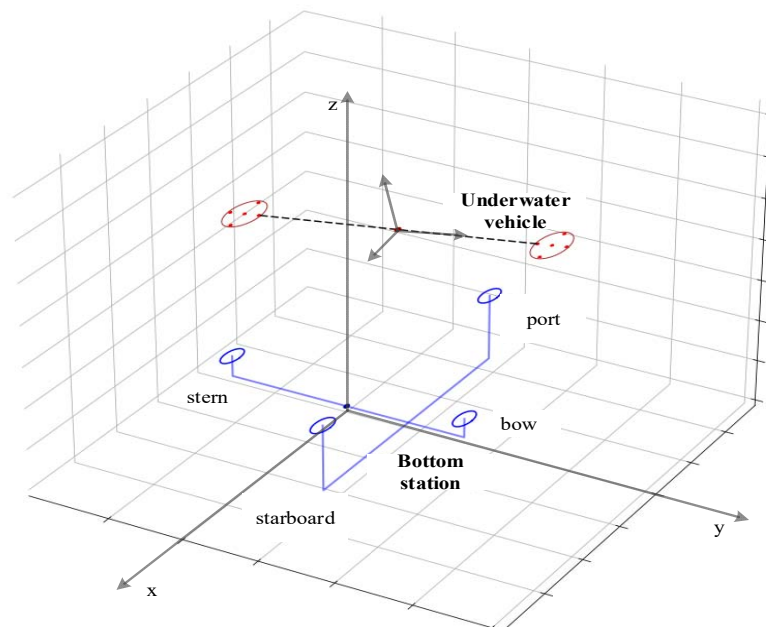


Fig. 1. Layout of UV and BS hydroacoustic system

Statement of deterministic problem of estimation. Onboard the UV, there is a group of n hydrophones operating on a single time scale and located in the bow and stern parts. Besides, the BS has m sonar beacons located at the edges (Fig. 1). The beacons emit a tone signal in accordance with the known emission cyclogram, and it is worth noting that the time scales of the UV and the BS do not match.

We will follow the article [2] and record the measurements of pseudoranges between beacons and hydrophones, which are generated by the UV:

$$y_j^i = \hat{c}_0 T_j^i = d_j^i + \delta + v_j^i + \Delta c T_j^i, j = \overline{1, n}, i = \overline{1, m}, \quad (1)$$

where i is the beacon number, j is the hydrophone number, d_j^i are the range true values, v_j^i are the interference, δ is the pseudorange measurement error due to the time scale discrepancy (a pseudorandom variable), T_j^i are the measured values of the time of signal arrival from the beacons to the hydrophones, \hat{c}_0 is the a priori estimate of the sound speed in the water, Δc is the error of the speed of sound propagation in the water. The interference v_j^i are mutually uncorrelated centered normally distributed random variables with standard deviations σ_j^i . We know the coordinates $x^i, y^i, z^i, i = \overline{1, m}$ of the beacons in the BS-fixed rectangular axes x, y, z , as well as the coordinates $\tilde{x}_j, \tilde{y}_j, \tilde{z}_j, j = \overline{1, n}$ of the hydrophones in the UV-fixed rectangular axes $\tilde{x}, \tilde{y}, \tilde{z}$. Orientation of the UV relative to the BS-fixed coordinate frame will be determined using the heading angles K , trim ψ and roll θ . The center of the UV-fixed coordinate frame is its control point, i.e. the coordinates of the control point in this coordinate frame are $\tilde{x}_0 = \tilde{y}_0 = \tilde{z}_0 = 0$, and in BS-fixed coordinate frame – x_0, y_0, z_0 . The a priori information about $x_0, y_0, z_0, K, \psi, \theta, \delta$ is not available.

Let us introduce the designations: $s^i = (x^i, y^i, z^i), i = \overline{1, m}$ – for beacon coordinate vectors in the BS-fixed coordinate frame; $\tilde{p}_j = (\tilde{x}_j, \tilde{y}_j, \tilde{z}_j), j = \overline{1, n}$ – for hydrophone coordinate vectors in the UV-fixed coordinate frame; $p_j = (x_j, y_j, z_j), j = \overline{0, n}$ – for coordinate vectors of the control point and hydrophones in the BS-fixed coordinate frame; $A(K, \psi, \theta)$ – for the matrix of transition [1] from axes $\tilde{x}, \tilde{y}, \tilde{z}$ to axes x, y, z . Note that $p_0 = (x_0, y_0, z_0)$.

Following the article [2], we can write down the formulas for ranges being measured:

$$d_j^i = |p_j - s^i| = |p_0 + A(K, \psi, \theta) \tilde{p}_j - s^i|. \quad (2)$$

Using measurements (1) and taking into account (2), it is necessary to estimate the vector p_0 of the UV control point coordinates in the BS-fixed coordinate frame, and the angles K, ψ, θ of the UV orientation relative to this coordinate system, as well as the error in measuring pseudoranges δ and the error of the speed of sound propagation in the water Δc .

Fully connected neural network. It is proposed to use a fully connected architecture of a deep neural network to reduce the area of expected knowledge uncertainty of relative coordinates and orientation angles for the first approximation when solving the estimation problem. The feedforward network will be trained on a data set that is formed on the basis of a geometric model – the preset position of the beacons of an underwater base station and the coordinates of UV receiving elements on a specified coordinate grid and orientation angles table. The training sample is formed according to the following rule:

Let the training sample be formed according to the following rule:

- $(t_a^j - t_b^j)_{j \in \overline{1, 4}}$ – the difference in the time of signal reception between the pairs of maximally spaced receivers (a, b) with the fixed beacon;
- $(t_i^a - t_i^b - T^{a,b})_{i \in \overline{1, 10}}$ – the difference in the time of signal reception between the pairs of beacons (a, b) by the fixed receivers and the shift in the time of signal emission by the beacons (with the fixed value $T^{a,b}$).

Thus, the input layer will consist of 100 neurons, the output layer – of 6 neurons. After each hidden layer, the ReLU (Rectified Linear Unit) activation function is applied, and after the last one the activation function is not available.

Simulation modeling and obtained results. Simulation modeling of the UV motion down to the BS from the point $(0, 0, 50)$ m was carried out with clockwise rotation about the vertical axis of the

UV and with zero angles of roll and pitch. Based on the modeling results, estimates of the root-mean-square errors (RMSE) of the UV coordinates and heading angle were obtained with the help of fully connected neural network architectures using various methods of their training (see Table 1).

Table 1

Comparison of RMSE of coordinates and heading angle estimates for 5 models with different training methods

		RMSE X, m	RMSE Y, m	RMSE Z, m	RMSE K, °
Model 1 (5x100)	Without BN, L2 = 0	1.21	1.36	4.61	4.7
	With BN, L2 = 0	1.39	1.67	5.45	4.78
	With BN, L2 = 0.001	0.85	1.48	6.84	5.2
	With BN, L2 = 0.01	0.8	1.27	6.2	5.09
	With BN, L2 = 0.1	1.07	1.02	20.5	5.45
Model 2 (10x100)	Without BN, L2 = 0	1.61	2.09	4.78	4.55
	With BN, L2 = 0	1.97	1.14	5.18	5.05
	With BN, L2 = 0.001	1.88	0.91	4.94	4.39
	With BN, L2 = 0.01	1.82	1.8	5.78	5.07
	With BN, L2 = 0.1	0.7	0.61	14.43	5.85
Model 3 (15x100)	Without BN, L2 = 0	1.4	1.84	3.65	4.67
	With BN, L2 = 0	1.59	1.34	5.98	4.99
	With BN, L2 = 0.001	3.34	1.64	4.52	4.89
	With BN, L2 = 0.01	3.99	3.54	5.69	4.85
	With BN, L2 = 0.1	-	-	-	-
Model 4 (100-500-250-50)	Without BN, L2 = 0	1.75	0.99	4.54	3.89
	With BN, L2 = 0	1.68	2.21	5.21	4.55
	With BN, L2 = 0.001	1.35	2.3	6.41	4.57
	With BN, L2 = 0.01	2.76	2.5	7.93	5.27
	With BN, L2 = 0.1	0.52	0.7	18.85	5.62
Model 5 (500-1000-3000-6000-4000-1000-500-250-100)	Without BN, L2 = 0	1.66	1.73	4.36	4.9
	With BN, L2 = 0	1.35	1.03	4.98	4.62
	With BN, L2 = 0.001	0.46	2.56	5.9	4.59
	With BN, L2 = 0.01	1.07	0.82	5.09	5.5
	With BN, L2 = 0.1	-	-	-	-

The following configurations of fully connected neural networks were analyzed: with batch normalization (BN), with L2 regularization (the table shows the values of the regularization parameter), and 5 network structures, where the first three models have all hidden layers with 100 neurons, and the 4th and 5th models have the structure given in brackets (the number of neurons in each hidden layer is written with a hyphen).

The results show that the use of regularization worsens the prediction accuracy, while the 4th and 5th models with a regularization parameter of 0.1 could not learn at all. The use of BN also did not improve the model. As a result, the best accuracy was shown by Model 4, without L2 regularization and BN. Estimates for the roll and pitch angles are not presented, because each model has estimated them with a RMSE of no more than 0.01 degrees.

Conclusion. The paper formulates the problem of estimating the relative coordinates and determining the orientation angles of the UV based on signals from hydroacoustic beacons within the deterministic approach. The authors show the possibility of using a deep neural network in solving this problem at the first stage of narrowing the area of a priori knowledge uncertainty of the relative coordinates and orientation angles.

This work was supported by the Russian Science Foundation, project no. 23-19-00626, <https://rscf.ru/project/23-19-00626/>.

REFERENCES

1. **Emel'yantsev, G.I. and Stepanov, A.P.**, *Integrirovannye inertial'no-sputnikovye sistemy orientatsii i navigatsii* (Integrated INS/GNSS Systems of Orientation and Navigation), St. Petersburg: Concern CSRI Elektropribor, 2016.
2. **Koshaev, D.A.**, AUV relative position and attitude determination using acoustic beacons, *Gyroscopy and Navigation*, 2022, vol. 13, pp. 262–275.
3. **Gruzlikov, A.M.**, Short and ultra-short baseline navigation of the AUV for bringing it to the bottom docking device, *Proceedings of the 29th Saint Petersburg International Conference on Integrated Navigation Systems (ICINS)*, 2022, pp. 1–3.
4. **Gruzlikov, A.M., Karaulov, V.G., Mukhin, D.A., and Shalaev, N.A.**, Results of testing the positioning algorithm and determining the orientation of the underwater vehicle based on data from hydro-acoustic beacons, *Izvestiya YuFu. Tekhnicheskie nauki*, 2023, no. 1, pp. 265-275.
5. **Karaulov, V.G., Gruzlikov, A.M., and Zolotarevich, V.P.** Recursive algorithm for AUV positioning and determining its orientation, *Proceedings of the 30th Saint Petersburg International Conference on Integrated Navigation Systems (ICINS)*, 2023, pp. 1-4.

O. A. STEPANOV, Yu. A. LITVINENKO, A. M. ISAEV
(Concern CSRI Elektropribor, ITMO University, St. Petersburg, Russia)

RECURSIVE ITERATIVE BATCH LINEARIZED SMOOTHER FOR NAVIGATION ESTIMATION PROBLEMS

A recursive iterative batch linearized smoother is described for the general case of solving nonlinear problems with nonlinearities both in the equations for the shaping filter and measurement equations. The efficiency of its application is analyzed by the example of solving practical navigation estimation problems.

Algorithms intended to solve nonlinear problems of navigation information processing are in most cases designed within the framework of the Bayesian stochastic approach [1-9], which is due to the need to obtain not only an estimate of the vector of unknown parameters, but also the corresponding calculated accuracy characteristic. In fact, in this case, the solution of the filtering problem is aimed to find a certain set of parameters describing the type of the posterior probability density function (PDF). Usually, the mathematical expectation calculated with the help of this set is used as an estimate at the algorithm output, and the root-mean-square error of the estimate, as an accuracy characteristic. If the calculated and actual values are consistent, the algorithm is called consistent [10-12].

One of the main requirements for the algorithms intended to solve problems in real time is low computational complexity, which makes it possible not to impose significant requirements when they are implemented in an onboard computer. In this regard, filtering algorithms are often designed using a recursive scheme, which implies sequential processing of measurements, one after another, and it is important that after the measurement was processed at the current step, it is no longer used. In so doing, it is necessary to keep the set of parameters, describing the type of the posterior PDF, from step to step.

Recursive Kalman-type algorithms (KTA), in which the posterior PDF is replaced at each step by its Gaussian approximation, are the most widespread in solving practical problems. Such replacement provides easy implementation of a computationally simple recursive algorithm since, from step to step, it is sufficient to keep only two parameters – the mathematical expectation and the covariance matrix of estimation errors, which fully describe the Gaussian approximation of the PDF. In many cases, when the form of the posterior PDF is close to the Gaussian one, KTAs prove to be consistent and allow obtaining an accuracy estimate close to the optimal one in the RMS sense [3-8]. However, when the form of the posterior PDF is substantially different from the normal one, the errors caused by its approximation will be significant. Due to the recursive nature of the algorithm, these errors will accumulate, which may eventually lead to its inoperability.

To solve such problems, the type of the posterior PDF in the filtering algorithm being designed can be described with the use of a significant set of parameters that retains its complex form, and the recursive nature of the algorithm can be organized based on the known recursive relation [6, 13-18]. A weighted set of delta functions can serve as a set of parameters. However, the algorithms designed in this way mostly turn out to be computationally complicated and difficult to implement in onboard computers, which makes them unsuitable for real-time problems.

There are some problems in which the posterior density, being multiextremal at initial moments of time, takes a single-extremal form close to the Gaussian one in the process of its evolution. Obviously, recursive KTAs will be inoperative for their solution. However, as was shown in [6,19-23], nonrecursive KTAs can provide the accuracy of optimal estimation and be consistent, starting from the moment when the posterior PDF becomes close to the Gaussian one. The input of such algorithms is a batch of all measurements accumulated by the current moment of time, which is why they are usually called batch algorithms [21-23]. For all their advantages, their computational load remains rather high, which is primarily due to the need to invert high-dimensional matrices.

To overcome this drawback, in [23], the authors propose an algorithm called the recursive iterative batch linearized smoother, hereinafter referred to as "Smoother". It is essentially a nonrecursive algorithm, but at the same time, it has the advantage of the algorithms constructed with

the use of the recursive scheme, namely, low computational load. This is made possible due to the recursive procedure, which is used, instead of inverting a high-dimensional matrix at each iteration, to find the necessary estimates by solving a smoothing problem. Paper [23] gives only a brief description of such an algorithm, without its formula dependencies and without going into the details of its implementation.

The aim of the paper is to describe in detail the proposed smoother for the general case of the problem whose statement is formulated within the framework of the Bayesian stochastic approach and nonlinearities are contained both in the dynamic equations and equations of measurements. The advantages of the smoother are demonstrated by solving practical problems of navigation information processing.

This work was supported by the grant from the Russian Science Foundation, project no. 23-19-00626,

<https://rscf.ru/project/23-19-00626/>.

REFERENCES

1. Kalman, R.E., A new approach to linear filtering and prediction problems, *Trans. ASME. Series D, J. Basic Engineering*, 82, 1960, pp. 35-45.
2. Stratonovich, R.L., Conditional Markov processes, in *Teoriya veroyatnostei i eyo prilozheniya* (Probability Theory and its Applications), 1960, vol. 5, no. 2, pp. 172-195.
3. Jazwinski, A.H., *Stochastic Process and Filtering Theory*, New York: Academic Press, 1970.
4. Gelb, A., *Applied Optimal Estimation*, M.I.T. Press, Cambridge, 1974.
5. Dmitriev, S.P., *Vysokotochnaya morskaya navigatsiya* (High-accuracy Marine Navigation). St.Peterburg: Sudostroyeniye, 1991.
6. Stepanov, O.A., *Primenenie teorii nelineinoy fil'tratsii v zadachakh obrabotki navigatsionnoi informatsii* (Application of Nonlinear Filtering Theory for Navigation Data Processing), 3rd edn., St. Petersburg: Elektropribor, 2003.
7. Simon D. *Optimal State Estimation: Kalman H_∞ and Nonlinear Approaches*, New Jersey, NJ: John Wiley & Sons, Inc., 2006.
8. Särkkä S., *Bayesian Filtering and Smoothing*, Cambridge University Press, 2013.
9. Stepanov, O.A., *Osnovy teorii otsenivaniya s prilozheniyami k zadacham obrabotki navigatsionnoi informatsii* (Fundamentals of the Estimation Theory with Applications to the Problems of Navigation Information Processing), 3rd edn., revised and supplemented, Part 1, *Vvedenie v teoriyu fil'tratsii* (Introduction to the Filtering Theory), St. Petersburg: TsNII Elektropribor, 2017.
10. Bar-Shalom Y., Li, X., and Kirubarajan, T., *Estimation with Applications to Tracking and Navigation*, New York, Wiley-Interscience, 2001.
11. Bolotin, Yu.V., Bragin, A.V., and Gulevskii, D.V., Studying the consistency of the extended Kalman filter in the problem of pedestrian navigation with an SINS fixed on his feet, *Giroskopiya i Navigatsiya*, 2021, vol. 29, no. 2 (113), pp. 59-77.
12. Stepanov, O.A. and Isaev, A.M., Methodology of comparative analysis of recursive nonlinear filtering algorithms in problems of navigation information processing based on predictive simulation, *Giroskopiya i Navigatsiya*, 2023, vol. 31, no. 3 (122), pp. 48-65. EDN: MVWKGK
13. Busy, R.S., *Nonlinear filtering theory*, *IEEE Trans on Automatic Control*, 1965
14. Doucet, A., Freitas, N. De., and Gordon, N., *Sequential Monte Carlo Methods in Practice*, New York, NY, USA: Springer-Verlag, 2001.
15. Chen, Z., *Bayesian Filtering: From Kalman Filters to Particle Filters, and Beyond*. Adaptive Systems Laboratory Technical Report, McMaster University, 2003, Hamilton.
16. Sarkka, S., Vehtari, A., and Lampinen, J. Rao-Blackwellized particle filter for multiple target tracking, *Information Fusion*, 2007, vol. 8 (1), pp. 2-15
17. Stepanov O.A. and Toropov A.B., Application of sequential Monte Carlo methods using analytical integration procedures in processing navigation information, *XII Vserossiiskaya soveshanie po problemam upravleniya VSPU-2014* (XII All-Russian Conference on Control

- Problems VSPU-2014, V.A. Trapeznikov Institute of Control Sciences of Russian Academy of Sciences, Moscow, Russia, 2014, pp. 3324-3337.
18. Stepanov O.A. and Toropov A.B. Primeneniye posledovatel'nykh metodov Monte-Karlo s ispol'zovaniyem protsedur analiticheskogo integrirvaniya pri obrabotke navigatsionnoy informatsii. *XII Vserossiyskoye soveshchaniye po problemam upravleniya VSPU-2014*. Institut problem upravleniya im. V.A. Trapeznikova ran. 2014. S. 3324-3337.
 19. Dunik, J., Straka, O., Matousek, J., and Brandner, M., Accurate Density-Weighted Convolution for Point-Mass Filter and Predictor. Accepted for IEEE Transactions on Aerospace and Electronic Systems, 2021
 20. Vasiliev V.A., Litvinenko Y.A., Stepanov O.A., Toropov A.B. Sravneniye rekurrentnykh i nerekurrentnykh algoritmov fil'tratsii pri reshenii zadachi navigatsii po geofizicheskim polyam // V sbornike: *XIV Vserossiyskaya mul'tikonferentsiya po problemam upravleniya MKPU-2021*. materialy XIV mul'tikonferentsii: v 4 t. Rostov-na-Donu, 2021. P. 125-127.
 21. O.A. Stepanov, A.M. Isaev, Y.A. Litvinenko Sravneniye rekurrentnykh i nerekurrentnykh skhem postroyeniya algoritmov, osnovannykh na linearizatsii, pri reshenii odnogo klassa zadach nelineynogo otsenivaniya // *Trudy XIV Vserossiyskogo soveshchaniya po problemam upravleniya*. M.: Institut problem upravleniya imeni V.A. Trapeznikova RAN, 2024
 22. O.A. Stepanov, Y.A. Litvinenko, A.M. Isaev Iterative Batch Linearized Smoother for the AUV Collaborative Navigation. *Materialy XXXI Mezhdunarodnoy nauchno-tekhnicheskoy konferentsii «Sovremennyye tekhnologii v zadachakh upravleniya, avtomatiki i obrabotki informatsii»* P. 117, 2024.
 23. Stepanov, O.A., Litvinenko, Y.A., and Isaev, A.M., Comparison of recursive and nonrecursive linearization-based algorithms for one class of nonlinear estimation problems. *10th International Conference on Control, Decision and Information Technologies (CoDIT)*, 2024 (in press).
 24. Stepanov, O.A., Zolotarevich V.P., Litvinenko Y.A., Isaev A.M., Motorin A.V. Recursive and Nonrecursive Algorithms Applied to Navigation Data Processing: Differences and Interrelation with Factor Graph Optimization Algorithms // 31st Saint Petersburg International conference on Integrated Navigation Systems, 2024.
 25. Stepanov O. A., Litvinenko Yu. A., Isaev A. M. Comparative Analysis of Quasi-Linear Kalman-Type Algorithms in Estimating a Markov Sequence with Nonlinearities in the System and Measurement Equations, *Mekhatronika, Avtomatizatsiya, Upravlenie*, 2024, vol. 25, no. 11, pp. 585—595 (in Russian).

V.A. BOLOTINA, D.P. AVARIASKIN
(Samara National Research University, Samara)

STUDY OF THE INFLUENCE OF THE MOON ON THE INSPECTION MOTION OF SPACECRAFTS IN HIGH ORBITS

In this work, initial conditions are used to ensure inspection motion, providing closed relative trajectories with unperturbed motion. Taking into account the influence of perturbation in the form of the gravitational field of the Moon leads to the evolution of the relative trajectory, and it ceases to be closed. A study of the evolution of the inspection trajectory under the influence of the gravitational field of the Moon is conducted.

Introduction. To solve scientific and applied problems in space, the technology of group flight is used, one of the types of which is the inspection motion of spacecraft (SC). Inspection motion is used for the inspection object (hereinafter referred to as the reference SC) to fly around the inspector in order to obtain the necessary information, inspection and diagnostics without direct contact [1]. The inspector can also approach space debris for its inspection or removal from orbit.

The main issue in the inspection problem is the choice of the initial conditions of the group flight. In the case of unperturbed motion, the initial conditions that ensure a closed relative trajectory are found from the condition of equality of the orbital energies of the reference SC and the inspector. However, under the influence of various disturbances, the trajectory ceases to be closed, which leads to the destruction of the inspection motion.

This work is devoted to the study of the influence of the gravitational field of the Moon on the formation of the inspection motion of spacecraft in high orbits. That is, a study was conducted of various initial conditions of motion of the inspector and the reference spacecraft, under which the deviation of the relative trajectory from the nominal (undisturbed) under the influence of the gravitational field of the Moon would be minimal.

Mathematical modeling of relative motion. In this paper, we will consider the influence of the Moon's gravitational field on inspection motion in the case when the reference SC moves along a geostationary orbit and the Molniya orbit. Inspection motion is provided in the plane of the orbits under consideration. Closed relative trajectories used to provide inspection of one SC by another can be obtained by selecting the initial conditions of the inspector's motion. In this case, the initial conditions must be selected so that the condition for the formation of a closed relative trajectory is met: the periods of revolution of each SC along its orbit around the attracting center must be equal:

$$T_{ref} = T_i, \quad (1)$$

where: T_{ref} , T_i – the periods of revolution of the reference spacecraft and the inspector, respectively, in their orbits.

Let us introduce two coordinate systems: the absolute geocentric coordinate system (ACS) and the orbital barycentric coordinate system (OCS). Let us consider the disturbed motion of two spacecraft – the reference and the inspector. The center of mass of the reference spacecraft is the origin of the OCS. The model of the motion of the reference spacecraft and the inspector in the ACS, taking into account the influence of the gravitational field of the Moon, are written, respectively, in the form

$$\ddot{\vec{r}}_{0n} + \frac{\mu}{r_{0n}^3} \vec{r}_{0n} = \vec{f}_L, \quad \ddot{\vec{r}}_n + \frac{\mu}{r_n^3} \vec{r}_n = \vec{f}_L, \quad (2)$$

where $\ddot{\vec{r}}_{0n}$ – acceleration of the reference spacecraft; $\mu = 398602 \text{ km}^3/\text{s}^2$ – gravitational parameter of the Earth; \vec{r}_{0n} – radius vector of the reference spacecraft; \vec{f}_L – disturbing acceleration caused by the attraction of the Moon; $\ddot{\vec{r}}_n$ – acceleration of the inspector; \vec{r}_{0n} – inspector radius vector.

The initial conditions of the inspector's motion are determined from the expression for the relationship between the ACS and the OCS:

$$V_n^2 = (v_{x0} + V_{n0n} + \omega_{0n}y_0)^2 + (v_{y0} + V_{r0n} - \omega_{0n}x_0)^2, \quad (3)$$

where ω_{on} – angular orbital velocity of the reference spacecraft; V_{non}, V_{ron} – normal and radial projections of the reference spacecraft velocity; $v_{y0} = \frac{\omega_{on} x_0}{2}$ – inspector initial velocity component [2], $V_H = \sqrt{\frac{2\mu}{r_H} - \frac{\mu}{a_{on}}}$ – initial speed of the inspector in the OCS, $r_H = \sqrt{X_H^2 + Y_H^2 + Z_H^2}$ – the value of the radius vector of the inspector. In this case, the fulfillment of (1) is ensured by choosing such a velocity of the inspector that the major semi-axes of the orbits of the inspector and the reference spacecraft are equal. Then the relative trajectory will be closed. This is true only for the case of unperturbed motion. Due to the fact that within the framework of this work the influence of the gravitational field of the Moon is taken into account, the real trajectory will not be closed. Therefore, a parameter is introduced that will be used to estimate the influence of this perturbation. The maximum deviation of the inspection perturbed trajectory from the unperturbed relative trajectory Δr_{max} under the same initial conditions of motion is taken as the evaluation parameter:

$$\Delta r_{max} = r_{maxB} - r_{maxH}, \tag{4}$$

where r_{maxB} – maximum distance between the reference spacecraft and the inspector on the disturbed trajectory, m; r_{maxH} – maximum distance between the reference spacecraft and the inspector on an undisturbed trajectory, m.

Using (4), the maximum deviations of the inspection perturbed from the unperturbed relative trajectory were found. The influence of the initial position of the Moon and the reference spacecraft on the inspection motion of the spacecraft was studied. The maximum influence of the Moon occurs at the arguments of the Moon's latitude from 75 to 125 degrees and from 260 to 320 degrees and at the arguments of the reference spacecraft's latitude from -40 to 20 degrees in the Molniya-type orbit.

A study was also conducted on the influence of the initial position of the inspector on the formation of the inspection motion, taking into account the influence of the Moon. The initial position was set by the angle α , measured from the Ox axis of the OSC to the current position of the inspector. The study showed that the influence of the Moon on the inspection motion is maximum in the case when the reference spacecraft and the inspector are on the same radius vector. Based on the simulation results, a graph was constructed reflecting the dependence of the maximum influence of the Moon on the initial positions of the inspector (Fig. 1).

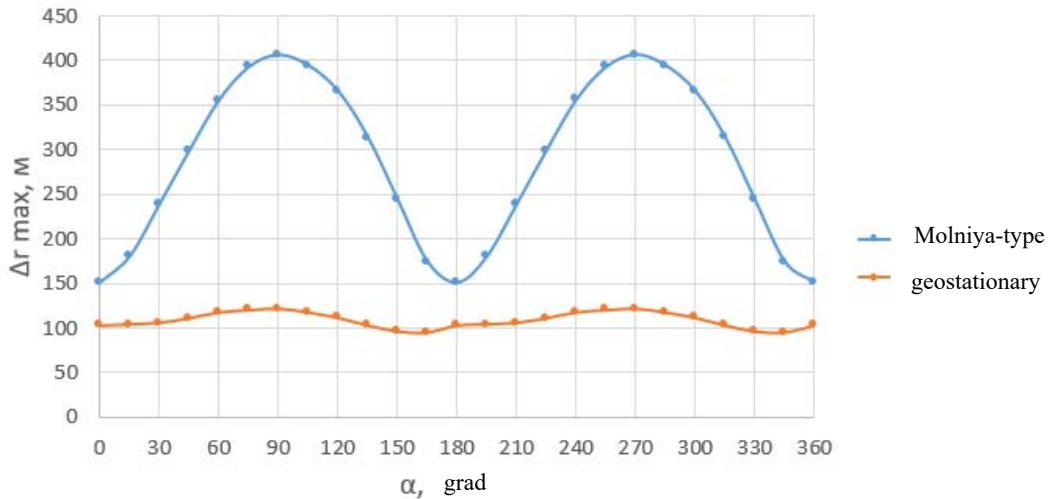


Fig. 1. Maximum influence of the Moon depending on the initial position of the inspector

Conclusion. A study of the influence of the Moon's gravitational field on the formation of inspection motion of spacecraft in high orbits was conducted. Ranges of arguments of latitude of the Moon and the reference spacecraft were obtained for which the influence of the Moon is maximum. A study of the influence of the Moon's gravitational field on the formation of inspection motion depending on the position of the inspector relative to the reference spacecraft showed that it is maximum when both spacecraft are on the same radius vector. There are no pronounced maxima on the inspection trajectory when moving along a geostationary orbit.

REFERENCES

1. **Scherbakov M. S., Medvedev S. A.** Study of the possibility of using osculating elements of relative motion in the inspection task // *Mathematical modeling, computer and natural experiment in natural sciences*. 2022. No. 4
2. **Scherbakov M. S., Avariaskin D. P.** Studying problems on choosing stable orbits of nanosatellites to provide passive and periodic relative trajectories // *Journal of Physics: Conference Series*. – 2020. – Vol. 1536, №1. – 8 p.

A. R. BRAZHENKO
(St. Petersburg Federal Research Center of the RAS, Saint Petersburg)

A. O. KOMAROV
(NNSTU n.a. R.E. Alekseev, Nizhny Novgorod)

ALGORITHM FOR LOCALIZATION AND DIRECTION DETERMINATION OF THREAT IMPACT USING VISION LANGUAGE MODELS IN AUTONOMOUS TRANSPORT SYSTEMS

An algorithm is proposed for the localization and analysis of threat directions in autonomous transport systems using Vision-Language Models (VLM). The application of VLM enables more accurate identification of the behavior and trajectories of objects in complex scenarios, including dynamic urban conditions and unpredictable environmental changes.

Introduction. Modern autonomous transport technologies face challenges related to safe navigation in real-world conditions, where the risk of hazardous events significantly increases. Existing systems[1], [2] often employ classical image analysis algorithms, which do not always effectively solve problems in complex scenarios. In recent years, methods utilizing deep learning for threat detection have been actively developed, including transformer-based approaches[3] that take contextual aspects into account. However, these methods are limited under real-world conditions, such as the presence of overlapping objects or complex interactions between objects. The proposed algorithm, based on Vision-Language Models (VLM), enhances localization efficiency[4] through the integration of visual and textual information, allowing for more accurate consideration of the dynamics and environmental changes.

Statement of the problem. This work addresses the task of creating an algorithm capable of localizing objects that pose a threat to the movement of unmanned ground transport and determining their direction based on images obtained from cameras. The algorithm must take into account not only the visual characteristics of the objects but also their behavioral models, which will help more accurately predict their movement. The key aspects of the task include:

1. The use of Vision-Language Models for generating textual descriptions of a scene based on images, which allows for obtaining contextual information about what is happening.
2. Localization and tracking of threatening objects in the frame based on the description obtained using VLM, including both static and dynamic elements.
3. Analysis of the behavior of objects and their trajectories to assess potential threats to the unmanned vehicle.

Algorithm for localization and direction determination of threat impact. The algorithm consists of the following steps:

1. Transmission of the image to the Vision-Language Model (VLM) [5].
2. Generation of a textual description of the scene, bounding boxes, and threat probabilities.
3. Extraction of keypoints of the object.
4. Determination of direction and visualization of object movement.

The algorithm receives an image I from the vehicle's camera, which is passed to the Vision-Language Model based on the attention mechanism[6] and the Kosmos-2 architecture[7], fine-tuned on specialized contextual tasks using the LoRA adapter[8]. A linear layer with a sigmoid activation function was added to the model's architecture for binary classification, predicting the probability of an object belonging to the classes "threat" or "non-threat."

The LoRA adapter adds learnable low-dimensional matrices to the model architecture for adaptive fine-tuning. The input image I is processed by the base model f and then fed into LoRA using the following operations:

Scientific Supervisor: Ph.D., Dc.Sci., Prof., Director of St. Petersburg Institute for Informatics and Automation of RAS (SPIIRAS), Vasily Yuryevich Osipov.

$$\mathbf{W}_{\text{LoRA}} = \mathbf{W} + \alpha \cdot \mathbf{A} \cdot \mathbf{B},$$

where \mathbf{W} — the original weights of the base model, \mathbf{A} и \mathbf{B} — low-dimensional matrices (LoRA adapters) initialized with random values and optimized during training, and α — a scaling factor that regulates the contribution of the adapter. The scaling factor $\alpha = 8$ was empirically chosen for an optimal balance between the performance of the base model and the improvement in adaptation provided by LoRA.

For the binary threat classification task, a loss function based on binary cross-entropy is used, which is optimized to minimize classification error. An additional regularization term is added, considering the specificity of the data and aimed at reducing false positives for the "no threat" class. The loss function is given by the following formula:

$$\mathcal{L} = -\frac{1}{N} \sum_{i=1}^N [y_i \cdot \log(\hat{y}_i) + (1 - y_i) \cdot \log(1 - \hat{y}_i)] + \lambda \cdot R(W_{\text{LoRA}}),$$

where N — the number of samples, y_i — the true class label for the i -th sample ($y_i = 1$ for threat, $y_i = 0$ for "no threat"), \hat{y}_i — the predicted probability of belonging to the threat class for the i -th sample, λ — the regularization coefficient, $R(W_{\text{LoRA}})$ — the regularization term that depends on the LoRA weights. The regularization coefficient λ , which varied from 0.01 to 1.0 in the experiments, was chosen to be 0.1, providing a balance between reducing false positives and maintaining threat classification accuracy.

The model generates a textual description of the scene, identifying objects and determining their coordinates as bounding boxes. Using the contextual task P , the model produces the following output:

$$\text{VLM}: \{I, P\} \rightarrow \{D, B, C\},$$

where D — the textual description of the scene, a B — the set of bounding boxes that define the positions of identified objects in the image, $C = \{c_1, c_2, \dots, c_n\}$ — represents the probabilities of objects belonging to the "threat" class. From the generated textual description, entities, their coordinates, and threat classification are extracted, providing structured information about the scene.

To determine the direction of movement of objects (in this research, pedestrians), a vector is calculated based on the coordinates of key body points obtained using the MediaPipe Pose model [9]:

- If previous frames are available, the coordinates of the key points are compared frame by frame:

$$\begin{aligned} \Delta x &= x_t - x_{t-1} \\ \Delta y &= y_t - y_{t-1} \end{aligned}$$

where (x_t, y_t) — the coordinates of the key points in the current frame, a (x_{t-1}, y_{t-1}) — the coordinates of the key points in the previous frame. Based on these changes, the direction vector is calculated as

$$\text{Direction} = \text{atan2}(\Delta y, \Delta x)$$

- If previous frames are not available, the direction is determined solely by the coordinates of the feet and the head. The following formula is used:

$$\text{Direction} = \begin{cases} \text{right}, & \text{if } \text{head_right} \wedge \text{left_foot_right} \wedge \text{right_foot_right} \\ \text{left}, & \text{if } \text{head_right} \wedge \neg \text{foot_right} \wedge \neg \text{right_foot_right} \\ \text{forward}, & \text{otherwise} \end{cases},$$

where head_right is determined by the position of the head relative to the center of the shoulders, left_foot_right and right_foot_right are determined by the position of the feet relative to the heels. This allows the system to accurately classify the direction of movement of objects even in the absence of information from previous frames.

After calculating the direction vector for each object, the movement direction is visualized by displaying a vector on the image from the geometric center of the object to the endpoint calculated based on the direction. The direction vector V is defined as:

$$V = (x_{\text{end}} - x_{\text{center}}, y_{\text{end}} - y_{\text{center}}),$$

where $(x_{\text{center}}, y_{\text{center}})$ — the coordinates of the geometric center of the object, $(x_{\text{end}}, y_{\text{end}})$ — the coordinates of the endpoint calculated based on the object's direction of movement.

Example of algorithm performance. The input to the algorithm is an image where an object (pedestrian) is crossing the street.

Output from the Vision-Language Model (VLM):

Scene Context: An image of a woman crossing the street while talking on her phone.

Objects:

('a woman', (12, 19), [(0.578125, 0.296875, 0.890625, 0.984375)], {'threat': 0.9, 'no_threat': 0.1}),

('the street', (29, 39), [(0.015625, 0.203125, 0.984375, 0.984375)], {'threat': 0.05, 'no_threat': 0.95}),

('her phone', (57, 66), [(0.640625, 0.421875, 0.671875, 0.484375)], {'threat': 0.3, 'no_threat': 0.7}).

For classifying objects as "threats," a probability threshold of 0.5 is used: if the probability exceeds 0.5, the object is classified as a threat. In this case, "a woman" with a probability of 0.9 is classified as a "threat," while "the street" and "her phone" (with probabilities of 0.05 and 0.3, respectively) are classified as "non-threats."

For threats, a movement direction vector is calculated. In the output image (Figure 1), the keypoints of the object (pedestrian) are highlighted, and an arrow indicates the direction of movement.



Figure 1. Example of algorithm performance

The algorithm was trained using 1000 images, and the final *F1-score* for threat classification was 0.89, which confirms the high accuracy of the algorithm. The metric was calculated using the following formula:

$$F1 = 2 \cdot \frac{Precision \cdot Recall}{Precision + Recall}$$

where *Precision* — the proportion of correctly classified objects among all detected objects, *Recall* — the proportion of correctly classified objects among all true positive cases.

Conclusion. The developed algorithm for localization and direction determination of threats in unmanned ground transport demonstrates high efficiency, achieving an F1 score of 0.89 on a collected dataset containing 1000 images. The novelty of the approach lies in the integration of Vision-Language Models (VLM) with fine-tuning on contextual queries, allowing the use of not only visual data but also textual information for a deeper analysis of object behavior and their interaction with the environment. This approach provides more accurate and adaptive threat recognition compared to classical detectors.

In the future, the algorithm will be improved with a focus on adapting VLM for more precise analysis of complex scenes, including scenarios with high object density and changing lighting conditions.

REFERENCES

1. **Umang Goenka, Aaryan Jagetia, Param Patil, Akshay Singh, Taresh Sharma, Poonam Saini:** Threat Detection In Self-Driving Vehicles Using Computer Vision, Network Security and Data Sciences MIND-2021, 2021
2. **Ahmed M. Ibrahim, Rania M. Hassan:** Real-Time Collision Warning System Based on Computer Vision Using Mono Camera, 2nd Novel Intelligent and Leading Emerging Sci. Conf.(NILES), 2020
3. <https://habr.com/ru/companies/yandex/articles/763348/>
4. **Ziang Guo, Zakhar Yagudin, Artem Lykov, Mikhail Kononov, Dzmitry Tsetserukou:** VLM-Auto: VLM-based Autonomous Driving Assistant with Human-like Behavior and Understanding for Complex Road Scenes, IEEE, 2024
5. **Naoki Wake, Atsushi Kanehira, Kazuhiro Sasabuchi, Jun Takamatsu, and Katsushi Ikeuchi:** Open-Vocabulary Action Localization with Iterative Visual Prompting, arXiv preprint arXiv:2408.17422v4, 2024

6. **Ashish Vaswani, Noam Shazeer, Niki Parmar, Jakob Uszkoreit, Llion Jones, Aidan N. Gomez, Lukasz Kaiser, Illia Polosukhini:** Attention Is All You Need, 31st Conference on Neural Information Processing Systems (NIPS 2017), Long Beach, CA, USA, 2017
7. **Zhiliang Peng, Wenhui Wang, Li Dong, Yaru Hao, Shaohan Huang, Shuming Ma, Furu Wei:** Kosmos-2: Grounding Multimodal Large Language Models to the World, arXiv preprint arXiv:2306.14824, 2023
8. **Edward J. Hu, Yelong Shen, Phillip Wallis, Zeyuan Allen-Zhu, Yanzhi Li, Shean Wang, Lu Wang, Weizhu Chen:** LoRA: Low-Rank Adaptation of Large Language Models, arXiv preprint arXiv:arXiv:2106.09685v2, 2021
9. **Jong-Wook Kim , Jin-Young Choi, Eun-Ju Ha and Jae-Ho Choi:** Human Pose Estimation Using MediaPipe Pose and Optimization Method Based on a Humanoid Model, Applied Sciences 13, 2700., 2023.

S.P. ABLYASOVA
(Lomonosov Moscow State University, Moscow)

SIMULATION OF TRAJECTORY PARAMETERS OF OBJECT MOTION IN POLE AREAS USING QUASI-GEODETIC COORDINATES

The task of simulating the trajectory parameters of an object - coordinates, linear velocity components, attitude angles, and "ideal" readings from inertial sensors such as angular rate sensors and accelerometers when the object is moving above or below the pole - is needed for testing onboard navigation algorithms of inertial navigation systems, such as strapdown inertial navigation system (INS). The unique aspect of the simulation problem mentioned is that traditional parameters such as longitude and heading cannot be used in relevant models, as these parameters are not defined for points lying on the axis of Earth's rotation. It has been demonstrated that this simulation can be performed using the quasi-Greenwich coordinate system, quasi-geodetic (or quasi-geocentric) coordinates, and quasi-angles of orientation, instead of the traditional ones. The zero test of inertial dead reckoning algorithms when the trajectory of an object crosses the axis of Earth's rotation confirms the proposed solution to the problem.

Introduction. The task of simulation of an object's trajectory parameters and corresponding inertial sensors readings in case when trajectory meets the axis of Earth rotation, in particular the north pole, is considered. Due to the fact that traditional models of trajectory simulators typically use a geodetic reference frame, these models are not suitable for use in areas near the poles. For this reason, the use of a quasi-Greenwich reference system and an appropriate quasi-geodetic navigation frame, as well as quasi-attitude angles, instead of traditional ones, is relevant. The report presents an approach to simulating the motion trajectory and its corresponding "ideal", i.e., error-free, measurements from INS inertial sensors. Based on this simulation, we compute a set of trajectory parameters to test onboard algorithms (dead reckoning) in polar regions.

Quasi-Greenwich and quasi-geodetic coordinate systems. In trajectory simulation procedure it is assumed that a vehicle crosses the pole in the meridian plane with the known value of geodetic longitude λ_0 . It is also proposed that the initial value of geodetic latitude φ_0 is close enough to 90° . In the context of the transition to a quasi-Greenwich reference system and a quasi-geodetic reference frame, the meridian mentioned is defined as the plane of the quasi-equator. Consequently, the quasi-latitude at the pole is zero.

The quasi-Greenwich $O\eta^q$ coordinate system is introduced by two consecutive rotations of the Greenwich reference system $O\eta$ around the axis $O\eta_2$ by the angle $-\frac{\pi}{2}$ and around the new position of the first axis by the angle $-\frac{\pi}{2} + \lambda_0$. The quasi-equator plane coincides with the plane of the meridian with geodetic longitude λ_0 .

The quasi-geodetic Ox^{0q} coordinate system is introduced by two consecutive rotations of the Greenwich coordinate system $O\eta^q$ around the axis $O\eta_3^q$ by the angle $\lambda^q + \frac{\pi}{2}$ and around the new position of the first axis by the angle $\frac{\pi}{2} - \varphi^{0q}$.

Trajectory simulation. In order to model the trajectory in quasi-coordinates, the use of kinematic equations for the motion of the IMU accelerometer's proof mass, M, is proposed.:

$$\begin{aligned}\frac{d}{dt}\varphi^{0q} &= \frac{V_N^q}{R}, \\ \frac{d}{dt}\lambda^q &= \frac{V_E^q}{R \cos \varphi^{0q}}, \\ \frac{d}{dt}R &= V_{UP}^q,\end{aligned}\tag{1}$$

Scientific adviser: A. A. Golovan, Lomonosov Moscow State University, Moscow, Russia

where V_E^q, V_N^q, V_{UP}^q are the components of the M velocity vector relative to the axes of the quasi-geodetic coordinate system Ox^{0q} , R represents the modulus of the radius vector OM.

The initial conditions for equations (1) are as follows:

$$\begin{aligned} \varphi^{0q}(t_0) &= 0, \\ \lambda^q(t_0) &= \frac{\pi}{2} - \varphi^0(t_0), \\ R(t_0) &= a + h(t_0) - \frac{ae^2}{2} \sin^2 \varphi(t_0) (\cos^2 \varphi(t_0) - \frac{1}{4} \sin^2 \varphi(t_0)) + O(0, 1M), \\ \psi^q(t_0) &= -\frac{\pi}{2}, \end{aligned} \quad (2)$$

where $\varphi^0(t_0)$ and $\varphi(t_0)$ are the values of geocentric and geodetic latitudes, respectively, at the initial time t_0 , $h(t_0)$ – geodetic altitude at time t_0 , ψ^q – quasi-heading angle, i.e. the angle between the axis Mx_2^{0q} (the direction towards quasi-north) and the projection of the longitudinal body axis on the plane $Mx_1^{0q}x_2^{0q}$. This angle is counted in a clockwise direction from the axis Mx_2^{0q} . Throughout the entire trajectory modelling interval, the quasi-heading angle $\psi^q(t_0) = -\frac{\pi}{2}$, which corresponds to the motion of the object along the quasi-equator towards quasi-longitude decrease.

The kinematic equations (1) are integrated with the initial conditions (2). The trajectory obtained in quasi-geodetic coordinates is used in the simulation of inertial sensor readings.

Modelling of inertial sensors readings. Prior to modelling accelerometer readings, it is necessary to determine the absolute angular rate vector of the body frame Ms of an object. This step is similar to the established methodology for modeling ARS readings in geodetic coordinates. [2].

Accelerometer readings are calculated using the point M motion equations in the axes. Mx^{0q} (see [1], [2]):

$$\begin{aligned} \frac{d}{dt} A_{x^{0q}\eta^q} &= \hat{\Omega}_{x^{0q}} A_{x^{0q}\eta^q}, \\ \frac{d}{dt} V_{x^{0q}} &= (\hat{\Omega}_{x^{0q}} + 2 \hat{u}_{x^{0q}}) V_{x^{0q}} + f_{x^{0q}} + g_{x^{0q}}, \end{aligned} \quad (3)$$

where $A_{x^{0q}\eta^q}$ is orientation matrix of the navigation frame Mx^{0q} with respect to the quasi-Greenwich coordinate system $O\eta^q$, the term $f_{x^{0q}}$ represents the vector of specific force acceleration at the point M in the navigation frame (ideal accelerometer measurements), $\hat{u}_{x^{0q}}$ is a skew-symmetric matrix that corresponds to the vector of angular rate of the Earth's rotation in the frame Mx^{0q} , $g_{x^{0q}}$ represents the normal gravity vector and $\Omega_{x^{0q}}$ is an angular rate vector of the quasi-geodetic frame Mx^{0q} .

Zero test. Based on the simulated inertial sensor readings, the algorithm of the INS dead reckoning was tested. For this purpose the geodetic wander azimuth reference frame was used as a navigation frame. This type of navigation frame is traditionally used in airborne navigation. The results of the dead reckoning test demonstrated a practical coincidence between the calculated trajectory parameters and the original trajectory parameters that were the basis of the simulation.

Conclusions. The results demonstrate that quasi-coordinates and quasi-orientation angles are the appropriate variables for modelling the trajectory parameters of an object's motion crossing points above and below the pole. This approach allows for the further full-scale dead reckoning algorithms testing on trajectories of this nature.

REFERENCES

1. Vavilova N.B., Golovan A.A., and Parusnikov N.A., *Matematicheskie osnovy inertial'nykh navigatsionnykh sistem.* (Mathematical Foundations of Inertial Navigation Systems), Moscow: Moscow State University, 2020.

2. Bogdanov O.N. Metodika soglasovannogo modelirovaniya izmerenij inercial'nyh datchikov, traektornyh parametrov ob"ekta s prilozheniem k zadacham inercial'noj i sputnikovoj navigacii. (Methodology of agreed modelling of measurements of inertial sensors, trajectory parameters of object with application to problems of inertial and satellite navigation), dissertation for the degree of Candidate of Physical and Mathematical Sciences, 2015
3. Lukyanov D.P., Mochalov A.V., Odintsov A.A., Vaisgant I.B. *Inercial'nye navigacionnye sistemy morskikh ob"ektov*. (Inertial navigation systems of marine objects), Leningrad: Sudostroenie

D.A. SAFIN
(Lomonosov Moscow State University)

AN ALGORITHM FOR RAW DATA FUSION OF A STRAPDOWN INERTIAL NAVIGATION SYSTEM AND ODOMETER

The paper describes an algorithm for data fusion of a strapdown inertial navigation system and odometer. The data fusion algorithm corrects the parameters of the inertial and odometry dead reckoning, provides estimates of the instrumental errors of the inertial sensors and the lever arm parameters in the inertial navigation system (INS) and odometer system, as well as the instrumental errors of the odometer, using the Kalman filter. The results of the experimental data processing for different types of land vehicles, including cars and tractors, have been presented. These findings demonstrate the effectiveness of the algorithm that was developed.

Introduction. Data fusion, provided by a strapdown inertial navigation system (INS) and an odometer, is widely used in various applications, including road surveying, self-driving vehicles, and agricultural machinery.

The source of initial data used to solve ground vehicle navigation problems is data from inertial sensors, such as accelerometers and gyroscopes, which are part of an inertial navigation system (INS). Additionally, data from an odometer, which records the absolute distance traveled by an object, is used. The given research examines the task of integrating INS (Inertial Navigation System) and odometer data in order to identify potential precision issues with this integration. However, the use of other available navigation information that is recorded, for example, by a global navigation satellite system (GNSS) receiver, is also considered.

Algorithms for data fusion form the basis of land vehicle navigation. They are used both in real-time and in post-processing modes. The Kalman filter is used as an assessment algorithm.

During the development of the algorithm, the following specific tasks were completed:

1. Initial alignment of the INS in the presence of uncontrolled angular motion of the vehicle's body frame.
2. Detecting the movement of an object in reverse, if the odometer measures an unsigned increment of the path.
3. Recalibration of the strapdown INS-odometer system according to results of data processing in previous tracks. Adjusting parameters are: two installation angles of INS instrument frame with respect to odometer measuring axis of the odometer, scale factor error of the odometer.
4. The size effect is due to the mutual displacement of the center of the INS and the odometer measuring point.
5. Application of Kalman-type smoothing algorithm in INS-odometer post-processing mode in case of known coordinates of the final stopping point.
6. Testing of Zero Velocity Update Technology (ZUPT-correction) when the vehicle stops.

Specifics of the development of data fusion algorithm.

1. A three-dimensional autonomous INS dead reckoning system is applied. Unstable INS altitude channel is being damped.
2. Three-dimensional odometric dead reckoning based on odometer reading and INS orientation parameters is applied.
3. The positional data from odometric dead reckoning are used for INS positional aiding with dampening of its vertical channel.

The main mathematical models of the INS integration tasks of the basis of odometer readings:

1. 3D INS error equations
2. 3D odometer dead reckoning error equations
3. INS position aiding based on odometer-derived coordinates.

The following data are included into the state vector of estimated parameters:

1. inertial and odometric dead reckoning errors
2. parameters of inertial sensors instrumental error models
3. scale factor error of the odometer
4. parameters of interrelated geometry of odometer and INS:
 - interrelated misalignment of INS–odometer system in yaw and pitch channels
 - lever arm parameters in the INS-odometer system

Test data, Moscow city. Three diagnostic test runs were carried out using the car which had navigational-grade strapdown INS installed in it.

The results of odometric dead reckoning were used only for INS positioning aiding.

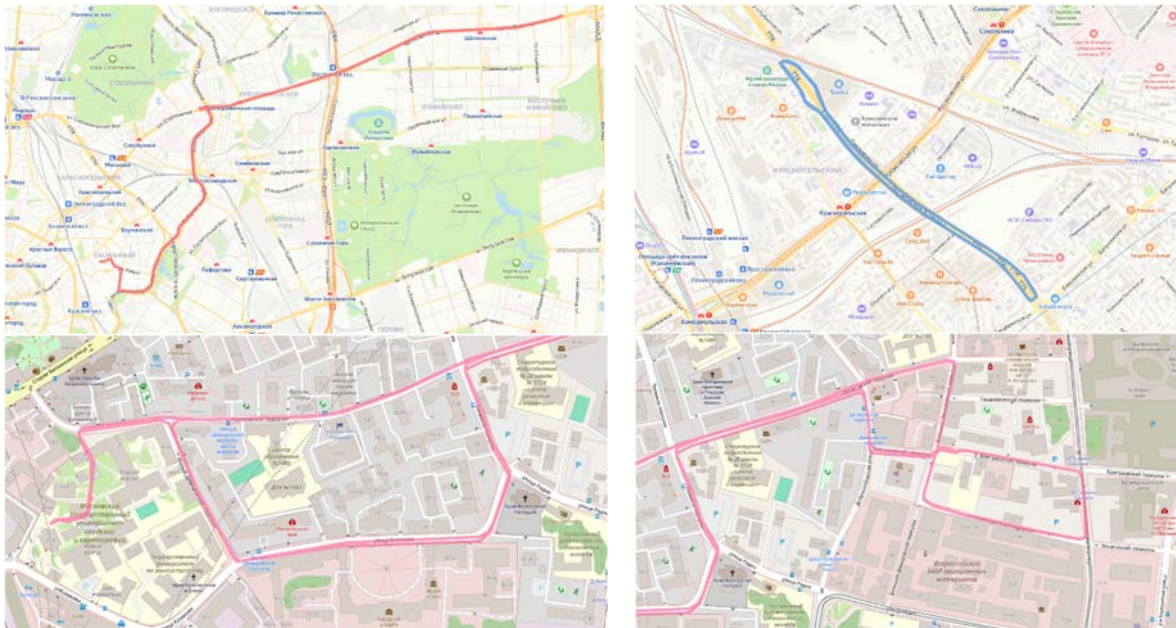


Fig. 1–4. Adjusted trajectory on the map (real time algorithm)

In post-processing mode and in all the test rides we have obtained nearly the same estimation of misalignment parameters. In order to improve the precision of navigation we have verified the effectiveness of misalignment parameters compensation (finishing calibration of strapdown INS-odometer system).

Test track using microelectromechanical system-based sensors (MEMS-based sensors). Positioning data from odometer was used for the aiding purposes, i.e. the result of the odometric dead reckoning and positioning data from global navigation satellite system (GNSS). Estimation algorithm was used in the feedback mode.



Fig. 5. Adjusted trajectory in real time



Fig. 6. Tractor with MEMS and odometer and GNSS receiver on the map

In post-processing we have received estimation of misalignment parameters and vector of MEMS and odometer bedding point angle that demonstrated a high precision of anticipatorily measurements.

Conclusion. The results of test data processing have shown performance efficiency of strapdown INS-odometer integration algorithm, as well as acceptable accuracy in solving navigation tasks using sensors of various accuracy grades. The results demonstrate the effectiveness of finishing calibrations of INS-odometer system.

REFERENCES

1. **Vavilova N.B., Golovan A.A., Parusnikov N.A.** "Mathematical principles of navigation systems" Publishing house of Moscow University, 2020.
2. **Golovan A.A., Nikitin I.V.** "Integration problems of strapdown INS and odometer from the point of view of the mechanics of adjusting inertial navigation systems" Part 1, Part 2 "Moscow University Journal. Mathematics. Mechanics." №2, pages 69-72, №4, pages 68-72, Moscow, 2015.
3. **Golovan A.A.** "Integration solution "Strapdown INS-odometer": positional (place-value) version (variant) // Gyroscopy and navigation. 2021, vol. 29. № 2. pages 110-125. DOI 10.17285/0869-7035.0066.

V. SMETANINA

(Saint Petersburg State University, Saint Petersburg)

IDENTIFICATION OF SPATIOTEMPORAL CLUSTERS IN MULTI-AGENT SYSTEMS USING AN ENDEMIC MODEL

The paper presents an approach to cluster detection in distributed multi-agent systems using an endemic model. By modelling the "activation" of an agent as an infectious process, the study demonstrates that patterns of joint activation indicate spatial proximity, without requiring explicit information about the distance between agents.

Introduction. Modern systems are characterized by increasing complexity and dimensionality, which makes centralized management strategies resource-intensive in terms of computing and communication costs. This has led to an increase in interest in distributed multi-agent systems that are used in various fields such as unmanned vehicles, distributed sensor networks, group robots and aircraft.

The complexity of such systems creates serious problems for traditional management methods. These methods are often unable to effectively control each individual agent, and they also do not take into account the properties of the system at a macro level [1]. By investigating how individual agents spontaneously form consistent structures at meso-levels, we can obtain important information about how to control multidimensional systems [2], [3]. In addition, many of these systems also have self-organizing properties, which dynamically form clusters. In this regard, control methods need to adapt to these dynamic structures. The paper [4] describes the formation of mesoscopic structures using the example of an aircraft with a large number of "feathers" distributed over the surface, i.e. elements with pressure sensors and rotary devices. It was shown that in conditions of turbulence, when the reaction of the system is nonlinear, the collective movement of the agents of the "feathers" can lead to their self-organization and a change in the flow regime of the aircraft body, thereby forming clusters of agents on the surface of the plane.

Cluster management strategies show better results compared to management approaches for macro and micro levels. Thus, in [5] an adaptive cluster management strategy with feedback was developed. Obtaining the clustering structure of the entire system was based on the compressed sensing method for a compact representation of the aggregated state of the agent, i.e. based on compressed measurements. Compared to micro-scale and macroscale approaches, cluster management outperformed these strategies in terms of convergence time, efficiency, and accuracy.

The problem of efficient cluster identification remains a matter of great urgency. The proposed work considers the formation of clusters based on periodic activation of agents and subsequent analysis of the dynamics of their spread using the endemic SIR (Susceptible, Infected Recovered) model. Just as the spread of infection in the SIR model demonstrates possible contacts in society [6], it is assumed that groups of agents, often activated together, are in spatial proximity to each other. By accurately identifying clusters that represent cohesive groups of interacting agents, we gain a deeper understanding of the internal organization of the system and can develop more effective management strategies. Unlike static approaches, the SIR model reflects the temporal evolution of agent interactions through the process of "activation", which allows us to identify clusters that arise, disintegrate and transform over time.

The proposed work is devoted to the identification of clusters in a distributed multi-agent system through the periodic activation of individual agents.

Problem statement. Consider a system with N agents (in a set of $N = \{1, \dots, N\}$), which are placed into a bounded region and are tasked to reach a certain goal point x^* . Each agent, possesses a state $x_i[t] \in R^d$, which may act as its location on a coordinate plane (therefore $d = 2$) or in a higher-dimensional coordinate space.

¹ Academic Advisor: Dr. Oleg Granichin, Doctor of Physical and Mathematical Sciences, Professor in the Department of System Programming, Faculty of Mathematics and Mechanics, Saint Petersburg State University.

The aim is to analyse the spatiotemporal patterns of active agents over time and draw a conclusion about the underlying spatial distribution. In this way, identify groups of agents that are often activated together, which will indicate their close proximity.

Conditions for solving the problem. To solve the problem, it is assumed that agents can interact in accordance with the communication graph. The interactions of agents are described through the adjacency matrix $A = [a_{ij}]$, where $a_{ij} \neq 0$ means the presence of a connection between agents i and j , and $a_{ij} = 0$ means its absence. The dynamics of changes in the states of agents is described as follows: with discrete time intervals $t = 0, 1, 2, \dots$ a subset of agents is randomly selected for "calling". Let $C_t \subseteq \{1, 2, \dots, N\}$ be a set of agents called at time t . The selection of C_t is carried out by uniform sampling with a fixed probability. When agent i is called at time t (i.e. $i \in C_t$), its "nearest neighbours" become "active". The function $N(i, r)$, which returns a set of agents within a radius r of agent i , is described:

$$N(i, r) = \{j \in \{1, 2, \dots, n\} : \|p_i - p_j\| \leq r\}, \quad (1)$$

where p is the coordinates of the location.

Activation propagation is described by the SIR dynamic model (simplified view):

$$\dot{G} = F(G) = \begin{cases} \dot{S} = S(A - S) - \beta_\gamma(t)IS \\ \dot{I} = \beta_\gamma IS - \frac{rI}{a + I} \end{cases}, \quad (2)$$

where $\beta_\gamma = \beta_0(1 + \Phi(\omega t))$, $G(t) = (S(t), I(t))$, A is the tolerance coefficient for susceptible agents in the absence of activation, γ is the amplitude of periodic oscillations, $\omega > 0$ frequency, β_0 is the rate of activation transmission in the absence of periodicity, a is the delay coefficient during recovery.

Conclusion. As a result of the research, a modelling environment was developed to visualise emerging spatial structures. Analysis of the patterns of pathogen activation over time reveals distinct temporal spikes as shown in Fig. 1. These spikes correspond exactly to moments when the spread of infection in SIR models is simulated during the "activation" process, agents are geographically grouped and isolated. Further research could be aimed at developing predictive models to predict activation patterns and system behaviour which would allow more accurate identification of clusters and consequently better control.

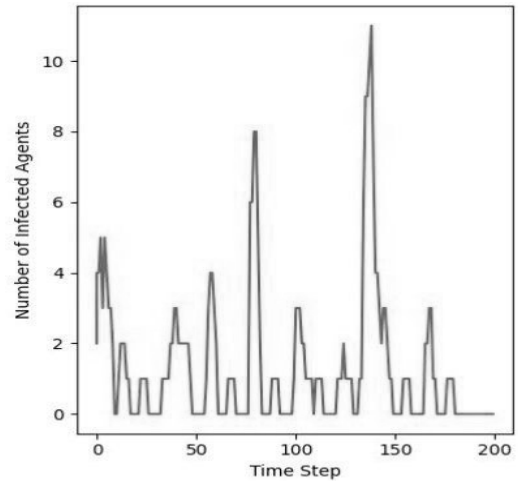


Fig.1. The number of "active" agents over time

The research was carried out within the financial support for the autonomous non-profit organization "Analytical Center for the Government of the Russian Federation" (Agreement No. 70-2024-000120 dated March 29, 2024, id: 000000D730324P540002)

REFERENCES

1. **H. Li, Y. Li, H. V. Zhao**, "Modeling Decision Process in Multi-Agent Systems: A Graphical Markov Game based Approach, APSIPA ASC, 2020, pp. 197-204.
2. **Amelin K., Granichin O.**, et al, A new method of adaptive mesoscale control in complex multiagent networked dynamical systems. Cybernetics and Physics, 2022. Vol. 11, Number 4. PP. 175-189.
3. **Cristin, J.** et al. Spatiotemporal organization of ant foraging from a complex systems perspective. Sci. Reports, 2024, Vol. 14, 12801.
4. **Granichin O., Khantuleva T., Amelina N.** Adaptation of aircraft's wings elements in turbulent flows by local voting protocol. IFAC-PapersOnLine 50, 2017, 1904–1909.
5. **Erofeeva V., Ershov V., Granichin O., Pankov V., Uzhva D., Granichina O.** Adaptive distributed cluster flow control for a group of autonomous robots, IFAC-PapersOnLine, Vol. 56, Issue 2, 2023, pp.8690-8695.
6. **Maurício de Carvalho J., Rodrigues A.**, Strange attractors in a dynamical system inspired by a seasonally forced SIR model, Physica D: Nonlinear Phenomena, 2022, Vol. 434, 133268.

D. MINGAZOV, M. KOZIN¹
(Saint Petersburg State University, Saint Petersburg)

RESEARCH ON CONSENSUS AND FIXED-TIME CONTROL METHODS FOR MULTI-AGENT SYSTEMS

This work examines consensus and fixed-time control algorithms for multi-component systems. The study explores mathematical models using iterative consensus and control methods, and proposes a fixed-time approach based on nonlinear functions. Numerical experiment results are provided to demonstrate the effectiveness of the proposed methods.

Introduction. Modern multi-agent systems (MAS) are a critical area of research, particularly in their applications within robotics, autonomous vehicle control, and communication networks. Coordinating agents, each following local behavioral rules and interacting with neighbors, presents a significant challenge. A key issue is achieving a consistent state (consensus) across all agents in the system, despite limited computational resources and time constraints.

Traditional consensus methods, such as linear information exchange models between agents, were introduced in the work of Olfati-Saber et al. [3]. These methods enable asymptotic convergence to a common state, making them useful for various practical applications. However, a major drawback of these algorithms is the requirement of unlimited time to reach consensus. This limitation reduces their effectiveness in systems that require convergence within a finite time.

To address this issue, fixed-time control (Fixed-Time Convergence, FTC) methods have been proposed, ensuring system convergence within a fixed time interval regardless of the agents' initial conditions. This approach is based on nonlinear control functions and was thoroughly discussed in the works of Polyakov and Parsegov [4]. These methods guarantee rapid state alignment among agents, allowing consensus to be achieved in fixed time, which makes them appealing for tasks where response speed is critical.

This study investigates combined consensus and FTC methods for multi-agent systems. Specifically, an algorithm is considered that employs nonlinear control functions to accelerate convergence. The control expression is written as follows:

$$U_t = \sum_{j \neq i} K_1 (\sqrt[3]{|x_i - x_j|}) + K_2 (x_i - x_j)^3 \quad (1)$$

where: x_i and x_j are the states of agents, and K_1 and K_2 are constants that regulate the rate of convergence. Using such control functions enables consensus to be reached faster and within a finite time compared to classical approaches.

This report is focused on examining the effectiveness of combined consensus and fixed-time control methods for multi-agent systems. Numerical experiments are presented to demonstrate the advantages of the proposed approach in managing systems with limited time resources.

Problem Statement. We consider a system with N agents, each with a state $x_i(t)$ at time t , where $i = 1, 2, \dots, N$. The goal is to develop an algorithm that ensures consensus among all agents within a fixed time. This implies that there exists a time T after which the states of all agents coincide:

$$x_i(t) = x_j(t) \quad \forall i, j \in \{1, 2, \dots, N\} \quad (2)$$

The task is to develop a control algorithm that ensures the alignment of all agents' states within a finite time T , regardless of their initial conditions.

Problem Conditions. To solve the problem, it is assumed that agents can interact with a limited number of neighbors according to a communication graph. The interactions between agents are described by an adjacency matrix $A = [a_{ij}]$, where $a_{ij} \neq 0$ indicates a connection between agents i

¹ **Academic Advisor:** Dr. Oleg Granichin, Doctor of Physical and Mathematical Sciences, Professor in the Department of System Programming, Faculty of Mathematics and Mechanics, Saint Petersburg State University

and j , and $a_{ij} = 0$ indicates its absence. The dynamics of the agents' state changes are described as follows:

$$x_i^{(t+1)} = x_i^{(t)} + \sum_{j \neq i} a_{ij} [K_1 (\sqrt[3]{|x_j^{(t)} - x_i^{(t)}|}) + K_2 (x_j^{(t)} - x_i^{(t)})^3] \quad (3)$$

where: K_1 and K_2 are positive constants that regulate the rate of convergence. This nonlinear control function includes two components: the first component, involving the cubic root, is responsible for the "soft" alignment of agent states, while the second accelerates the consensus process through the cubic difference of states.

Stability Analysis. To analyze the stability of the system, let us consider the Lyapunov function $V(t)$, defined as:

$$V(t) = \frac{1}{2} \sum_{i=1}^N \sum_{j=1}^N a_{ij} (x_j(t) - x_i(t))^2 \quad (4)$$

This function characterizes the divergence of agent states and must decrease over time to ensure convergence. The time derivative of the Lyapunov function is calculated as:

$$\hat{V}(t) = -K_1 \sum_{i=1}^N \sum_{j=1}^N a_{ij} (\sqrt[3]{|x_i - x_j|})^2 - K_2 \sum_{i=1}^N \sum_{j=1}^N a_{ij} (x_j(t) - x_i(t))^6 \quad (5)$$

Both terms are decreasing, which confirms the stability of the proposed algorithm and guarantees that all agents converge to a single state within a finite time T .

Conclusion. This study examined various dynamic models for controlling multi-agent systems, specifically the consensus protocol, the Round-Robin algorithm, and a modified protocol incorporating Fixed-Time Convergence (FTC) elements. The findings indicate that FTC significantly enhances the convergence rate of the system due to its adjustable parameters, K_1 and K_2 , which allow for precise control over the consensus achievement time.

Optimizing parameters K_1 and K_2 further demonstrated that FTC surpasses traditional methods in convergence speed. Future research could focus on fine-tuning these parameters through adaptive techniques or machine learning approaches. It is also crucial to investigate the application of FTC in the context of partially connected agent networks and under resource constraints.

In summary, this work illustrates the efficacy of FTC algorithms for achieving rapid consensus, and continued research will likely extend their applicability to more complex systems.

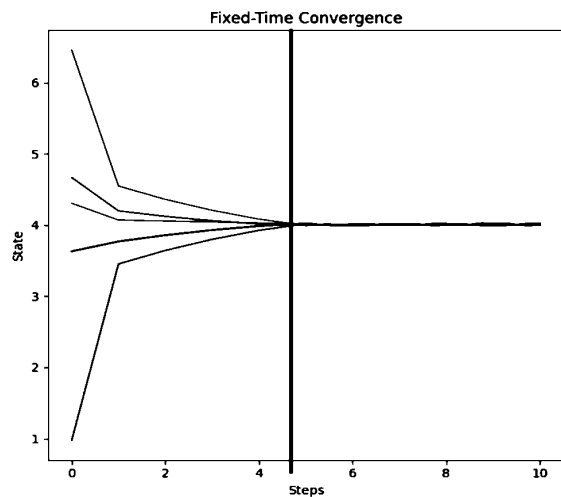


Fig. 1. Increase in Convergence Speed for 5 Agents

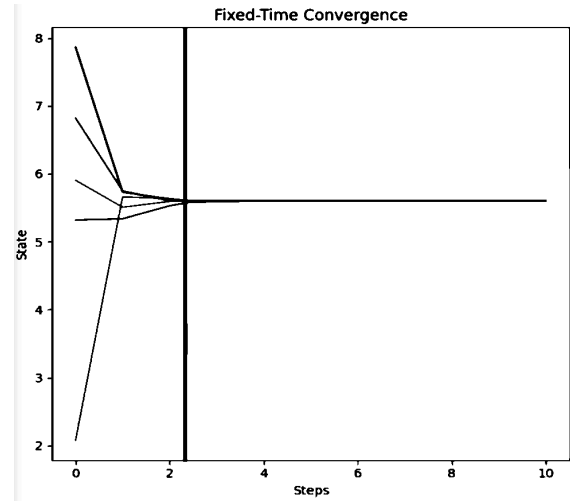


Fig. 2. Increase in Convergence Speed for 5 Agents

THE RESEARCH WAS CARRIED OUT WITHIN THE FINANCIAL SUPPORT FOR THE AUTONOMOUS NON-PROFIT ORGANIZATION "ANALYTICAL CENTER FOR THE GOVERNMENT OF THE RUSSIAN FEDERATION" (AGREEMENT NO. 70-2024-000120 DATED MARCH 29, 2024, ID: 000000D730324P540002).

REFERENCES

1. **Amelina N.O., Granichin O.N., Fradkov A.L.** Method of Averaged Models for Discrete Adaptive Systems. Moscow: Automation and Telemekhanics, 2019, No. 10, pp. 3–36.
2. **Amelina N.O., Fradkov A.L.** Approximate Consensus in a Stochastic Dynamic Network with Incomplete Information and Measurement Delays. Moscow: Automation and Telemekhanics, 2012, No. 11, pp. 6–29
3. **Olfati-Saber R., Fax A., Murray R.M.**, Consensus and Cooperation in Networked Multi-Agent Systems, Proceedings of the IEEE, 2007, Vol. 95, No. 1.
4. **Parsegov S.E., Polyakov A.E., Shcherbakov P.S.**, Fixed-Time Consensus Algorithm for Multi-Agent Systems with Integrator Dynamics, IFAC Proceedings Volumes, 2013, Vol. 46, No. 27, pp. 110-115.
5. **Chen Y., Wang F., Wang B.**, Fixed-Time Convergence in Continuous-Time Optimization: A Fractional Approach, IEEE Control Systems Letters, 2022, Vol. 7, P. 631-636
6. **Ge P., Li P., Chen B., Teng F.**, Fixed-Time Convergent Distributed Observer Design of Linear Systems: A Kernel-Based Approach., IEEE Transactions on Automatic Control, 2023, Vol. 68, P. 4932-4939

A. O. KOMAROV
(NNSTU n.a. R.E. Alekseev, Nizhny Novgorod)

A. R. BRAZHENKO
(St. Petersburg Federal Research Center of the RAS, Saint Petersburg)

A SCENE BUILDING ALGORITHM FOR VISUALIZING OBSTACLES USING TWO CAMERAS

A building of 2D Bird's-Eye View (BEV) map for visualizing obstacles using information from two cameras is proposed. Based on the depth map, a 2D BEV scene is built, which displays the objects necessary for the functioning of the route planning system. This makes it possible to provide an exact visualization of the environment for subsequent automatic parking, automatic driving or flying in real conditions.

Introduction. Currently, the development of autonomous transportation is becoming a key area that will define the future of transportation infrastructure. Autonomous transportation systems have the potential to improve road safety, reduce the number of accidents, and optimize resource usage. One of the most important aspects is the construction of a BEV (Bird's Eye View) map, which provides the autopilot with an accurate representation of the surrounding environment. Modern systems [1, 2, 3] focus on object detection in urban environments, such as traffic signs, pedestrians, and others. However, autonomous vehicles can also be used outside of cities, where a more universal object detection method is required.

This paper is dedicated to an algorithm for constructing a BEV map without the use of LiDAR or radar, unlike the works [4, 5], which employ a multimodal approach. The algorithm demonstrates flexibility under various lighting and weather conditions, in contrast to traditional algorithms such as IPM (Inverse Perspective Mapping), which are sensitive to changes in the environment. The paper presents an approach that uses a neural network to estimate distance, while objects are detected using classical computer vision methods.

Problem Statement and Solution Method. The system should automatically process the image, extract depth information of objects, identify obstacles, and display them on a plane corresponding to a BEV (Bird's Eye View) projection.

The input consists of an image I_{RGB} , obtained from a camera capturing the surrounding environment in perspective projection. The image I_{RGB} is passed through a trained neural network F_θ (MiDaS [6]), which generates a **depth map** $D(x, y)$:

$$D(x, y) = F_\theta(I_{RGB}),$$

where x, y – pixel coordinates in the image, and $D(x, y)$ is the distance to the object in the scene for each point.

To obtain objects from the depth map, we will use classical computer vision methods.:

1. We apply adaptive histogram equalization to obtain a contrast-enhanced image.
2. We filter the image using Gaussian blur with a kernel 5×5 .
3. We use binarization and morphological filtering to eliminate noise
4. We find the contours of the obtained objects and create bounding rectangles.
5. Take camera positioning into account using the function G which transforms the object's bounding rectangle into coordinates on the BEV-map:

$$G(B_i) = \begin{cases} T_{front} \left(\frac{\left(x_i + \frac{w}{2}, y_i + \frac{h}{2}, D(x_i, y_i) \right)}{D(x_i, y_i)} \right), & \text{if the front camera is used} \\ T_{rear} \left(\frac{\left(x_i + \frac{w}{2}, y_i + \frac{h}{2}, D(x_i, y_i) \right)}{D(x_i, y_i)} \right), & \text{if the rear camera is used} \end{cases}$$

where T_{front} — the coordinate transformation matrix from the camera to BEV for the front camera, and T_{rear} — the coordinate transformation matrix for the rear camera, which accounts for the coordinate shift relative to the vehicle (e.g., inversion of direction along the Y-axis).

The center of the object and its width are projected into the BEV coordinate system:

$$P_{cam}(x_{center}, y_{center}, D(x_{center}, y_{center})) = K^{-1} \cdot \begin{bmatrix} x_{center} \\ y_{center} \\ 1 \end{bmatrix} \cdot D(x_{center}, y_{center}),$$

The final function $F(D(x, y), rear|front)$ - which takes the depth map as input and accounts for the camera position, will include the transformation of bounding boxes to the BEV map, considering the camera position:

$$\{P_{BEV}(X, Y)\} = F(D(x, y), rear|front) = \{G(B_i, rear|front)\} | B_i \in \text{BoundingBoxes}(D(x, y)),$$

Thus, for each bounding rectangle B_i we calculate the object's coordinates on the BEV map, considering whether it is the front camera or the rear camera.

An example of the algorithm in action. Shows two images from the camera with objects (1 from the front camera and 2 from the rear camera). On the constructed 2D BEV map, three objects are visible: one in front of our vehicle model and two behind it. The white lines represent the camera's field of view.

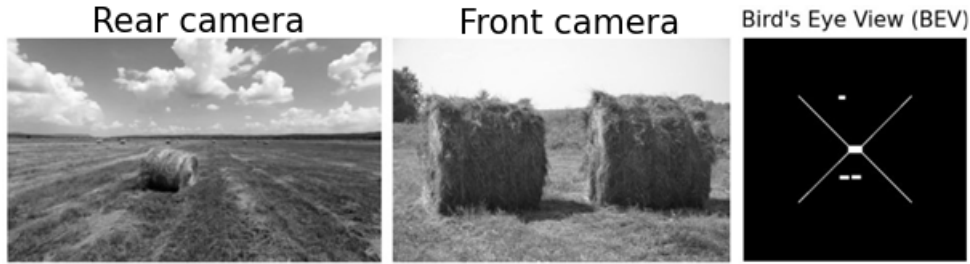


Fig. 1. Example of construction 2d BEV

To performance index the quality of the algorithm, we use a combined metric that simultaneously considers both the accuracy of object localization and the ability to determine the distance to objects:

$$LPS = \alpha \cdot AP - \beta \cdot DE_{norm},$$

where LPS(Localization Precision Score) – is the quality metric, α and β – are weight coefficients that determine the relative importance of detection accuracy and distance, AP(Average Precision) – is the average precision across various confidence threshold levels for all detected objects, and DE_{norm} – is the distance error.

The algorithm's accuracy based on the LPS metric is 0,57 on 100 images with predominantly agricultural objects, which is a good result for an algorithm that identifies obstacles it has not encountered before.

Conclusion. A method for constructing a scene in the Bird's Eye View (BEV) projection for visualizing obstacles based on data from two cameras is proposed. The algorithm includes several key steps: depth map creation, object segmentation in the image, determining their boundaries (bounding boxes), and projecting objects into the BEV coordinate system, considering the camera positions.

A metric, Localization Precision Score (LPS), is introduced, which effectively evaluates the algorithm's performance. Testing results on real data show that the algorithm can accurately identify obstacles, providing a high degree of reliability when building a 2D BEV scene.

One of the key advantages of the algorithm is its independence from complex and labor-intensive camera calibration. Moreover, the algorithm does not require the use of expensive sensors such as LiDAR or radar. This makes the proposed approach not only more accessible but also more flexible, ensuring stable performance under various lighting and weather conditions. All of this highlights its

potential for use in autonomous driving systems and other fields where efficient environmental visualization is required.

REFERENCES

1. **L. Reiher, B. Lampe and L. Eckstein:** A Sim2Real Deep Learning Approach for the Transformation of Images from Multiple Vehicle-Mounted Cameras to a Semantically Segmented Image in Bird's Eye View. IEEE 23rd International Conference on Intelligent Transportation Systems (ITSC), 2020
2. **Khawlah Bajbaa, Muhammad Usman, Saeed Anwar, Ibrahim Radwan, and Abdul Bais:** Bird's-Eye View to Street-View: A Survey. arXiv preprint arXiv: 2405.08961, 2024
3. **Jiayu Yang, Enze Xie, Miaomiao Liu and Jose M. Alvarez:** ParametricBEV: Parametric Depth Based Feature Representation Learning for Object Detection and Segmentation in Bird's-Eye View, ICCV, 2023
4. **Wending Zhou, Xu Yan, Yinghong Liao, Yuankai Lin, Jin Huang, Gangming Zhao, Shuguang Cui, Zhen Li:** BEV@DC: Bird's-Eye View Assisted Training for Depth Completion, 2023 IEEE/CVF Conference on Computer Vision and Pattern Recognition (CVPR), Vancouver, BC, Canada, 2023, pp. 9233-9242
5. **Haotian Hu, Fanyi Wang, Jingwen Su, Yaonong Wang, Laifeng Hu, Weiye Fang, Jingwei Xu, Zhiwang Zhang:** EA-LSS: Edge-aware Lift-splat-shot Framework for 3D BEV Object Detection, arXiv preprint arXiv:2303.17895, 2023
6. **Reiner Birkel and Diana Wofk:** MiDaS v3.1 -- A Model Zoo for Robust Monocular Relative Depth Estimation, arXiv preprint arXiv:2307.14460, 2023

D. I. SMOLIANOV
(Lomonosov Moscow State University, Moscow)

ON THE NAVIGATION PROBLEM OF UNMANNED WHEELED AGRICULTURAL MACHINERY USING INERTIAL, SATELLITES INFORMATION AND ODOMETRY.

The work describes the development, testing, and implementation of navigation algorithms for unmanned wheeled agricultural vehicles, vehicles when the navigation equipment consists a low-grade inertial navigation system, a receiver of global navigation satellite systems and odometry data — odometer-derived velocity and a steering sensor.

Introduction. The navigation problem is one of the most important in the operation of unmanned agricultural machinery. The positioning accuracy of the corresponding equipment needs to be a few centimetres for the treatment of most agricultural crops. High accuracy is also important to reduce fuel costs and ensure safe operation of agricultural machinery for humans. The reliability of the navigation solution depends on its stability to outliers and short-term losses of GNSS data.

Navigation equipment includes a low-grade inertial navigation system (INS) with microelectromechanical sensors (MEMS), a single antenna GNSS receiver (subsequently referred to as GNSS) and odometry — an odometer, and a steering sensor.

The paper considers two approaches to GNSS/INS/Odometry data fusion: loose and tight integrations. There are approaches to loose and tight integrations with odometer data [1, 2]. This work expands on these approaches by adding a new source of information – a steering sensor. We compare mentioned approaches.

Also, the work is devoted to a method of INS velocity fusion based on kinematic model properties of navigation objects – so-called component-wise ZUPT (Zero-Velocity Update Technology). Mentioned fusion does not require new sources of navigation information, but is based on the property of the movement of the ground vehicle. The relevant covariance analysis shows the observability of accelerometer biases in fusion proposed.

Kinematic models. The work examines the two most common configurations of agricultural vehicles: classic and articulated. Most tractors and combine harvesters have the classic configuration, i.e., a four-wheeled vehicle, which is steered by the front or the rear axle. Most tractors are steered by the front axle, while the rear axle steers most combines. The bicycle kinematic model [3, 4] is a sufficiently good approximation of classic vehicles without lateral slip. The articulated configuration implies two frames connected by a joint, each of which has two wheels fixed to the corresponding frame. In this configuration, one can make a turn by changing the angle between the frames. The articulated kinematic model [5, 6] is a sufficiently good approximation of articulated vehicles without lateral slip.

The kinematic equations of these models are used to construct the odometric dead reckoning in the loose integration with odometry and to construct the aiding measurements in the tight integration, which we discuss further.

Estimation problem. The traditional approach to solving this problem proposes the usage of geodetic reference frame as navigation frame in INS dead reckoning. We use GNSS data aiding if GNSS measurements are available. The fusion is implemented through feedbacks based on the estimates of the corresponding Kalman filter (KF). Methodically, the fusion comes down to solving the estimation problem (for illustration in continuous time)

$$\dot{y} = Ay + q, z = Hy + r, \quad (1)$$

where y is the state vector, A is the matrix that corresponds to the INS linear error equations used and to the model of the odometer and steering instrumental errors, q, r are vector-valued zero-mean white-noise processes, z is the measurement vector, generated by GNSS and odometer data, H is the corresponding observation matrix.

Loose INS/Odometry integration. The loose INS/Odometry integration implies two simultaneously working reckonings — inertial and odometric, as well as two integrated estimation problems. The inertial estimation problem was described in [1] with the state vector

$$y_1 = (\Delta x^T, \delta V^T, \alpha_1, \alpha_2, \beta_3, k^v, \kappa_1, \kappa_3, v_0^T, \Delta f_0^T)^T, \quad (2)$$

where Δx is INS position errors, δV is the vector of INS dynamic velocity errors, α_1, α_2 indicate the deflections of virtual horizon, β_3 is the azimuth attitude error, k^v is the odometer scale factor error, κ_1, κ_3 are the misalignment angles between the «measuring» axis of the odometer wheel and the INS instrument axes, v_0 is the vector of the angular rate sensors (ARS) drifts, Δf_0 is the biases vector of the accelerometers.

The state vector of the odometric estimation problem is

$$y_2 = (\Delta x_1^*, \Delta x_2^*, \Delta \psi, k^{v*}, k^{\delta_0}, k^{\delta_1})^T, \quad (3)$$

where $k^{\delta_0}, k^{\delta_1}$ are a null bias and a scale factor of steering sensor.

The two state vectors shown have common components, but the values of the estimates of these components may differ; the subscript (*) is used to demonstrate this fact.

The dynamic equations for y_1 are based on traditional INS error equations [7]. Dynamic equations for y_2 are based on linearised odometric reckoning error equations.

This approach can be called traditional, combining two traditional approaches to ground-based navigation — inertial and odometric. The advantage of this approach is the independent execution of two parallel estimation tasks, which increases the reliability in the event of failure of one of the components.

Tight INS/Odometry integration. The tight INS/Odometry integration implies one reckoning — inertial dead reckoning. In this case, the estimation problem is also single, but with an extended state vector

$$y = (\Delta x^T, \delta V^T, \alpha_1, \alpha_2, \beta_3, k^v, \kappa_1, \kappa_3, k^{\delta_0}, k^{\delta_1}, v_0^T, \Delta f_0^T)^T. \quad (4)$$

Odometry data is used as aiding measurements in this approach.

The advantage of this approach is that it eliminates the additional computational costs associated with the redundancy of estimation problems that arise from the loose integration approach.

Component-wise ZUPT. Here, component-wise ZUPT (Zero-Velocity Update Technology) means aiding by zero components of the heading point velocity vector. This method allows aiding even in the absence of odometer measurements, and, moreover, does not require stopping, unlike the classic ZUPT method. The heading point is a point whose velocity vector has direction along the longitudinal axis of the vehicle without any lateral slip. This property can be described by a non-holonomic constraint of the following form

$$\dot{x}_1 \cos \psi - \dot{x}_2 \sin \psi = 0, \quad (5)$$

where x_1, x_2 are the horizontal coordinates, ψ is the heading angle.

Conclusion. We present two approaches for integrating INS and odometry data: loose and tight integration. We consider two kinematic configurations: classic and articulated. We demonstrate that these two methods are equivalent in terms of their behaviour with respect to accelerometer biases and odometry coefficient estimates. Furthermore, we present the so-called component-wise ZUPT approach for INS aiding, which is based on kinematic models of the movement for ground wheeled vehicles. This approach does not require any additional navigation sensors. Based on covariance analysis, we demonstrate the observability of accelerometer biases in periodic curve trajectories. All the presented approaches have been implemented and tested on different models of agricultural machinery under real operating conditions.

The study was conducted with the support of Cognitive Pilot.

REFERENCES

1. **Golovan A.A., Nikitin I.V.** Combined use of strapdown inertial navigation systems and odometers from the standpoint of mechanics of inertial navigation systems. Part 1. Moscow University Mechanics Bulletin. Volume 70, pages 46–49. 2015
2. **Golovan A.A.** INS/Odometer Integration: Positional Approach. Gyroscopy and Navigation. v. 12. #2, 2021. DOI: 10.1134/S2075108721020048
3. **Polack, Philip & Althé, Florent & Novel, Brigitte & de La Fortelle, Arnaud.** The kinematic bicycle model: A consistent model for planning feasible trajectories for autonomous vehicles. 2017 IEEE Intelligent Vehicles Symposium (IV). PP. 812-818, 2017. doi:10.1109/IVS.2017.7995816.
4. **Min, Haigen & Wu, & Cheng, & Zhao.** Kinematic and Dynamic Vehicle Model-Assisted Global Positioning Method for Autonomous Vehicles with Low-Cost GPS/Camera/In-Vehicle Sensors. Sensors 19. 5430., 2019. DOI:10.3390/s19245430.
5. **Nayl T.** Modeling, Control and Path Planning for an Articulated Vehicle. Luleå tekniska universitet, Luleå, Sweden, 2013.
6. **Delrobaei M.** Design and Steering Control of a Center-Articulated Mobile Robot Module. Hindawi Publishing Corporation. Journal of Robotics. Volume 2011, Article ID 621879. DOI:10.1155/2011/621879
7. **Vavilova N.B., Golovan A.A., Parusnikov N.A.** Mathematical foundations of inertial navigation systems. Moscow University Publishing House. 2020